AN EXPERIMENTAL STUDY TO INVESTIGATE THE EFFECTS OF IN SITU STRESS STATE AND ROCK-FLUID INTERACTIONS ON PROPPED FRACTURE CONDUCTIVITY IN THE VACA MUERTA FORMATION

by

Dina A. Hegazy

A thesis submitted to the Faculty and the Board of Trustees of the Colorado School of Mines in partial fulfillment of the requirements for the degree of Master of Science (Petroleum Engineering).

Golden, Colorado

Date ___________________

Signed: ________________________

Dina A. Hegazy

Signed: ________________________

Dr. Azra N. Tutuncu
Thesis Advisor

Golden, Colorado

Date ___________________

Signed: ________________________

Dr. Erdal Ozkan
Professor and Department Head
Department of Petroleum Engineering

ABSTRACT

Much evidence has been presented in literature proving the importance of proppant testing for hydraulic fracture design. The majority of the research studies published for proppant conductivity present experimental results obtained under a laboratory uniaxial stress state. Under field in situ stress state, however, the fracture is subjected to triaxial stress. Propped fracture conductivity degradation resulting from various damage mechanisms and changes in mechanical properties depends on the stress state applied on the core samples tested and the sample sensitivity to the aqueous fluids.

In this research study, the main objective was to measure propped fracture conductivity and changes in ultrasonic wave velocity measurements performed under a triaxial stress state using 2% KCl brine saturated shale core samples from the Vaca Muerta formation in the Neuquén Basin, Argentina. The results of this study could aid in decision making regarding hydraulic fracture treatments and production optimization for operators in the Vaca Muerta shale. Another objective of the study was to quantify the relationship between fracture contact stiffness and shear wave velocity through uniaxial test measurements. This relationship could help estimate the stimulated reservoir volume (SRV) from microseismic data.

Fractures in core samples were induced parallel to the natural bedding planes, in the axial direction of core samples to obtain a natural rough fracture surface. Changes in the geomechanical properties due to interaction with KCl brine were measured before conductivity measurements were performed. Samples were saturated in 2% KCl brine for 30 days. Ultrasonic wave velocity measurements were conducted before and after saturation. A uniaxial test was performed utilizing a cubic sample to measure fracture displacement and P and S wave velocity as a function of stress. For conductivity measurements, samples were then placed in a triaxial sample cell where the cell pressure acts as the closure stress on the fracture. The confining stress was increased by stages and flow tests were performed to measure the permeability of the fractured sample at each stage. Acoustic data was also collected as the stress was increased for the calculation of acoustic wave velocities. Finally, after completion of the test, damage mechanisms were studied both through visual inspection and field-emission scanning electron microscopy (FSEM).

An insignificant decrease in core sample Young's moduli was measured with exposure to KCl brine. Fracture permeability was calculated from fracture aperture values obtained from derived relationships between fracture stiffness and shear wave velocity (V_s) obtained from the uniaxial test measurements.. The triaxial test results showed decrease in conductivity with increasing stress in the samples tested. Fracture permeability reduction was sensitive to stress at lower stresses up to 2000 psi while at higher stresses the rate of reduction decreased with increasing stress. Conductivity values at each point of measurement decreased and then stabilized at the second day of exposure to the respective stress condition. Damage mechanisms observed contributing to the conductivity degradation were spalling of the formation into the proppant pack, proppant embedment and fines migration. Compressional wave velocity increased slowly with increasing stress while shear wave velocity was more sensitive to stress increase.

TABLE OF CONTENTS

LIST OF FIGURES

LIST OF TABLES

ACKNOWLEDGMENTS

First and foremost, I would like to thank my advisor Dr. Azra N. Tutuncu. Dr Tutuncu shared her vast knowledge in geomechanics and wave velocity measurements with me to help me analyze the data. Her research ideas became a valuable part of my thesis. She was always open for any inquiries from me and provided me with beneficial articles to read for further enhancing my knowledge. Second, I would like to thank my committee members Dr. Erdal Ozkan and Dr. Steve Sonnenberg for their guidance and support through the time I spent pursuing my Master's degree. Dr. Ozkan's knowledge helped me a lot to understand flow through fractures, has been major part of my study. Dr. Ozkan is also a supportive department chair to all the petroleum engineering students. Dr. Sonneberg helped change my engineering thinking to be able to think in a geological point of view to analyze data correlating geology and data obtained from the laboratory. His discussions with students in the Vaca Muerta Consortium were enlightling to me and helped linking geology and engineering in this research study. I am especially grateful to him, because he was the reason I joined Mines in the first place,

I am indebted to Dr. Daisuke Katsuki. Without his guidance and mentoring, this study wouldn't have been possible. His creative ideas to make the triaxial assembly to be utilized for fractured samples with proppants are for me to complete my MS research in a timely manner. He was treating the research study as if it was his own.

I would like to thank Dr. Hossein Kazemi who helped me solve the issues I encountered in my calculations for fracture permeability. A few incidences occured where he stayed in his office later than he planned to explain some concepts to me that were essential for completing this thesis. I would to thank Dr. Jennifer Miskimins who never hesitated to answer my questions and help me out when I needed in research related topics. She would always reply to my emails right away, even when she was travelling. I would like to thank Dr. Katherina Pfaff for helping me get a kick start to obtain my FESEM images. Her guidance surely made the process of taking FESEM images more efficient.

I would like to thank Dr. Ali Mese for donating the triaxial cell to the UNGI consortium. The cell was an integral part of this research study.

I am surely grateful to have met people in the UNGI consortium. I would like to thank Jessica Iriarte, Bekdar Baizahov and Wale Adekunle for sharing with me our “late night” parties at the laboratory. Our common love for the “blues” and political discussions made time spent in the lab enjoyable. Jessica was my lab buddy during the past spring semester, when we were trying to calibrate the cell for fracture flow. She never hesitated to share with me her vast field knowledge in hydraulic fracturing which helped me grasp many concepts. Bekdar helped me a lot to understand the concepts of wave velocity propagation. Faisal Al Howaish, Rayan Alidi and Sebas Ramiro were always always providing me with support when I needed it.

I am really grateful to have Jamila Huseynova, Yijia Zhang, Ilkay Eker and Mesferah Al Qahtani as friends. They were constantly supporting throughout my tough times during the time of the research.

Last but not least, I would like to thank my family; my parents, my two sisters and brother for their love. They always provided me encouragement even at the toughest times. Without them, I would not be where I am today. My mom was actually the one who encouraged me to pursue my MS degree.

For my parents Salwa and Adham for their unconditional love.

CHAPTER 1

INTRODUCTION

The Vaca Muerta formation is considered the primary source rock for the Neuquén basin in Argentina. The formation is approximately 200-1700 feet and is known for its vertical and lateral heterogeneity, with varying lithological, petrophysical and geomechanical properties throughout the entire interval. Like most unconventional plays, wells drilled in the Vaca Muerta formation need to be hydraulically fractured to achieve economical levels of production. One of the main goals of hydraulic fracture design is preserving fracture conductivity within a proppant pack since it affects the capacity of the fracture to flow fluid. Evidence has shown that one of the main contributors to the steep production decline seen in shale plays, is declining fracture effectiveness due to conductivity decline (Vincent and Besler 2013). Damage mechanisms might occur during the hydraulic fracture operation, resulting in decreased fracture conductivity (Baree et al. 2003). Interactions with fracture fluids can also play a role in fracture conductivity degradation. The effect of rock fluid interactions and damage mechanisms and their effect on conductivity and mechanical properties of the formation could be investigated experimentally. Several published experimental studies have been performed on samples from US shale formations (Alramahi and Sundberg, 2012; Guzek 2014; Kamenov et al. 2013); however, very few are available for Vaca Muerta shale samples.

The ultimate goal of this study is to evaluate effects of rock fracture fluid interactions and high closure stress on propped fracture conductivity in Vaca Muerta shale samples. Damage mechanisms such as proppant embedment and fines migration that occurred throughout the experimental procedure are investigated. Results and observations are correlated with compressional and shear wave velocities recorded with increasing stress and rock properties determined through core analysis, such as formation mineralogy and Young's modulus. We use an apparatus for the experimental part of the research study that simulates more realistic pressure downhole conditions incorporating the hydraulic fracture operation. This is achieved by the introduction of triaxial testing into proppant conductivity testing.

The experimental results could serve as inputs to fracture simulators to simulate fracture and production performance in wells drilled in the Vaca Muerta formation. The proppant type and size used during the experiment is used in hydraulic fracture treatments in wells of the Vaca Muerta formation. Therefore, results should be relevant and applicable to field applications. The results could also be used to establish relationships between fracture stiffness and S-wave velocity through the fracture which could help in estimating hydraulic fracture width.

1.1 Objectives

The objectives of this research study were as follows:

- To quantify the effect of rock fluid interactions on change in geomechanical properties through measurements of Young's modulus and Poisson's ratio. During the experiments conducted, 2% KCl water was used and samples were saturated in that fluid for 30 days before the measurements were recorded.
- To find relationships between fracture stiffness and shear wave velocity from uniaxial test data for fracture width estimation.
- To design a system using the triaxial cell in the UNGI lab, that could be used to measure proppant embedment and conductivity in fractured core samples.
- To quantify the reduction in propped fracture conductivity due to the occurrence of damage mechanisms as a function of stress, utilizing triaxial measurements.
- To investigate the relationship between compressional and shear wave velocities and fracture conductivity loss.
- To characterize the damage mechanisms that were induced as a result of the testing conditions.

1.2 Research Motivation

The knowledge of how mechanical properties can affect hydraulic fracture performance is important for hydraulic fracture treatment design. Fracture conductivity is dependent on the mechanical properties and mineralogy of the formation. Maintaining fracture conductivity is vital for the success of hydraulic fracture operations. Therefore, experiments need to be performed to test the fracture conductivity under field in situ stress conditions to better select the operational parameters for the fracture job such as the types of proppants and fracturing fluids. Most published experimental results have been from experiments performed under uniaxial stress conditions. In this research study, proppant conductivity experiments have been conducted under a triaxial stress state to better simulate downhole pressure conditions and obtain more reliable results. Since there are very few experimental results published for the Vaca Muerta formation, experiments performed in this research can serve as reference for selecting proppant types in future hydraulic fracture treatments performed in the Vaca Muerta formation and other shale formations with similar characteristics.

Argentina's world class shale oil and gas resources, including the Vaca Muerta, can potentially make the country energy independent. According to a report by the Energy Information Administration (EIA) (2013), the Neuquén Basin, where the Vaca Muerta play is located, is the leading producer of hydrocarbons in Argentina. Therefore, optimization studies, like the one described in this research study, can help to properly utilize these resources. Moreover, more accurate input of hydraulic fracture permeability could help obtain better estimation of expected production and more accurate economical evaluation, which in turn leads to improved decision making for operators in the Vaca Muerta formation.

1.3 Vaca Muerta Overview

The Vaca Muerta formation is considered one of the key source rocks for oil and gas fields in the Neuquén basin. Risked technically recoverable reserves shale gas and oil are estimated to be 308 Tcf and 16 billion barrels, respectively (EIA 2013). At present, more than 400 wells are on production from the Vaca Muerta shale (Licitra et al. 2015).

1.3.1 The Neuquén Basin

The Vaca Muerta formation is located in the Neuquén Basin of Argentina. The basin occupies an area of around 137,000 km^2 and is located in central-western Argentina (EIA 2013). It is bordered by the Andes in the west, the Colorado Basin and the North Patagonian Massif in the east as illustrated in Figure 1.1 (Sagasti et al. 2014).

The basin contains strata of Late Triassic to Early Cenozoic age that were deposited in a back arc tectonic setting. Its seven km thick stratigraphic column consists of carbonates, evaporites and marine siliciclastic rocks (Manceda and Figueroa 1995). The organic rich Vaca Muerta and Los

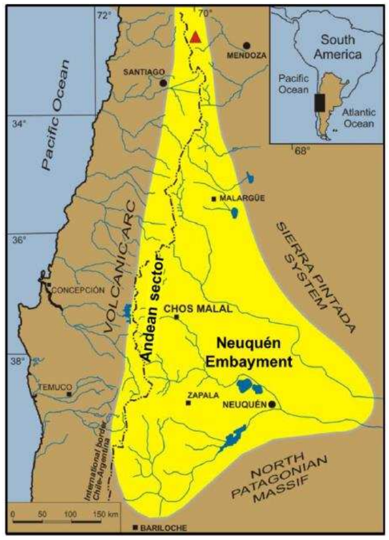

Figure 1.1: Structural domain and boundaries of the Neuquén Basin with its geographical location on the upper right corner (Sagasti et al. 2014).

Molles formations are considered the primary source rocks for the fields in the Neuquén Basin (Howell et al., 2005). The relative thickness of the two formations with respect to the overlying and underlying formations can be seen in Neuquén Basin's stratigraphic column in Figure 1.2.

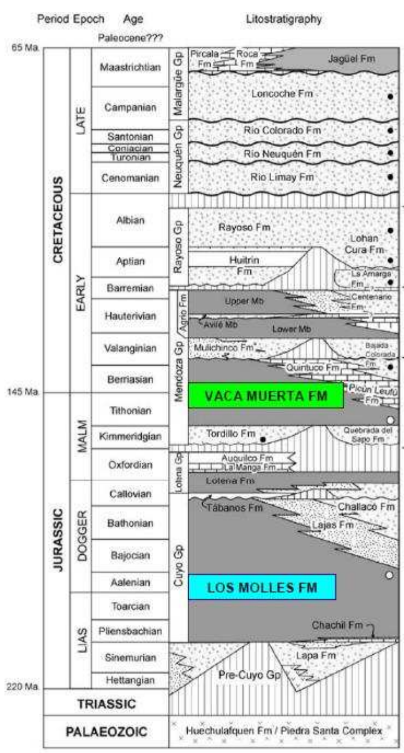

Figure 1.2: Stratigraphic column of the Neuquén Basin, showing relative thickness of the Vaca Muerta and Los Molles formations (Howell et al. 2005).

1.3.2 The Vaca Muerta Shale Play

The Vaca Muerta formation is considered the largest source rock in the Neuquén basin, with a thickness ranging from 25-450 meters, covering an area of around 25,000 km^2. It has the largest estimated reserves and largest number of field development projects among all the formations present in the Neuquén Basin. The formation has been explored for unconventional shale oil and gas since 2010 and most of the exploration wells indicated presence of oil and gas. The Vaca Muerta's favorable source rock characteristics have attracted many operators to drill in the area. Initial production from vertical wells drilled is around 42 bbls/day and around 95 bbls/day for the horizontal wells. Although there is limited production history, estimated ultimate recovery (EUR) at 25 years is 176,000 bbl for vertical wells and 300,000 bbl for horizontal wells in the Vaca Muerta formation (Stinco and Barredo 2014). The Eagle Ford shale in South Texas is considered the analog for the Vaca Muerta shale (Tepper et al. 2013). The Vaca Muerta shale has the same maturity variation as the Eagle Ford with the maturity progressing from oil to condensate to gas window from the west to the east as seen in Figure 1.3. The area studied in this research is focused mainly on the oil window.

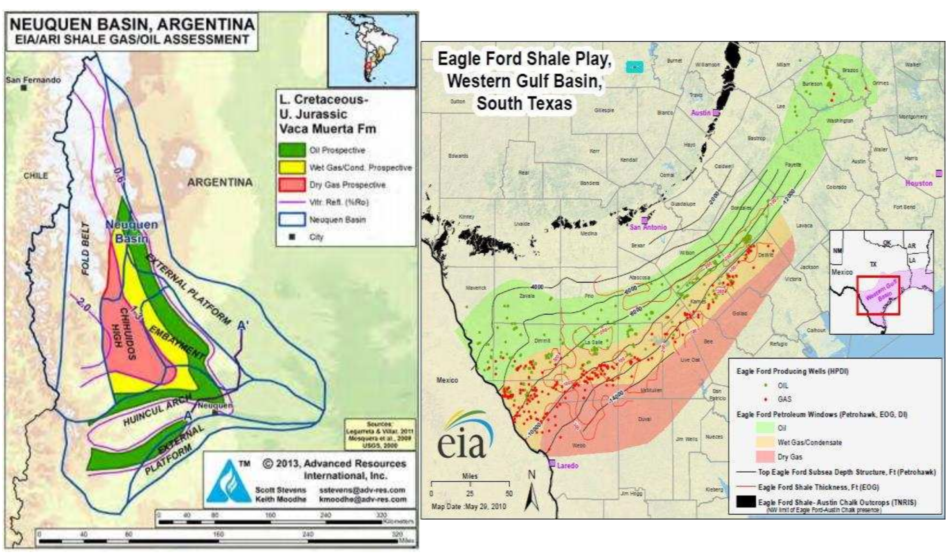

Figure 1.3: Maturity maps of the Vaca Muerta (Kuuskraa et al. 2013) and Eagle Ford (EIA 2014) shales on the left and right hand side respectively.

The Vaca Muerta formation can be divided into three sections. The lower Vaca Muerta is the highest in Total Organic Carbon content (TOC) and is considered the organic rich kitchen for the formation. The upper Vaca Muerta is also organic rich and laminated like the lower section. The middle Vaca Muerta, however, is less laminated and lower in organic content than the other two sections.

The Vaca Muerta shale is of Late Jurassic to Early Cretateous age. The formation can be considered calcareous shale/marl with illite type clay and a transition to smectite-illite as we go deeper in the basin (Kugler 1985; Wren 2011). The formation was deposited as a propagating wedge, increasing in thickness from the south to the east towards the north and west. The marine shale was deposited in an anoxic environment and contains Type II kerogen. The shale is finely stratified, black and dark gray and contains limestone lenses (Aguirre-Uretta et al. 2008).

1.3.3 Formation Properties

Although thinner than the Los Molles formation as shown in Figure 1.2, the Vaca Muerta shale is more organic rich and occupies more area across the Neuquén basin. Due to its organic richness, the oil prone Vaca Muerta has sourced an estimate of 50% of all the formations in Argentina (Kietzmann et al. 2011). Oil production from Vaca Muerta sourced rocks is generally high quality with light oil (31-58° API) (Urien and Zambrado 1994).

Many studies have been performed to evaluate the total organic content (TOC) of the formation. Parnell and Carey (1995) collected samples from wells and bitumen veins from mines in the north that were organically rich up to 14.2 weight% TOC. TOC ranged between 2.9-4% in samples taken from the south and up to 6.5% in lower bituminous shales of the Vaca Muerta. In a presentation by Wren (2011), the Vaca Muerta reservoir characteristics were found to be comparable or even more favorable to US shales as shown in Table 1.1.

Table 1.1: Comparison of the Vaca Muerta Shale and Major Shale plays in the United States (Wren 2011).

	Haynesville	Barnett	Marcellus	Woodford	Vaca Muerta	Horn River	Eagle Ford
Lithology	Siliceous Marl	Siliceous Shale	Siliceous Shale	Chert	Siliceous Marl	Chert	Calcareous Shale
Average Mature TOC(%)	3 to 4%	4 to 5%	4 to 7%	4 to 8%	3 to 5%	3 to 6%	4 to 8%
Net Thickness (Ft)	225 to 300	150 to 250	75 to 150	75 to 150	300 to 1300	125 to 450	120 to 280
Maturity (Ro)	1.7 to 2.8	1.3 to 2.1	1.3 to 2.4	1.2 to 2.8	1.4 to 1.8	1.6 to 2.7	0.7 to 1.8
Pressure Gradient (ppg)	13.5 to 17.3	9.6 to 10.6	11.6 to 13.5	9.6 to 10.6	9.4 to 17.3	10.6 to 13.5	9.6 to 14.5
Porosity (%)	7 to 9%	4 to 8%	7 to 9%	5 to 6%	7 to 12%	4 to 10%	4 to 10%
Permeability (nD)	100 to 500	50 to 200	100 to 200	40 to 70	50 to 200	100 to 1000	100 to 1500
Well IP (mcfd peak month)	8 to 25	3 to 7	4 to 10	2 to 6	2 to 12	5 to 8	2 to 17
GIP*/Sq Mi (bcf)	150 to 250	100 to 150	75 to 125	75 to 150	300 to 800 (bcf)	175 to 250	80 to 250
EUR**/Well (bcf)	8 to 12	3 to 4.5	3 to 6	2.5 to 5	8 to 20	4 to 10	2 to 6

The mineralogy of the Vaca Muerta formation is analogous to that of the Eagle Ford. X-ray diffraction (XRD) data collected from several US shale plays and the Vaca Muerta is shown in Figure 1.4. From the data collected, it is evident that both the Eagle Ford and the Vaca Muerta formations have more carbonate than quartz, yet the Eagle Ford contains higher clay content (Tepper et al. 2013).

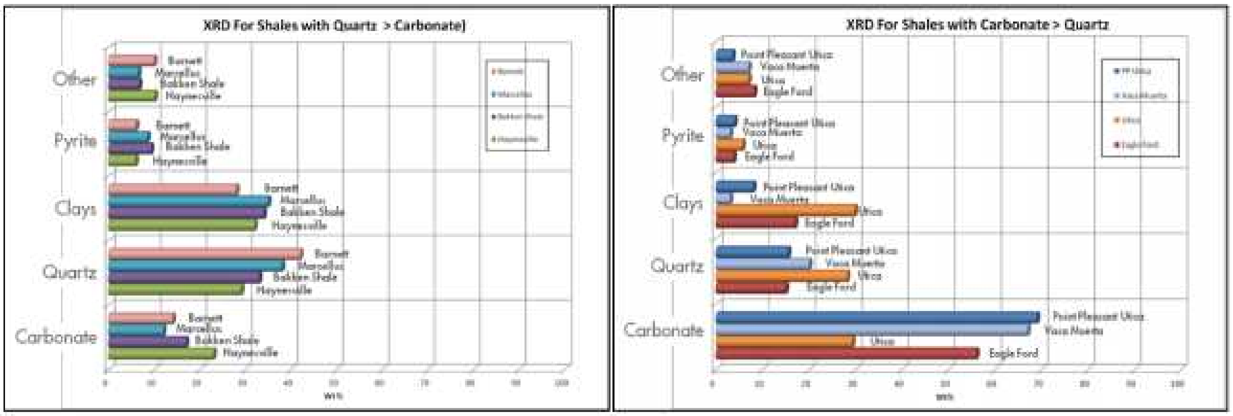

Figure 1.4: XRD data comparison between different US shale gas and oil plays and the Vaca Muerta shale (Tepper et al. 2013).

1.4 Location of Study

In this research study, Loma Jarillosa Este (LJE) block data was used (shown in the following map in Figure 1.5), since most of the field data and cores used are provided by the sponsors from the wells in the LJE area.

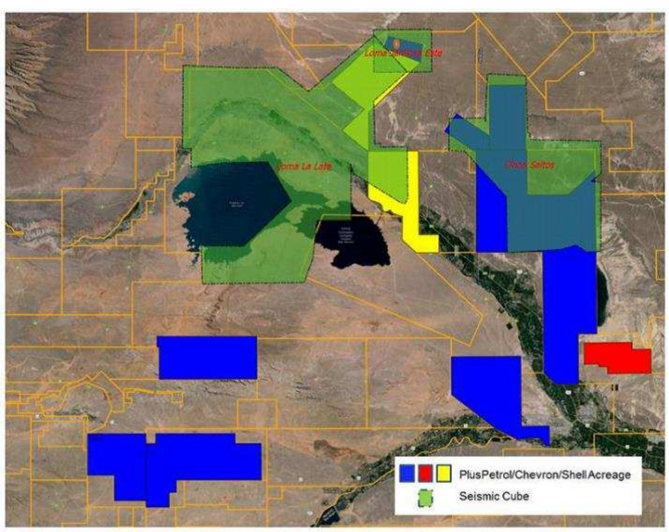

Figure 1.5: Maps of blocks covered by different operators displayed by color (Kernan 2014).

1.5 Available Data

A wide variety of well log and core data relevant to this research study, that aided in the analysis of the current experimental results, was supplied by sponsors and earlier research results from students in the Vaca Muerta consortium. This data includes core analysis results, log data from various wells, pump schedules, formation mechanical data and fracture description.

Data provided by sponsors includes a wide variety of logs and core petrophysical properties and mechanical properties, along with a few embedment test results. Additionally, pump data was provided for 2 wells drilled in the LJE block as well as microseismic data and formation images (FMI). Correlations between dynamic and static rock mechanical properties have been derived by Willis (2013) and microfracture characterization has been performed by Hernández Bilbao (2016) as part of the earlier research studies in the Vaca Muerta consortium at Colorado School of Mines.

1.5.1 Core Petrophysics and Mineralogy

An 18 m core from the LJE.x-1010 well was donated to the research consortium by Plus Petrol. The core was taken from the lower most section of the organic rich lower Vaca Muerta. Full core analysis has been performed at TerraTek laboratory including geomechanical measurements, porosity, permeability, saturation, mineralogical composition and source rock analysis.

Petrophysical analysis was performed on various depths along the length of the core. The effective porosity average is around 3% and permeability is in micro-Darcy range. Oil saturation decreases as the depth increases in the core.

Mineralogical composition of the samples was obtained from X-ray Diffraction (XRD) analysis (Figure 1.6) and Quantitative Scanning Electron Microscope (QEMSCAN) analysis (Figure 1.7). The mineralogy along the length of the core is highly variable. The formation mainly consists of quartz, calcite, feldspar and varying clay minerals. Clay weight% in several samples was low (<10%) and high in other samples (>30%), with an average of around 25 wt%. Clays are mostly illite/mica or in the mixed layer illite/smectite phase. The carbonate content in the measured core is not necessarily more than the quartz content, unlike the results presented by Tepper et al. (2013). Carbonate and quartz content vary throughout the length of the core, with most of the samples being quartz rich as shown in Figure 1.6.

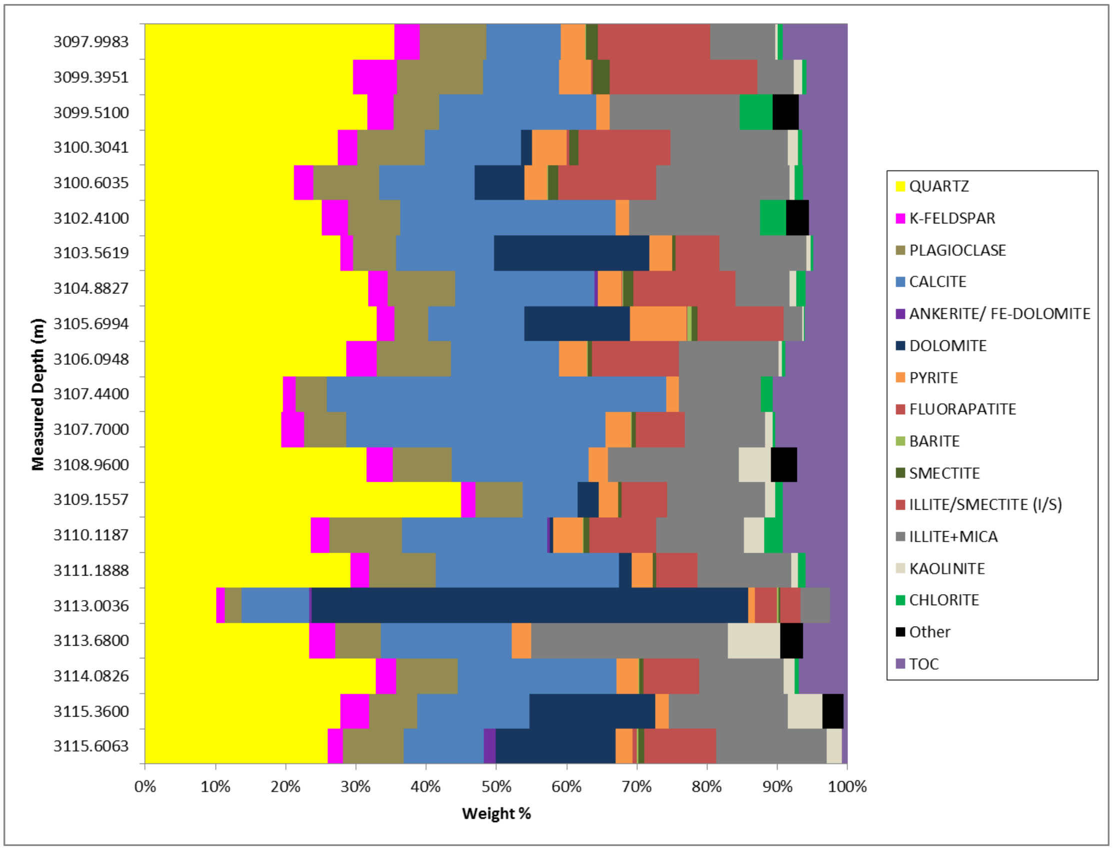

Figure 1.6: Mineralogical composition of LJE.x-1010 core from XRD analysis and total organic content (TOC) from SRA analysis.

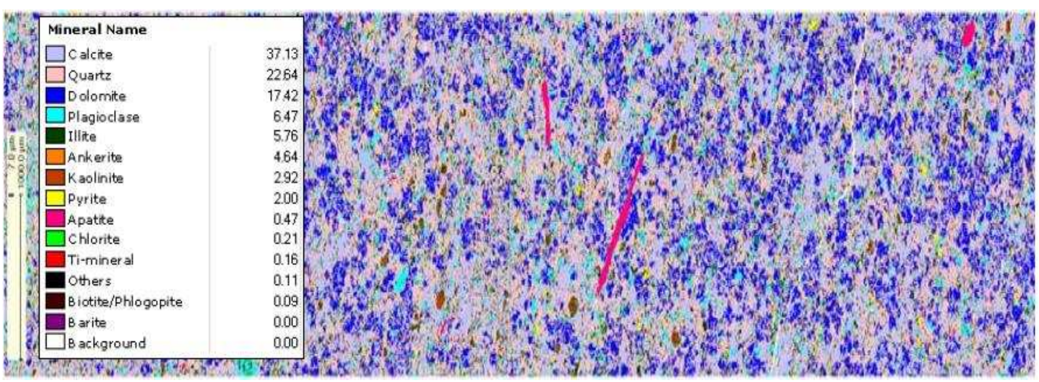

Figure 1.7: Example of a QEMSCAN image of a sample from the LJE.x-1010.

From the petrographic images analyzed by Hernández Bilbao (2016) (Figure 1.9) combined with XRD results, it could be concluded that the lower most part of the Vaca Muerta formation depending on the carbonate content, could be either identified as a siliceous mudstone or marlstone as shown in Figure 1.8.

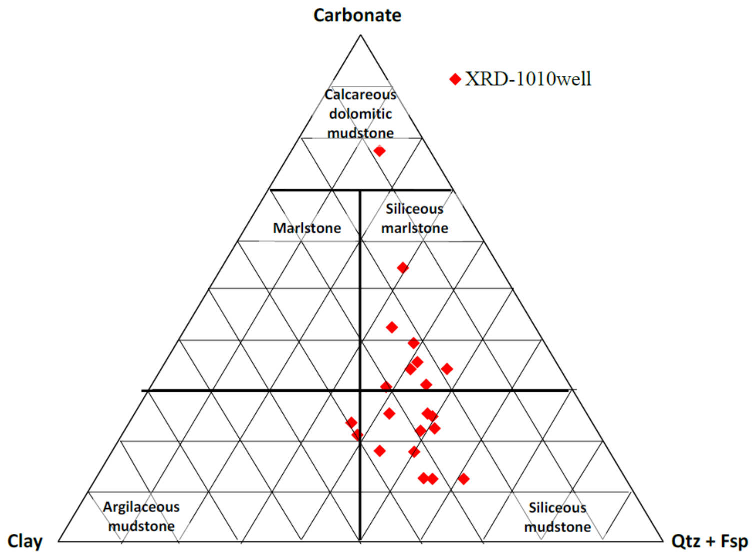

Figure 1.8: Ternary Diagram of the XRD mineralogy of the 21 samples from the LJE.x-1010 core. Samples containing <30 wt% carbonate are classified as mudstones, while samples with 30-70 wt% carbonate are classified as marlstones (Hernández Bilbao 2016).

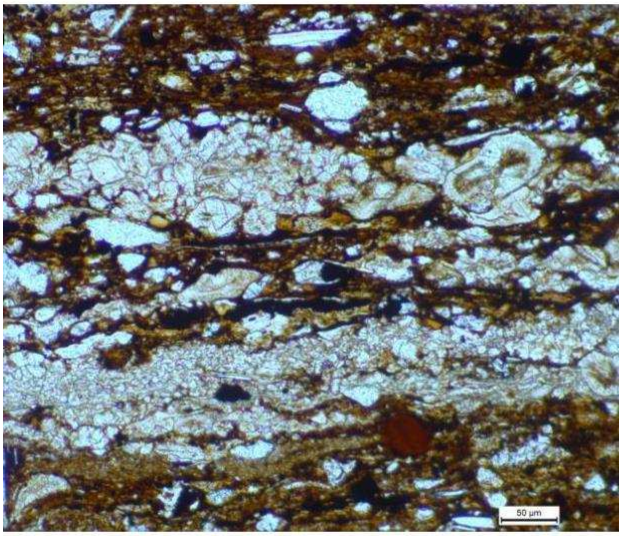

Figure 1.9: Photomicrographs of the lower Vaca Muerta Formation. Sample shows a quartz-rich layer in a clay and organic-rich matrix (plane polarized light, scale 50 μm) (Hernández Bilbao 2016).

The total organic carbon content (TOC) based on the source rock analysis (SRA) ranges between (0-12 wt%) (Figure 1.10). Furthermore, the analysis on core and outcrop samples confirms that the Vaca Muerta formation is within the oil window as it is mainly Type I-II kerogen (Figure 1.11).

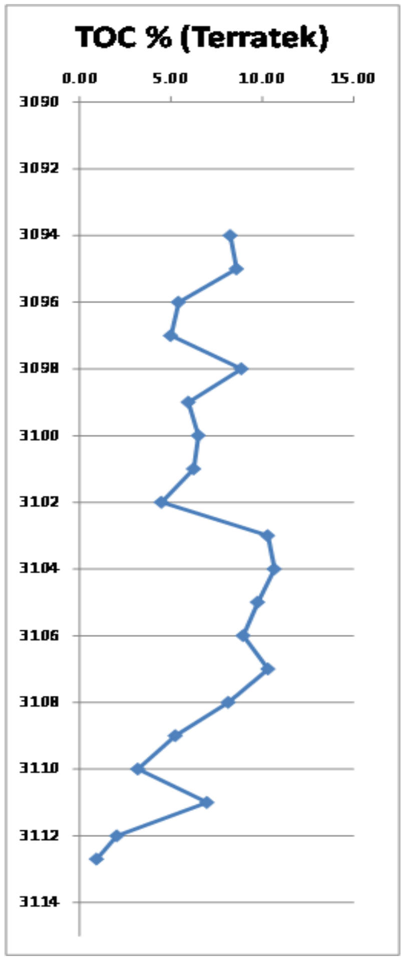

Figure 1.10: TOC wt% values throughout the length of the LJE.x-1010 core.

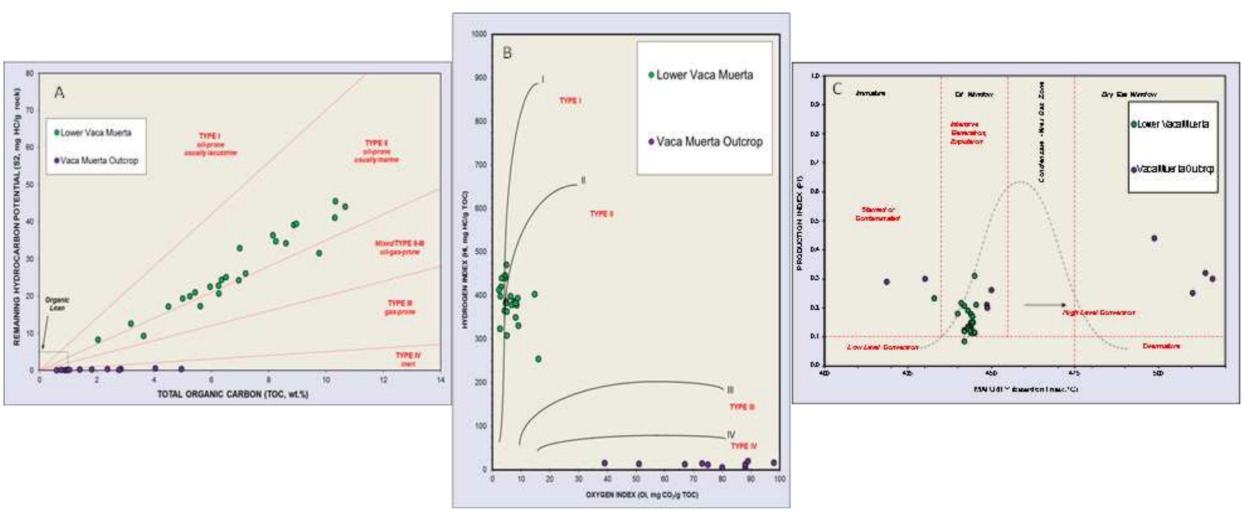

Figure 1.11: SRA analysis performed on lower Vaca Muerta core and Vaca Muerta outcrop samples (A) S2 vs. TOC plot; (B) Hydrogen index vs. oxygen index plot; (C) Production index vs. thermal maturity plot.

1.5.2 Fracture Characterization

There is a lot uncertainty when characterizing fractures in unconventional reservoirs due to their anisotropic nature. Determining the fracture orientation from core and logs could possibly reduce the uncertainty. Formation Micro Imager (FMI) logs were acquired on the LJE.x-1010 and LJE.x-1011 wells. The direction of the fractures, which is usually in the direction of the maximum horizontal stress, could be determined from these FMI logs. For example, in the LJE.x-1010, the breakouts observed in the Vaca Muerta section are 150° north east.

The direction of the maximum horizontal stress is normally perpendicular to the observed breakouts. Thus, the maximum horizontal stress and the natural fractures are in the N60°E direction (Figure 1.12).

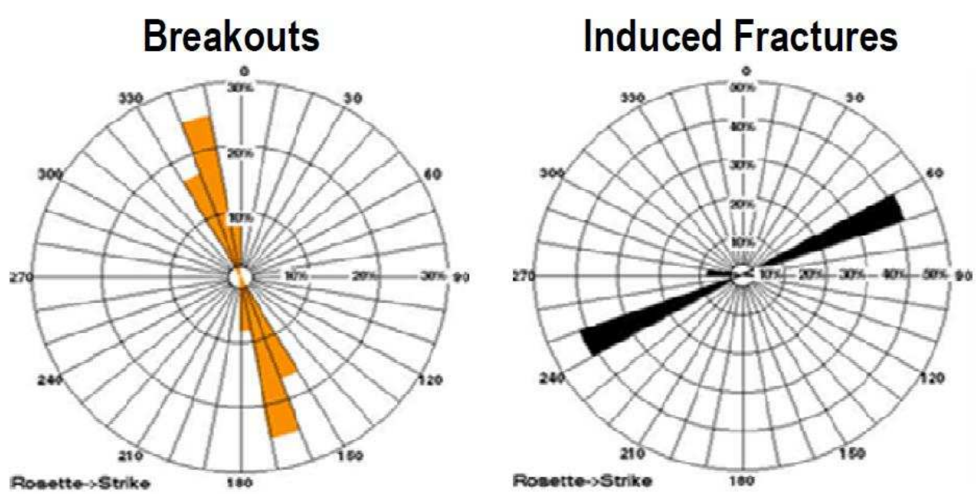

Figure 1.12: Micro Imager (FMI*) log interpretation of the LJE.x-1010.

Microfractures are too small to be captured by logs. They should be described through core description and microscopy. Microfractures throughout the depth of the whole LJE.x-1010 core were described by Hernández Bilbao (2016). The orientations of the microfractures, which are calcite filled, were found to be either bedding parallel or subvertical as shown in (Figure 1.13).

1.5.3 Mechanical Properties

Formation mechanical properties were available on a core and log scale in this study. Mechanical tests were performed on samples from the available core from the LJE-1010 well. Six depth points from the core were chosen for the analysis and for each depth point three core plugs

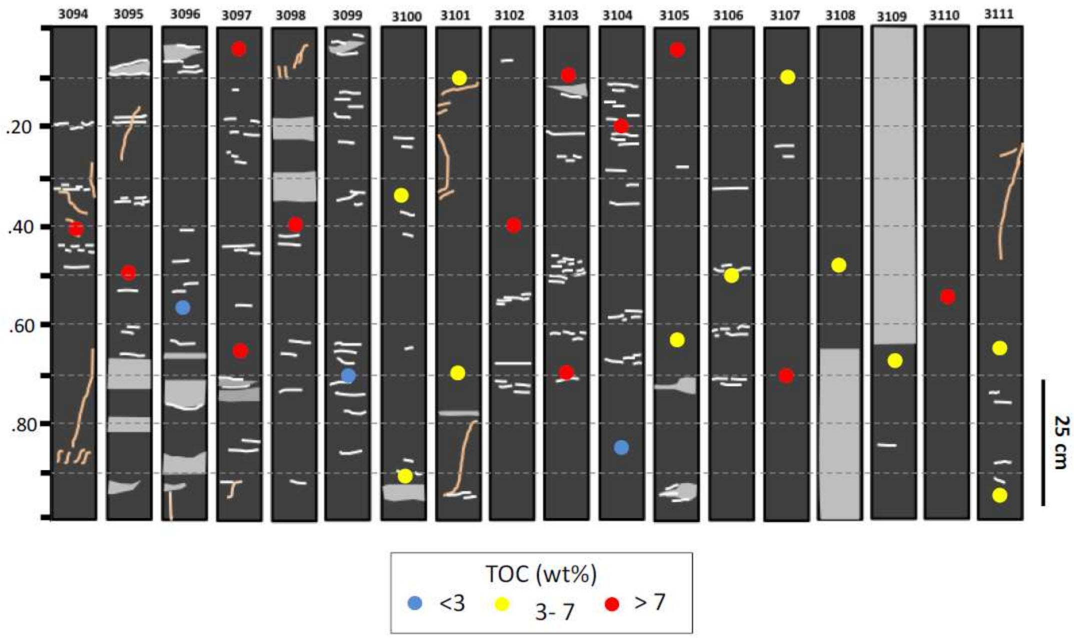

Figure 1.13: Illustration of calcite-filled horizontal fractures (white) and sub-vertical fractures (orange) in the LJE.x-1010 core. TOC wt% is color coded according to value. Concretions and/or carbonate-rich facies are in light gray (Hernández Bilbao 2016).

were taken parallel to bedding, perpendicular to bedding and 45° to bedding. From these tests, static mechanical properties were obtained.

Willis and Tutuncu (2014) developed a correlation between static and dynamic moduli customized for the Vaca Muerta formation using the results from tests performed on these core samples. The log derived dynamic elastic moduli were converted to static moduli that were used in the study as they are more representative of the formation properties relevant to the hydraulic fracturing. Willis (2013) established a 3D Mechanical Earth Model (MEM) by defining geomechanical clusters and upscaling the clusters based on the geomechanical properties.

1.5.4 Hydraulic Fracturing Data

Pump schedule and completion data were provided by Plus Petrol for two wells in the LJE block: LJE.x-1010 and LJE.x-1011 wells. Two stages were pumped in each well. The schedule data included timing, pump rates, volumes, proppant concentration and weight of the proppant pumped. Fluid and proppant types and the amounts pumped for each type were provided in the operation reports. A hybrid fluid system was used in the hydraulic fracture treatment for the two wells starting with slick water, then pumping higher viscosity fluids (linear gel) followed by the cross-linked fluid. Ceramic proppants were used due to the high closure pressures in the Vaca Muerta formation. Moreover, hydraulic fracture pretest diagnostic data was included.

CHAPTER 2

LITERATURE REVIEW

In order to be able to design a reliable experiment that is applicable to realistic fracture treatments, one must: 1) understand the basics of hydraulic fracturing and geomechanics; 2) review relevant experiments in the area of interest that might provide a guideline for the intended experimental objective.

2.1 Hydraulic Fracturing Technology

To accommodate rising energy demand, shale plays have been developed for production. These reservoirs have nanodarcy scale permeability, low porosity and complex geological and mechanical properties making completion design complex and producing an economic challenge. Production from shale oil and gas wells has been made economically feasible by introducing multistage hydraulic fracturing in horizontal wells. Holditch et al. (2007) defined unconventional gas reservoirs as "natural gas that cannot be produced at economic flow rates nor in economic volumes of natural gas unless the well is stimulated by a large hydraulic fracture treatment, a horizontal wellbore, or by using multilateral wellbores or some other technique to expose more of the reservoir to the wellbore". The same definition can be applied to unconventional oil reservoirs. The multiple hydraulic fractures in horizontal wells are usually propped (Saldungaray et al. 2013). The hydraulic fractures increase the contact area of the well into the formation in order to achieve the economic rates desired.

2.1.1 The Hydraulic Fracture Treatment Process

The hydraulic fracture operation consists of several steps. The hydraulic fracture treatment is performed by first injecting at high rate and pressure the "pad" to breakdown the formation. Following the pad, the slurry containing the proppant is injected. As the proppant follows the pad, fluid leaks off and it becomes more of a solid form. The proppant is designed to keep the hydraulic fracture open to maintain conductivity. A flush volume is then injected to displace the slurry to the top of the perforations. The injection process is then shutdown to allow for the fracture to close on the proppant and leak off into the formation. Finally, the remaining fracturing fluid is allowed to flow back from the fracture, with as much gel residue as possible (Miskimins 2015).

2.2 Hydraulic Fracturing Geomechanics

Basic geomechanics principles must be known to be able to understand the mechanisms of hydraulic fracture initiation and propagation. The concept of stress is the root to grasp the geomechanical concepts involved in hydraulic fracture behavior.

2.2.1 Principle stress

Absolute stress, created by an external load is the total stress applied on the rock grain and pore fluid in the pore space. The stress acting on the rock grains is referred to as the effective stress expressed in Equation 2.1, where $\sigma_{v,eff}$ is the effective stress and σ_v is the stress in the vertical direction or the overburden stress (Terzaghi 1943). An increase in pore pressure (p_p) results in the dilation of the rock, while a decrease in pore pressure is caused by compression in the rock. Biot's coefficient (α) can be defined as the percentage of the pore pressure bearing the stress.

$$\sigma_{v,eff} = \sigma_v - \alpha p_p \tag{2.1}$$

The absolute vertical stress at each depth is referred to as the absolute overburden stress. In the case of isotropic stress state conditions, the relationship between the minimum horizontal stress $\sigma_{h,eff}$ and effective overburden stress presented in Equation 2.2 is applicable. The maximum horizontal $\sigma_{H,max}$ stress is the sum of the minimum horizontal stress and the tectonic stress σ_{tech} (Equation 2.3).

$$\sigma_{h,eff} = \frac{v}{1-v}\ \sigma_{v,eff} \tag{2.2}$$

$$\sigma_{H,max} = \sigma_{h,min} + \sigma_{tech} \tag{2.3}$$

2.2.2 Rock failure

Several failure criteria have been developed to describe rock deformation. The most well known of the failure concepts is Mohr's circle and failure envelope. The graphical representation of Mohr's circle was described by Meissner (1984). Stress conditions in a rock are represented by the Mohr's circle, where the maximum and minimum stresses (S1 and S3 respectively) intersect the x-axis as shown in Figure 2.1. As the circle "touches" the failure envelope, the rock is expected to fail. Mohr Coulomb failure criteria (Jaeger and Cook 1979) could be used in describing the subsurface conditions such as increase in pore pressure and decrease in reservoir temperature due to waterflood operations.

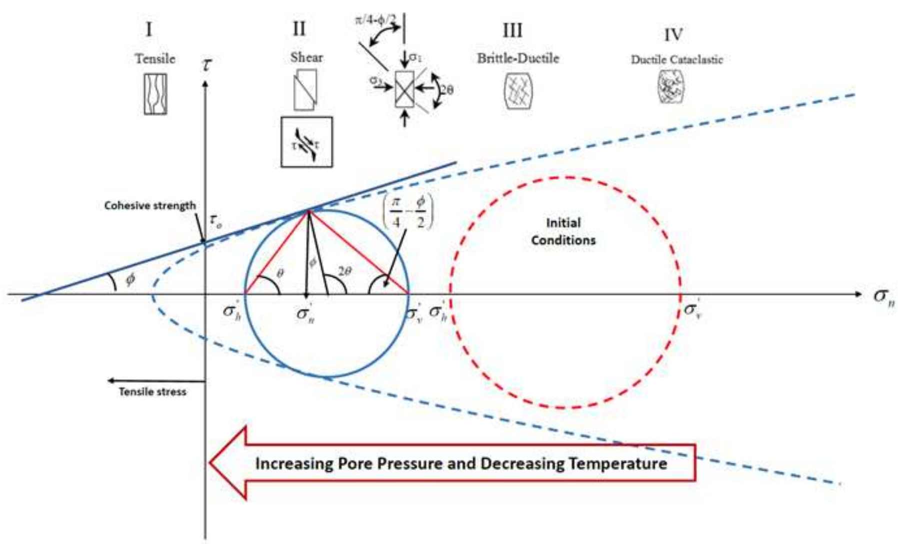

Figure 2.1: Graphical representation of Mohr’s circle with the illustration of rock failure due to increasing pore pressure (Kazemi 2015).

Other rock failure criteria exist and could be used to develop the failure envelop. These failure criteria include Drucker-Prager (Drucker and Prager 1952), Inscribed Drucker-Prager (Veeken et al. 1989), Tresca (Drucker and Prager 1952), Hoek-Brown (Hoek and Brown 1980), Modified Wiebols-Cook (Zhou 1994), Lade (Lade 1977), and Modified Lade (Ewy 1999). According to Colmenares and Zoback (2001), the selection of which criteria to apply is based on the several aspects such as the materials, types of loads, and treatment of intermediate principal stress.

2.2.3 Modes of Crack Deformation

The three modes of crack deformation are described by Liebowitz (1968) in Linear Elastic Fracture Mechanics (LEFM). The modes are illustrated in Figure 2.2. They include Mode-I (opening mode), Mode-II (sliding or in-plane shear mode), and Mode-III (tearing or out-of-plane shear mode). Mode-I crack is caused by normal tensile stress that exerts on the plane of the crack.

Fracture propagation in Mode-I is typically in the direction that is perpendicular to in-situ minimum stress and Mode-II and Mode-III are a result of shear stress applied to the plane of crack; crack tip displacement is parallel to the plane. In Mode-II and III, the direction of applied shear stress is perpendicular to the leading edge and parallel to the crack front, respectively.

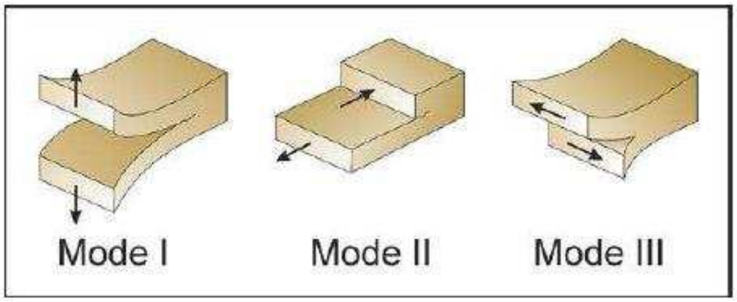

Figure 2.2: The three modes of crack deformation (Hudson and Harrison 1997).

2.2.4 Fracture Initiation and Extension

The geometry and direction of propagation of hydraulic fractures is determined by the in situ stress field within a formation. The orientation of the fracture is determined by its angle to the minimum and maximum horizontal stresses. The possible different scenarios of fracture orientation are shown in Figure 2.3. Transverse fractures, which are the most common scenario, are obtained when the lateral is drilled in the direction of the minimum horizontal stress or at an angle to the maximum horizontal stress (Tutuncu 2016).

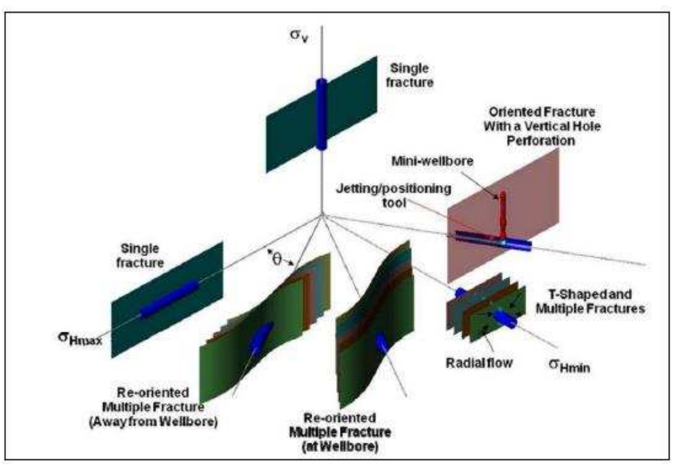

Figure 2.3: Fracture geometries expected with different well orientation. Notice that in most cases transverse fractures are expected (Tutuncu 2016).

A hydraulic fracture will initiate provided that the pressure required to breakdown the formation exceeds the stress concentration around the wellbore and the tensile strength of the formation, T_0. The stress concentration around the wellbore is composed of the stresses induced due to the drilling operation of the well. The calculations of tangential stresses σ_θ around the wellbore in case the well is drilled parallel and perpendicular to the minimum horizontal stress are shown in Equation 2.4 and Equation 2.5, respectively.

$$(\sigma_\theta)_{\theta=0} = 3\sigma_x - \sigma_y = 3\sigma_{h,\,min} - \sigma_{H,\,max} \tag{2.4}$$

$$(\sigma_\theta)_{\theta=\pi/2} = 3\sigma_y - \sigma_x = 3\sigma_{H,\,max} - \sigma_{h,\,min} \tag{2.5}$$

If the effective stress is considered, from Equations 2.4 and 2.5, the fracture breakdown pressure pbd could be expressed in Equation 2.6.

$$p_{bd} = 3\sigma_{h,\,min,\,eff} - \sigma_{H,\,max,\,eff} + p_p + T_0 \tag{2.6}$$

The fracture opens provided that the fluid pressure (p_{fl}) inside the fracture is not less than the closure pressure (p_c), given in Equation 2.7. The difference between p_{fl} and p_c is referred to as net pressure Δp_{net}. The effect of tectonics on closure pressure is accounted for with the inclusion of regional tectonic strain (E_ε) and regional tectonic stress σ_t.

$$p_c = \frac{v}{1-v}\,(p_{ob} - \alpha_v\, p_p) + \alpha_h p_p + E\varepsilon + \sigma_t \tag{2.7}$$

2.2.5 The Effect of Fracturing Fluids on Geomechanical Properties of Shale

The Young's Modulus and the Poisson's ratio are two important mechanical parameters to look at when trying to identify the potential for a shale prospect. The Young's modulus describes the stiffness of the material and it is the ratio of stress to strain. The Poisson ratio is the transverse strain divided by the axial strain. Kundert and Mullen (2009) recommended selecting intervals that are organic rich with high TOC content as well as the "brittle" intervals that have natural fractures present that could be detected by imaging log or core analysis. The definition of the term brittleness varies in literature. Stiffer zones are easier to fracture and interactions with with fracture fluids could reduce a shale's Young's modulus making them less stiff (Akrad et al. 2011; Corapcioglu 2014; Padin 2015).

2.3 Fracture Conductivity

Fracture conductivity is defined as the volumetric capacity of the hydraulic fracture to transmit fluids. It is the product of the fracture width *w* and fracture permeability k_f. It is an important parameter that should be considered by a completion engineer when designing a hydraulic fracture job to ensure a successful fracture treatment. Fracture conductivity is also a function of fracture width squared according to the parallel plate model as explained in Equations 2.8 and 2.9. The pressure change with respect to length is *dp/dx* and μ is the viscosity.

$$q = \frac{-w_f^3\, dp}{12\mu\, dx} \tag{2.8}$$

Substituting with Darcy's equation $(k=q\mu l/A\Delta p)$ in Equation 2.4:

$$k_f = \frac{w_f^2}{12} \tag{2.9}$$

The parallel plate model cannot fully model permeability through fractures as it assumed that the two fracture faces are smooth, neglecting the true fracture roughness. The asperities in the fracture in case of propped conductivity experiments deform/compact as applied stress is increased. This results in the increase in the distance of the fluid path and the decrease in fracture closure rate, which are not considered in the parallel plate model (Kranz et al. 1979).

The dimensionless fracture conductivity is defined in Equation 2.10. The parameter is both dependent on the fracture's ability to deliver fluid to the wellbore ($k_f\, w_f$) and the formation's capacity to flow fluids to the fracture which is calculated by multiplying the formation permeability k by the fracture half length (x_f). Therefore, it can be used as a measure to understand the fracture's performance in a reservoir.

$$F_{ed} = \frac{k_f w_f}{k x_f} \tag{2.10}$$

Numerous sources in literature demonstrated that fracture conductivity has a great impact on expected production. Vincent (2002) summarized the result of 80 field cases where conductivity enhancement resulted in increased well conductivity. He included a wide diversity in his study where he looked at results of production improvements in wells drilled in high permeability, low permeability and gas storage fields. He concluded that not only the improved conductivity can enhance well production, but it can also help reduce the effects of multiphase flow and mitigate issues such as sand production, paraffin build-up and asphaltene deposition. Coker and Mack (2013) presented studies where conductivity was enhanced due to better proppant selection. They concluded that increased fracture conductivity can lead to a significant increase in production. Results of simulation studies performed by Mayerhofer et al. (2006) show that by increasing the fracture conductivity from 0.5 md-ft to 5 md-ft, production over 5 years increases by 4 times.

Having noted the impact that fracture conductivity imposes on production, hydraulic fracture treatments need to be designed, taking into account that fracture conductivity is maintained downhole, especially in low permeability shale systems like the one studied in this research. Fracture conductivity decline is a strong contributor to the steep production decline curves that are seen in shale. Several evidences have been presented by Vincent and Besler (2013) to support this claim. For example, it was found in various shale plays such as the Eagle Ford and the Bakken that well productivity is highly dependent on depth. In addition, in cases where fractures were connecting two wellbores, diagnostics tests indicated that those fractures are no longer continuous.

Proper proppant and fluid selection can reduce the occurrence of damage mechanisms contributing to fracture conductivity loss. Fluids selected must be compatible with the formation to reduce the effect of chemical and mechanical damage and proppants must be the right type, size and concentration to ensure optimum fracture conductivity. The selection of these two components dictates the quality and success of the hydraulic fracturing treatment.

A description of how proppant and fracturing fluids selection can affect fracture conductivity is presented in the following sections. Damage mechanisms and other factors that contribute to conductivity loss in fractures are also explained.

2.3.1 Fluid Selection

Fracturing fluid selection is one of the primary steps of hydraulic fracture treatment design. The fluid selected for the fracture treatment must be compatible with the formation, selected proppants and wellbore design. Several requirements must be met by the fracturing fluid to prevent risks that they might pose on the production process. Anderson et al. (1982) listed some of the fluid characteristics that the completion engineer should be aware of when designing the fracture treatment and they are follows:

- Width-Generating Ability: The capability of the fluid to generate fracture width increases with fluid viscosity.

- Metal Corrosion: Reactions between fracture fluids and metals in wellbore components can yield large volumes of gelatinous iron oxide.
- Formation compatibility: Fracturing fluids should be compatible with the formation, formation fluids and matrix minerals to reduce fracture conductivity damage induced by chemical reactions.
- Gel Residue: Fluid residue that remains in the fracture after clean-up can block the pathway of fluids. Usually the risk increases with higher viscosity fluids such as cross link gels.
- Fluid Leak-off: Optimum fluid leakoff should be achieved by the fluid so that secondary fractures are created to increase stimulated reservoir volume and the fractures are also cleaned up.
- Fluid Flowback: One of the most important parameters to consider is the fluid recovery efficiency.
- Proppant Transport: The ability of the fluid to transport proppants to the fracture. Fluids with higher viscosity are usually used with larger size proppants.

It is apparent that selecting the optimum fluid is not an easy process, as it is impossible to meet all the criteria listed above. Fracture fluid additives could aid in achieving all the criteria required to achieve a successful hydraulic fracture treatment. Examples of commonly used additives are corrosion inhibitor to prevent the corrosion of tubing, casing and tanks; biocides to reduce bacterial corrosion; potassium chloride to reduce clay swelling and stabilize the clay-water reactions; and breaker to decrease fluid viscosity for better proppant settling and more efficient flowback.

2.3.2 Proppant Selection

Proppants are an essential component of hydraulic fracture design as their selection alone has an effect on overall job economics, treatment size and well productivity. Knowledge of the various types of proppants available and their characteristics will aid in their selection for fracture design jobs.

There are four different types of proppants that are well known in industry: sand, ceramic, resin coated sand and ceramic. The different types of proppants vary in crush resistance and roundness and sphericity. Sands, which are low strength proppants, are irregular in shape and size, with roundness and sphericity ranging from 0.5-0.7. Ceramic proppants generally exhibit higher strength than sands and are more uniform in size and shape with higher roundness and sphericity of 0.8-0.9 (Kullman 2011). Thus, when selecting proppants for a hydraulic fracture treatment, a completion engineer should look into formation characteristics such as closure pressure and mineralogy. For example, in the Vaca Muerta formation where closure pressure exceeds 9000 psi, due to their higher closure pressures, ceramic proppants are used in hydraulic fracture treatments. An illustration of properties per proppant type and respective level of expected conductivity is shown in Figure 2.4.

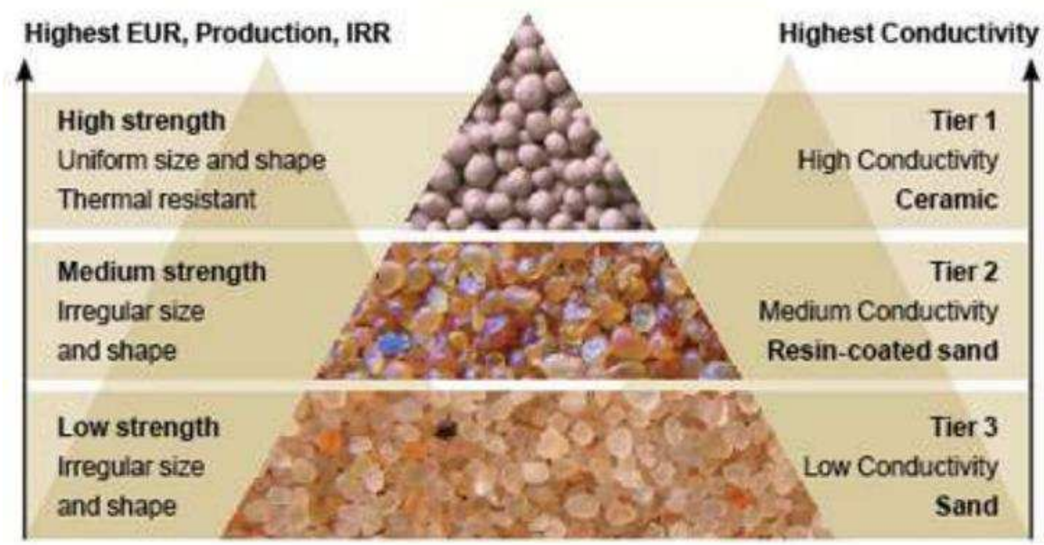

Figure 2.4: The three different proppant types, their properties and expected level of conductivity (http://images.sdsmt.edu/learn/speakerpresentations/Kullman.pdf).

Conductivity varies with the size of proppants. Proppant particle size is described in terms of sieve distribution. A 20/40 proppant will range in size between 20 mesh (0.841 mm diameter) and 40 mesh (0.4 mm). A 40/70 proppant will have a smaller diameter size range between 40 mesh (0.463 mm) and 70 mesh (0.21 mm) (Miskimins 2015).

The permeability of a proppant pack is also dependent on the packing arrangement of proppants. The packing arrangement varies from one material to another. As the stress applied to the proppant pack increases, its packing geometry is expected to change. Proppants with higher values of roundness and sphericity are expected to exhibit better packing conditions by withstanding higher closure stress (Baree et al. 2003). An illustration of how the different proppants look like in terms of roundness and sphericity is provided in Figure 2.5.

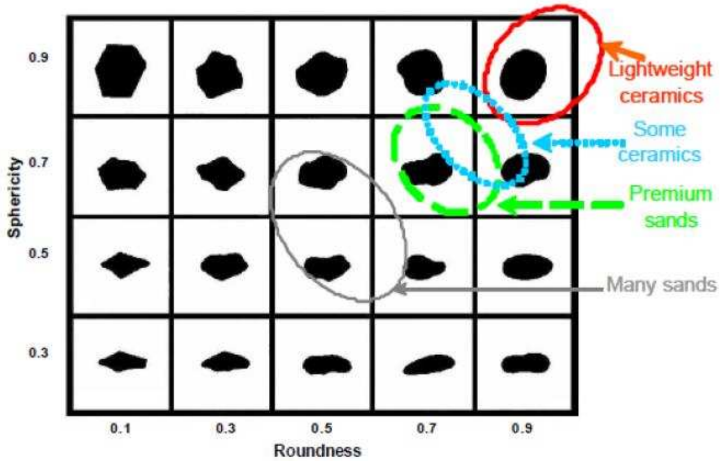

Figure 2.5: Roundness and sphericity of the different types of proppants (Vincent et al. 2004).

2.3.3 Proppant Transport and Distribution

There is a lot of uncertainty about proppant distribution within the fracture. Three different scenarios are possible for proppant transport in fractures and are shown in Figure 2.6: proppants spread evenly through the complex fracture network, proppants become concentrated in the main fracture or they settle and form pillars throughout the complex fracture network (Cipolla et al. 2010).

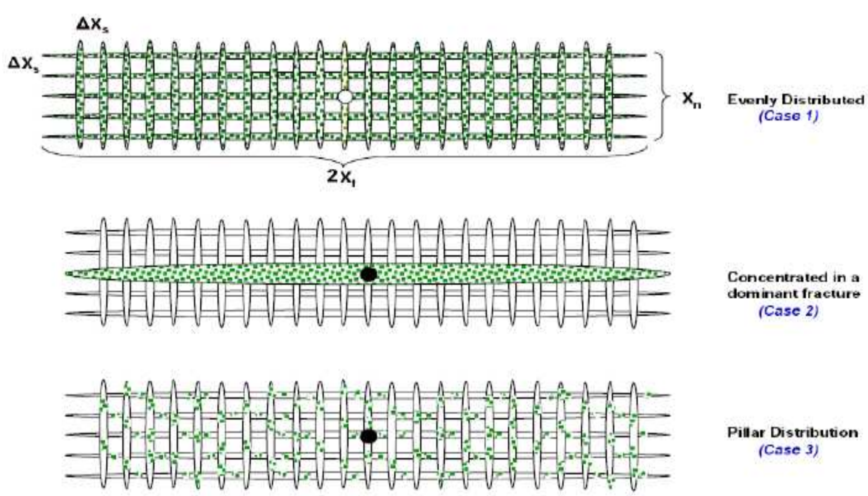

Figure 2.6: The three possible proppant transportation distribution scenarios in complex fracture systems from the top view. The dot in the middle is a symbol for the well (Cipolla et al. 2010).

The distribution of proppants throughout the fracture is a strong determiner of the fracture conductivity. Baree et al. (2003) stated that the original packing distribution of proppants causes the highest variation in fracture width. Many factors play a role in controlling the proppant distribution such as closure stress, physical and formation properties, fluid specific gravity, fluid viscosity, proppant size, proppant specific gravity and pumping rate. The force of gravity can result in the uneven distribution of proppants where they are concentrated in the bottom of the fracture as displayed in the left side of Figure 2.7. This may lead to the closing of fractures and a great reduction in fracture conductivity. As shown in Figure 2.7, the effect of gravity is stronger on vertical fractures as closure portions could be closed blocking flow of fluids. High viscosity fluid can help reduce the problem by better supporting the proppants against gravitational forces. In natural fractures or fractures with high asperity, proppants can settle in certain parts of the fracture due to gravitational forces, allowing the closure of the fracture in the other parts as shown in the right side of Figure 2.7. Due to the roughness and irregularity of fractures, proppants can move more easily and build packs, as a result of tensile and shear fracturing (Daneshy 2007). The even distribution of proppants reduces the likeliness of fracture closure. The effect of proppant distribution on conductivity is investigated in this research study.

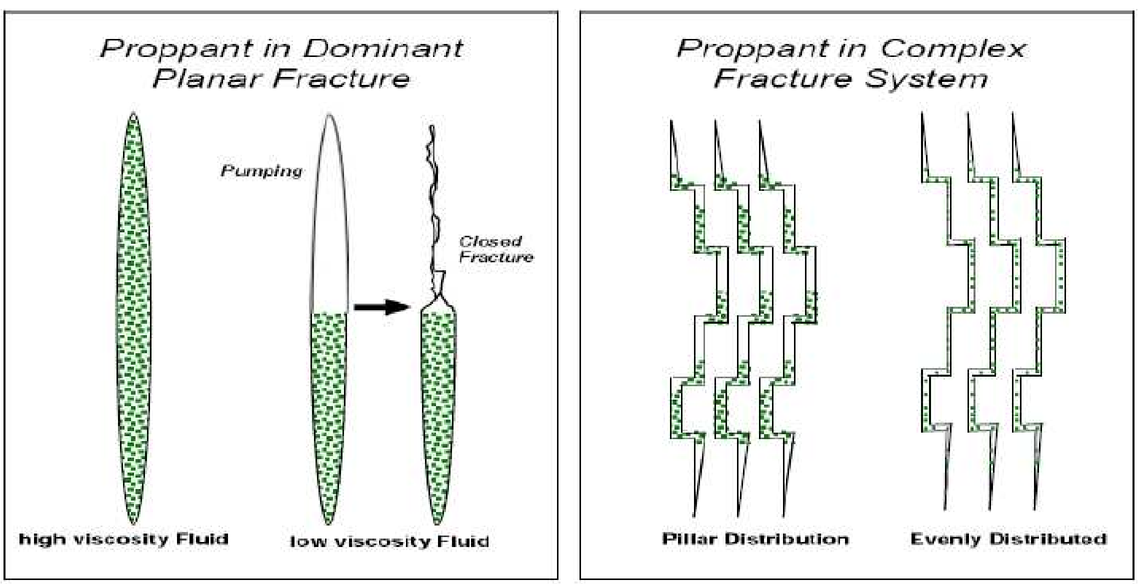

Figure 2.7: Side view of proppant distribution scenarios in planar (left side) and complex (right side) vertical fracture systems (Cipolla et al. 2010).

In case of horizontal fractures or more complex fracture systems, the flowrate of proppant is an important factor affecting its distribution. A threshold flowrate should be achieved and maintained for proper proppant distribution around a horizontal fracture. Otherwise, proppants could develop beds and/or packs or become loosely distributed, negatively affecting conductivity (Sahai 2012).

Proppants could be distributed in the form of a monolayer, multilayer or a partial layer distribution. The term monolayer is used when proppants are distributed in a single layer (Figure 2.8), which is very unlikely due to the turbulent fluid flow effects. Proppants are expected to move around with fluids and settle in time. Proppants distributed in a mono- layer are more prone to embedment as they are subjected to stress at only a single layer, which causes a reduction in conductivity. Wider fractures could be created with multilayer distribution at which proppants are randomly scattered and packed along the fracture face. Improved conductivity could be achieved with increased fracture width due to multiple layers of proppants. However, with multiple layers of proppant, there is a risk of proppant crushing as proppants are stacked over one another. To reduce the problems that are encountered with mono and multilayer distributions, the idea of a "partial monolayer' was introduced (Figure 2.8). In a practical sense, it is difficult for proppants to distribute in a partial mono- layer in vertical fractures. The idea of this type of distribution is purely theoretical, based on the belief that the spaces between proppants can vastly improve conductivity (Palisch et al. 2008).

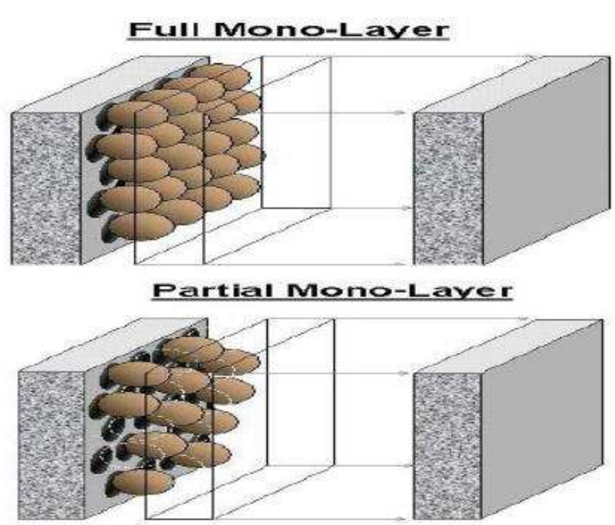

Figure 2.8: Illustration of full and partial monolayer on the fracture surface (Brannon et al. 2004).

2.3.4 Damage Mechanisms

Damage mechanisms that can occur downhole can also cause the reduction of proppant pack conductivity. A thorough investigation of the damage mechanisms that might occur under field conditions and their impact on conductivity must be performed before selecting proppants to be used in a fracture treatment. Several of these damage mechanisms that could be investigated experimentally are explained in this section and they include proppant embedment, formation spalling, proppant resistance to cyclic stress changes and proppants fines migration.

Proppant embedment occurs as proppants embed into the fracture face. The external proppant pack width is reduced by the effect of proppant embedment, causing a reduction in the flow capacity of the fracture as illustrated in Figure 2.9. Embedment losses are more significant in softer formations such as shale (Penny 1987).

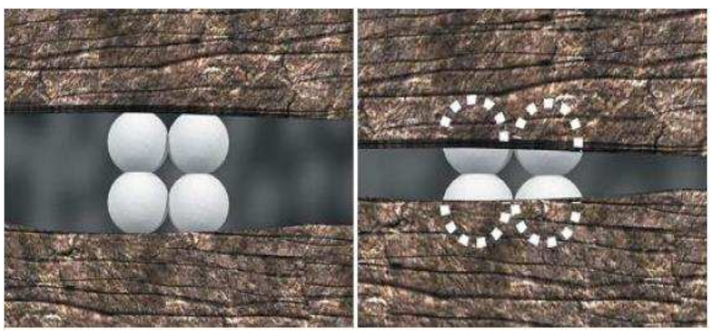

Figure 2.9: Proppant embedment leading to a decrease in fracture width and conductivity (Terracina et al. 2010).

Spalling is defined as the extrusion of formation material into the proppant pack. Formation spalling into the proppant pack is usually a consequence of proppant embedment. It occurs as formation fines or crushed particles are generated as the hard proppant grains are forced into the fracture wall. The combined process of embedment and spalling is shown in Figure 2.10.

Proppants fines can also be generated as the fracture is subjected to closure stress and downhole temperature (Figure 2.11). Small particles of proppant break off the proppants grains, reducing the proppant pack permeability and porosity. A great deal of conductivity is lost during the process of proppant generation and migration. According to Coulter and Wells (1972) as little as 5% proppant fines could reduce proppant pack conductivity by 62%. Proppant fines could migrate down the proppant pack towards the wellbore and accumulate and limit fluid flow, further reducing fracture conductivity (Terracina et al. 2010).

Figure 2.10: Formation fines spalling (circled) due to grain embedment (Baree et al. 2003).

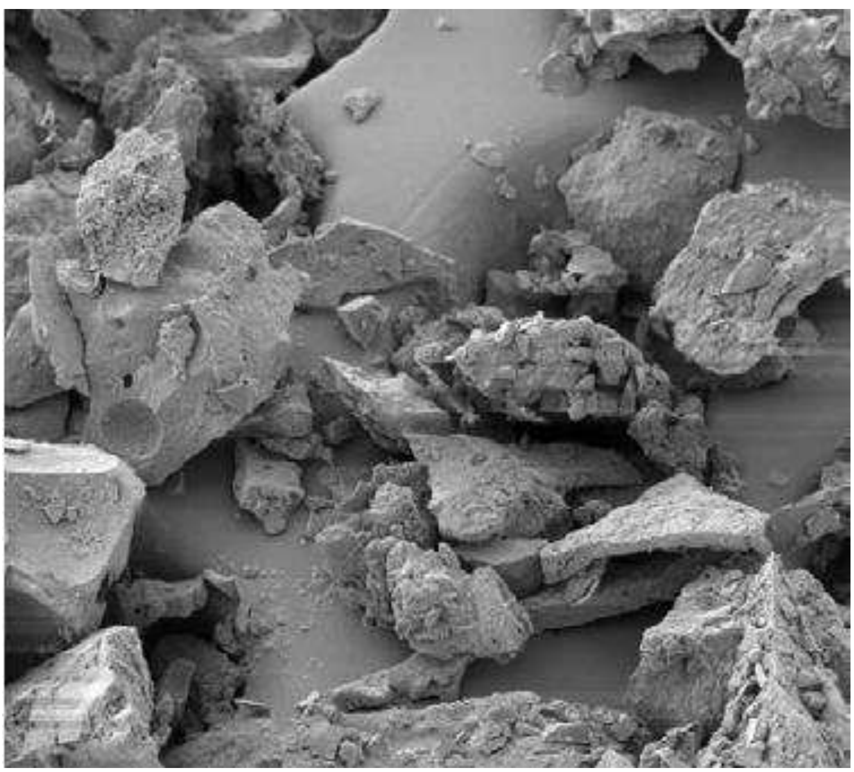

Figure 2.11: Scanning Electron Microscope (SEM) image (404x) of 40/80 mesh ceramic proppant that has produced fines (Terracina et al. 2010).

When the proppants are subjected to closure stress changes due to field operations such as shut-ins due to pipeline capacity or workovers and connections to pipelines, they can fail. The changes in pressure and stress applied to the proppant can lead to their redistribution, resulting in the reduction of the fracture width, additional fines generation and proppant flowback. Cyclic stress is usually not simulated in laboratory conditions, although it has a significant impact on fracture conductivity. Shut-ins of fractured wells can lead to the reduction of production rate after the shut-in period due to lower fractured conductivity and decreased fracture width (Kim and Willingham 1987). It was reported by Freeman et al. (2009) that the amount of fines generated increased by 22.6% after only 4 stress cycles.

There are other damage mechanisms that contribute to fracture conductivity damage at field conditions, but are difficult to measure experimentally (Baree et al. 2003).

- Non-Darcy flow
- Multiphase flow
- Multiphase non-Darcy flow
- Gravity and viscous segregation
- Reservoir flow capacity

2.4 Fluid Flow in Fractures

Darcy's law is used in industry to calculate fracture permeability from pressure drop and flow through the propped fracture recorded in the lab (Duenckel et al., 2016). Darcy's law assumes a linear relationship between pressure drop and flow rate (Equation 2.11).

$$\frac{dp}{dl} = \frac{\mu v}{k} \tag{2.11}$$

The limitation of Darcy's law is that with higher velocities, an apparent decrease in flow capacity is observed. Thus, calculated permeability values in will vary with different flow rates. To encounter the problem of non-linearity between flow rate and pressure gradient at high fluid velocity, Forchheimer (1914) presented an empirical equation to account for non-linear flow behavior (Equation 2.12). Forchheimer attributed the non-linear increase in pressure gradient with higher velocities to inertial losses in the porous medium that which are proportional to ρv^2. The first term in Forchheimer's equation $\mu v/k$ describes the Darcy linear pressure gradient. The second term term which describes the non-linearity, is described by the fluid density, the square of interstitial velocity and β which is a contrived proportionality constant with units 1/ft.

$$\frac{dp}{dl} = \frac{\mu v}{k} + \beta \rho v^2 \tag{2.12}$$

Forchheimer's equation assumes that Darcy's law is still valid, but an additional pressure drop should be included. The additional pressure drop was derived from empirical observations that when $1/k_{app}$ (permeability values obtained using Darcy's law) is plotted against $\rho v/\mu$, a linear relationship is obtained.The permeability could then be calculated from the intercept $1/k_d$.

$$\frac{1}{k_{app}} = \frac{1}{k_d} + \beta \rho v \tag{2.13}$$

By rearranging Equation 2.13, a linear relationship between flow rate q and $1/k_{app}$ is obtained as shown in Equation 2.14.

$$\frac{1}{k_{app}} = \frac{1}{k_d} + \frac{\beta \rho}{A} q \tag{2.14}$$

2.5 Conductivity Testing

As hydraulic fracturing became a popular method of stimulation, interest in evaluating proppant performance began to grow. Several methods to test proppant conductivity in industry arose with the attempt to simulate proppant performance in a hydraulic fracture. The American Petroleum Institute (API) issued the first industry standard to measure the proppant pack conductivity. API RP61 (API 1989) called "Recommended Practices for Evaluating Short Term Conductivity" is considered a "short term conductivity" test. The measuring apparatus and its constituents are described in Figure 2.12. Duenckel et al. (2016) summarize the methodology and the experimental apparatus in the following points:

- 10 inch square flow path (1.5w×7.0 inch cell)
- Deionized or distilled water flowed through the proppant pack
- Performed at room temperature (75°F +/- 5°F)
- Proppant loaded at a concentration of 2 lbm/ft^2 or 0.25 inch width
- Proppant is confined between steel platens
- Each stress is applied to the proppant for 15 minutes
- Stresses applied vary with the type and size of proppant
- Stress ranged from 1 to 14k psi

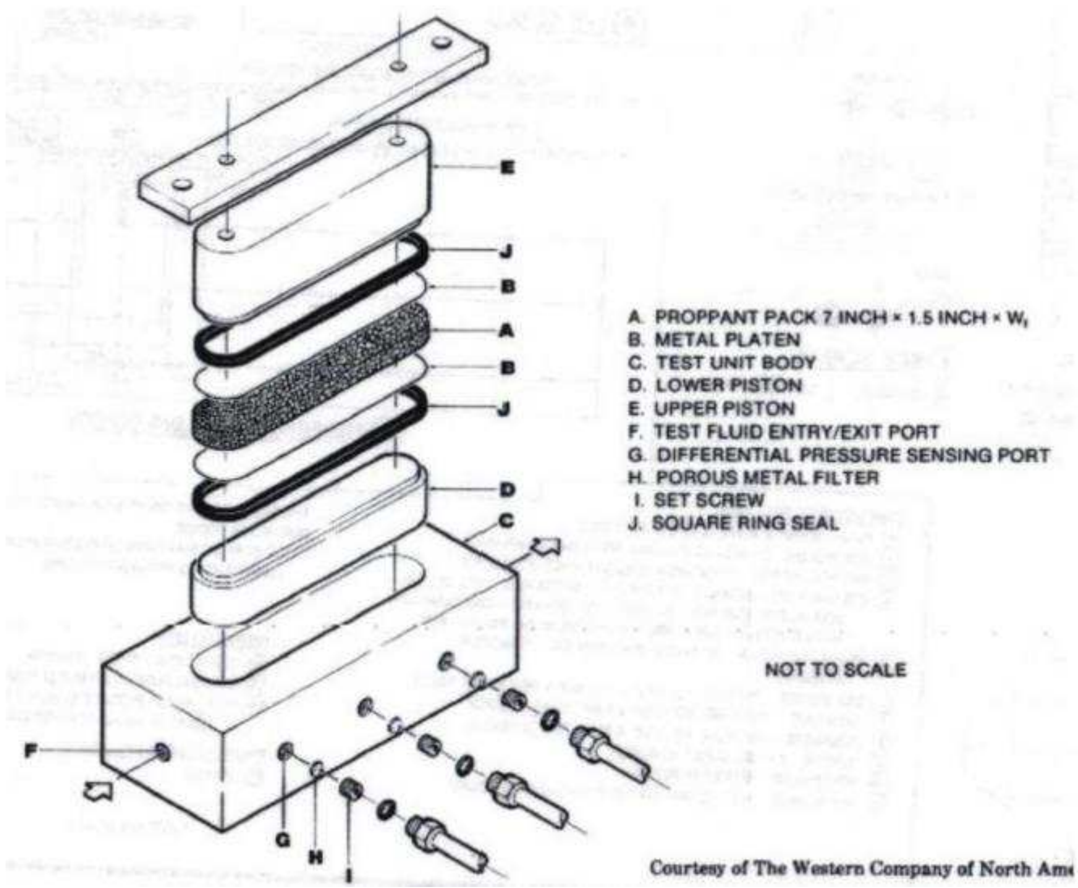

Figure 2.12: API short term conductivity apparatus (API 1989).

The tests conducted using the setup in the previous figure have several limitations that are clearly stated in the API RP 61 document. In the document, it was explained that the conductivity values obtained from these types of experiments do not represent values under reservoir downhole conditions. Furthermore, 15 minutes of applied stress is not sufficient to quantify the reduction in fracture "long term conductivity" which could amount to 90% additional reduction in conductivity. The term long term conductivity refers to the conductivity loss with time (several days) and due to elevated temperature and the damage mechanisms described in the previous section. To address all the issues faced with short term conductivity tests, Penny (1987) proposed the following changes to the short term conductivity test:

- Stainless steel platens were replaced with a sandstone core sample to allow for the measure of proppant embedment
- Deionized water was replaced with 2% KCl. In addition, the sandstone sample was saturated with silica to prevent its dissolution

- Stress was applied for 50 hours, instead of 15 minutes, based on past observations that conductivity decreased rapidly initially then started to stabilize between 50-100 hours
- Tests were run at temperatures close to downhole temperatures of 150-250 F

The above procedures soon became an industry standard to measure "long term" conductivity, outlined in API RP19D (API 2008). The test is used as a basis to compare the performance of different proppants provided by the various suppliers within industry. The API RP19D document contains some instructions on how to take measurements and load proppant onto the sample. The document recognizes that the measurement of conductivity could be modified to obtain improved test results: "The procedures presented in this publication are not intended to inhibit the development of new technology, materials improvement, or improved operational procedures. Qualified engineering analysis and sound judgment is required for their application for a specific situation." In fact, testing procedures have been modified by some researchers to obtain different experimental objectives such as investigating effect of interaction of the formation with various fluids and the effect of mechanical properties on fracture conductivity. Some of these tests are discussed in this section, due to their relevance to this research study.

Alramahi and Sundberg (2012) conducted experiments to investigate the relationship between proppant embedment and fracture conductivity in formations with different mineralogy. The experiment designed to measure embedment was separate from the one that measures fracture conductivity. The embedment experiment consisted of a transparent cylindrical tube where the samples were placed (Figure 2.13). Proppant was placed on the shale sample and increasing uniaxial stress was applied. Deformation was then measured using 2 LVDTs as the stress increased. The experiment performed to measure conductivity was performed by applying increasing confining stress to a fractured core sample and flowing fluid through it to measure fracture conductivity as shown in Figure 2.14. The same shale samples, proppant sizes, concentrations, and fluid chemistry used in the embedment experiments were used in the conductivity experiment.

Alramahi and Sundberg's (2012) results showed that embedment and conductivity loss increase with stress. More embedment and conductivity loss were experienced in samples with higher clay content and lower Young's modulus (Figure 2.15).

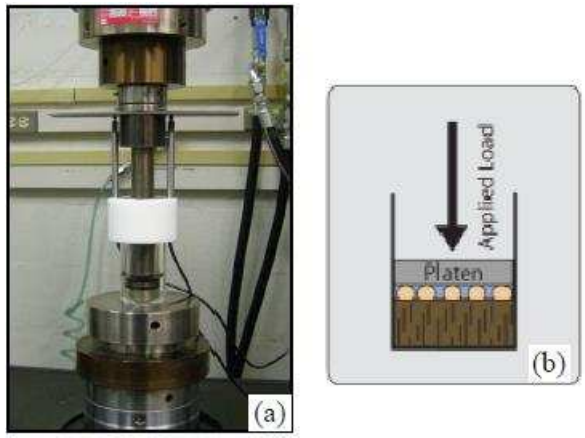

Figure 2.13: (a) Proppant embedment apparatus, (b) illustration of how proppant are loaded onto sample and the applied stress (Alramahi and Sundberg 2012).

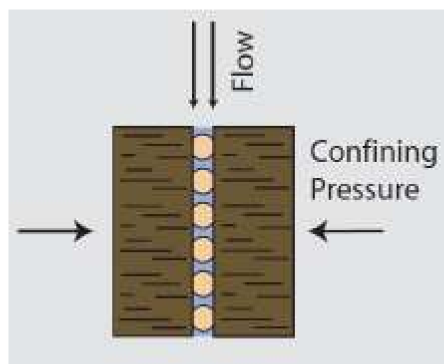

Figure 2.14: Description of the conductivity experiment (Alramahi and Sundberg 2012).

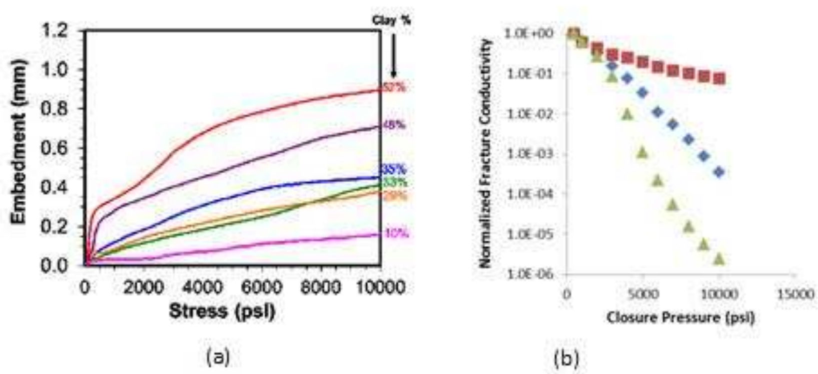

Figure 2.15: (a) Embedment vs. closure stress, showing that embedment increases significantly with clay content. (b) Reduction in conductivity with increase in closure stress, the red and blue curves represent results for stiffer samples (Alramahi and Sundberg 2012).

Similar experiments were performed while maintaining the fracture asperity. Jansen and Zhu (2015) performed unpropped and propped fracture conductivity tests on samples with different fracture roughness and mechanical properties. They concluded that increased fractured roughness provides a higher initial flow path for fluids, but as the proppant concentration increases proppant properties such as packing and strength become the stronger contributing factor to fracture conductivity. Similar finding were presented by Kamenov et al. (2013), Guzek (2014) and Briggs (2014) for Barnett, Eagle Ford and Fayetteville shale samples respectively.

Other researchers carried out experiments to find relationships between conductivity degradation and rock fluid interactions. Akrad et al. (2011) investigated the impact of a exposing samples with variable mineralogy (Figure 2.16) to a mixture of 2% KCl brine and friction reducer for different time periods and different temperatures. Nanoindentation technology was used to obtain the Young's modulus before and after fluid saturation. Uniaxial stress was then applied on those samples to test for embedment. The results showed that Young's modulus decreased with exposure to fluid; decrease in Young's Modulus was the most in calcite rich shales and was more in samples that were saturated at downhole temperature. This decrease caused an increase in embedment and therefore a decrease in fracture conductivity.

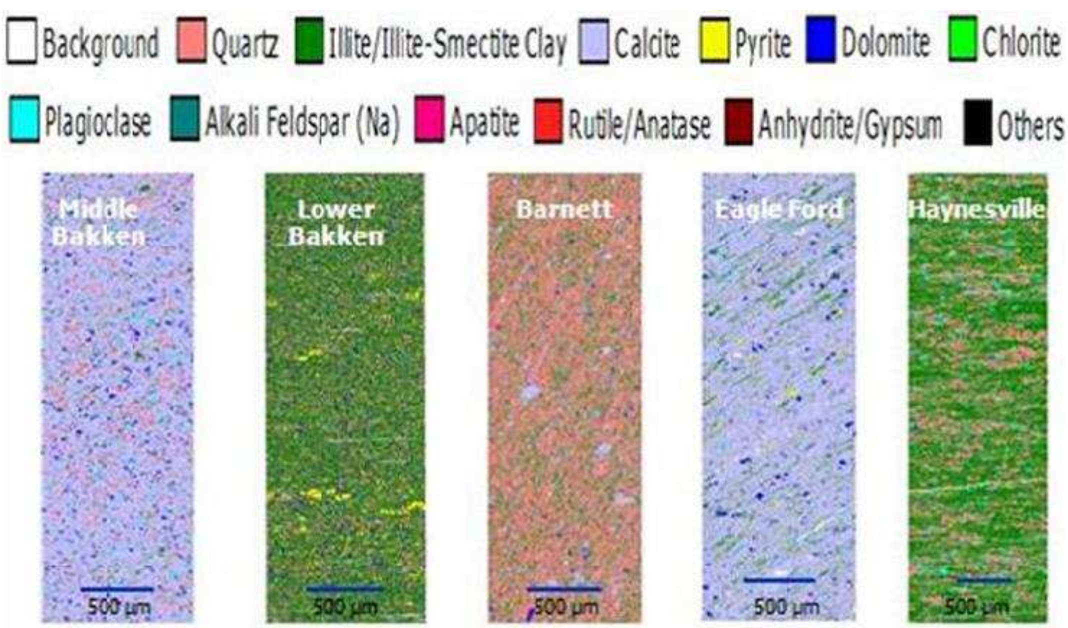

Figure 2.16: QEMSCAN image showing the different mineralogy of samples that were studied (Akrad et al. 2011).

Pedlow and Sharma (2014) used a core flooding apparatus that simultaneously measures fracture permeability. Samples with different mineralogy were tested with different fluids such as 3.5% NaCl and 3%wt KCl. Long term fracture permeability was tested for some of the samples. They concluded that samples with clay content higher than 20% are more fluid sensitive and more prone to conductivity loss due to stress exposure even at stress just greater than 500 psi. Moreover, they pointed out the significance of proppant fines generation on conductivity reduction.

CHAPTER 3

EQUIPMENT AND METHODS

The research study focuses on the effect of stress and fluid interactions on fracture conductivity, wave velocity propagation and geomechanical properties. Detailed procedures and methods used to achieve these objectives are discussed in this chapter.

3.1 Research Plan

Samples were obtained from the 18 m full core from the LJE.x-1010 well that was described in more detail in Chapter 1. Fractures in core plugs were induced parallel to the natural bedding planes to obtain a more realistic rough surface. A flowchart outlining the main steps that were necessary to complete this research are explained in Figure 3.1.

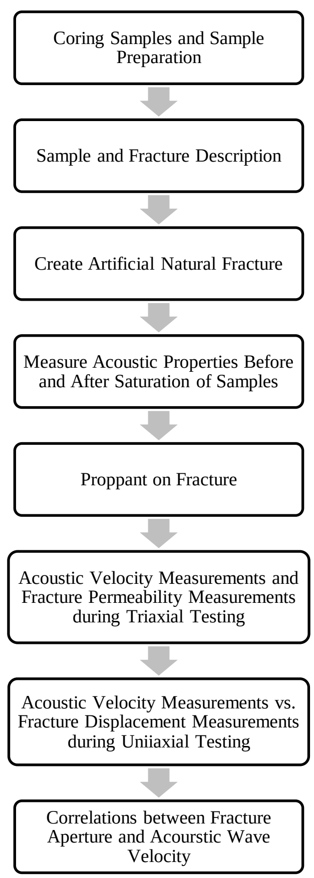

Figure 3.1: Flowchart of experimental procedure.

3.2 Sample Preparation

Core preparation starts from coring the sample plug from the full core to fracturing them. Before coring the samples out of the available full core, a core depth interval had to be selected for analysis and experimentation. The shallowest core depth section available (measured depth of 3094 m) was chosen, as it is the closest depth to the base of the lower Vaca Muerta, which was suggested by Willis (2013) as a sweet spot for horizontal well placement. The base of the lower Vaca Muerta was also identified as a play flag according to analysis performed on Mangrove, based on cut off values from TOC, mineralogy, resistivity and calculated dynamic Young's Modulus logs.

Core sections were drilled parallel to bedding into 1.5 inch core plugs. This orientation was selected in order to have fracture creation in the sample to be in the direction of the maximum horizontal stress, representative of the hydraulic fractures in horizontal wells. These core plugs were then cut using a diamond saw to obtain a core plug length of 0.7 inch, with smooth surfaces. However, the core surfaces need to be precisely parallel to ensure the equal distribution of stresses during triaxial testing to obtain reliable wave velocity data and to avoid unwanted weakening due to stress concentration due to uneven surfaces. This is achieved by grinding the core plugs using a surface grinder that could sand the surfaces up to ±0.01 mm. Samples have been clamped using a Clamped Starrett V-Block, which is placed on a magnetic X-Y table under the sanding disk. The table rotates to sand the core surface until a flat surface is obtained. Samples were smoothed using fine sand paper.

After ensuring that samples were well prepared for triaxial testing, they were fractured prior to proppant placement. Use of high pressure for fracturing caused shattering of the core samples (Figure 3.2). Therefore, stress was applied on the sample in the axial direction using a vice combined with a sharp metallic edge (Figure 3.3). The final outcome was fractured cores with parallel smooth surfaces, shown in Figure 3.4.

A similar procedure was applied to prepare samples for the uniaxial test; except that the sample was a cube and that a the Brazilian test was successfully performed to create a fracture along the sample as shown in Figure 3.5.

Figure 3.2: Unsuccessful attempt to fracture core samples using Pressure Press.

Figure 3.3: Core plug fracturing method used.

3.3 Sample Analysis

Several rock analysis methods were performed to better understand the properties of the formation in relating them to the experimental results. Mineralogical analysis using X-ray diffraction (XRD), fracture characterization using computerized tomography (CT-Scan) and topography imaging using field emission scanning electron microscopy (FE-SEM) have been conducted before and after the experiments.

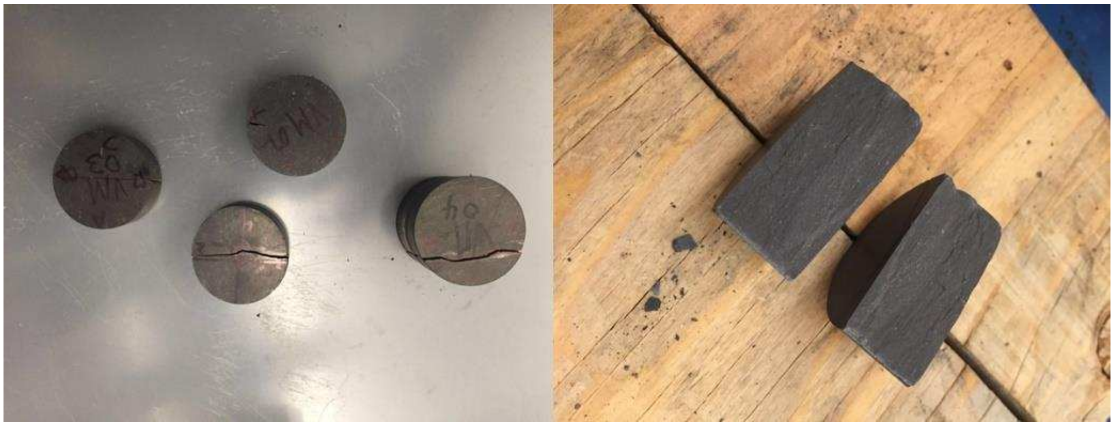

Figure 3.4: Unpropped fractured samples, with rough fracture surface.

Figure 3.5: Brazilian test to create fracture in the sample used in the uniaxial stress propped fracture conductivity test.

3.3.1 Sample Mineralogy

X-ray diffraction was required, as the prior mineralogy data did not include mineralogical composition of the section depth being investigated in this study.

3.3.2 Fracture Characterization

Computerized tomography (CT-Scan) measurements are used to look at the fracture intensity present in the samples. Checking the presence of fractures in the samples could help in understanding of the wave acoustic velocity data obtained before and after the saturation of the samples and during triaxial testing.

3.3.3 Field Emission Scanning Electron Microscopy (FE-SEM)

Field emission scanning electron microscopy (FE-SEM) could capture the topographical variation in the sample, providing a clear image with magnifications up to 300,000X. Imaging was performed before the conductivity test to be able to describe by comparison with the image of the undamaged core, the fracture damage due to damage mechanisms such as embedment and spalling by comparing before and after scans.

3.4 Measurement of Sample Mechanical Properties Before and After Saturation

This step was performed in order to quantify the mechanical degradation of samples due to interaction with fracture fluids. The samples where saturated with 2% KCl water, to represent the common slick water base fluid, widely used in fracturing shale formations, including the wells in the Vaca Muerta formation. Dynamic mechanical properties of the samples were calculated before and after saturation using wave velocity measurements.

3.4.1 Core Saturation

The saturation of core samples involves the following steps:

1) Placement of samples in a sealed desiccator vacuum chamber connected to a vacuum pump (Figure 3.6), until vacuum pressure is achieved. Samples were maintained at vacuum pressure for a week to release air trapped in pores and fractures.

2) Degassed deionized water with 2% KCl concentration was sucked to the desiccator through sealed vacuum tubing, while ensuring that vacuum pressure is maintained by monitoring the gauge

reading.

3) Samples were left inside a beaker within the desiccator, filled with the saturation fluid, at vacuum pressure for 30 days.

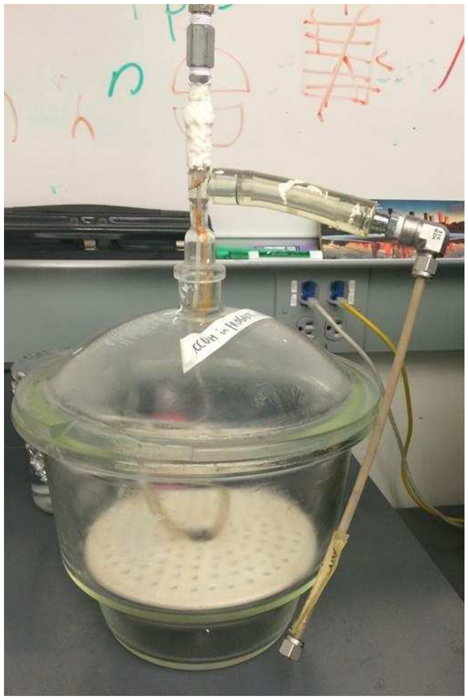

Figure 3.6: Vacuum chamber where core plugs were saturated with 2% KCl.

3.4.2 Wave Velocity Measurements

Elastic wave propagation measurements are useful to determine formation properties in core scale as well as in the field through sonic logs or seismic. Elastic waves are mechanical disturbances generated by particle movement that allow for energy movement through the sample, without it being displaced. Compressional waves (P-wave) particle motion is parallel to the direction of wave propagation while in shear waves (S-wave), the motion is perpendicular to the direction of wave propagation (Stein and Wysession, 2003) (Figure 3.7). Due to the fact that particle vibration in S-waves takes place on a plane normal to the direction of particle propagation, the direction of vibration on that plane or polarization can vary. S-waves consist of vertically (SV) and horizontally (SH) polarized components. Intrinsic rock properties such as fracture intensity, grain orientation and external factors such as stress influence the wave propagation. Due to the difference in the nature of the particle motion propagation in P-waves and S-waves, they respond differently to those factors.

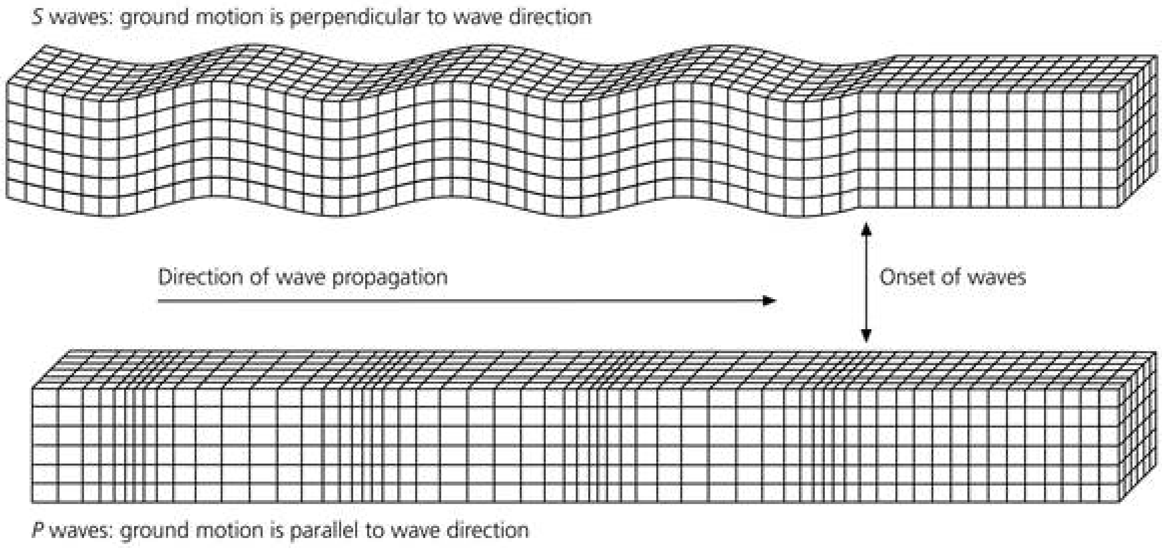

Figure 3.7: Illustration of S and P wave direction with reference to direction particle propagation (Stein and Wysession 2003).

Ultrasonic wave velocity measurements on saturated and non-saturated core samples have been performed using two “Olympus Model 5058PR” piezoelectric transducers of 1 MHz central frequency. The transducers transform electric pulses into mechanical pulses and vice-versa and are shown in Figure 3.8. Using a pulse generator, a high voltage, short duration (ultrasonic frequency) electrical pulse is applied to one of the transducers, resulting in compressional and shear wave propagation. The core sample before and after saturation has been placed between the transmitter and receiver transducers, as the electric pulse transmits through it in form of the elastic waves. The receiving transducer transforms the wave into an electric signal that transmits through P and S wave cables to a digital oscilloscope connected to the pulser/receiver connected to a computer for data acquisition. An image of the pulser and receiver and oscilloscope is shown in Figure 3.9. The data acquisition system is explained in further detail in the latter sections. It must be noted that transmitter and receiver transducers are aligned at zero polarization to avoid variations in shear wave data due to change in polarization. Based on the arrival times of the compressional and shear pulses, P-wave and S-wave velocities have been calculated. Measurements were taken at several points within the surface of the core to reduce uncertainty of measurements.

Prior to core sample measurement, calibration was performed by face-to-face measurements to determine accurate arrival time for the signal in the core sample during the wave propagation measurements.

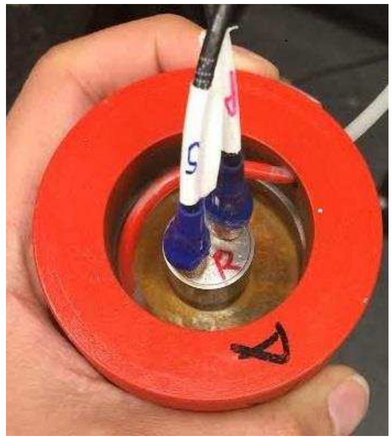

Figure 3.8: One the piezoelectric transducers used to measure elastic wave velocity through sample.

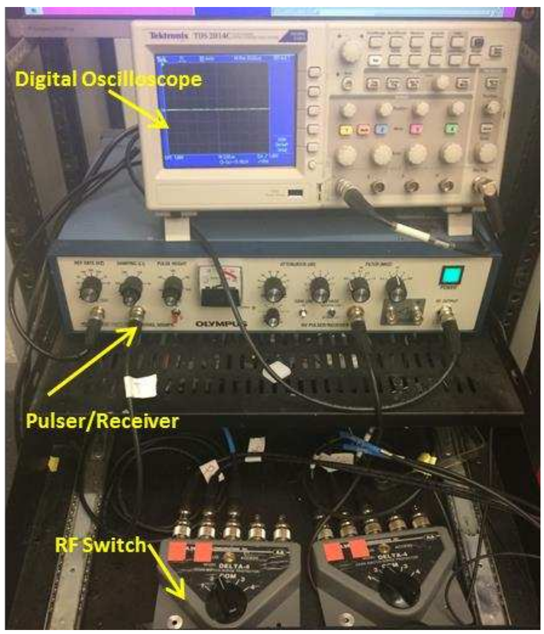

Figure 3.9: Digital Oscilloscope, pulser/receiver and RF switch for selecting the measurement of P or S wave velocity.

3.4.3 Determination of Sample Mechanical Properties from Acoustic Wave Measurements

The following calculation steps were performed to obtain Young's Modulus and Poisson's before and after saturation of the sample.

1. Picking the arrival times from the recorded wave velocity data. Selecting the arrival times could be challenging as it may be difficult to distinguish noise from actual wave data. A guideline for picking arrival times for P and S waves is provided in Figure 3.10.

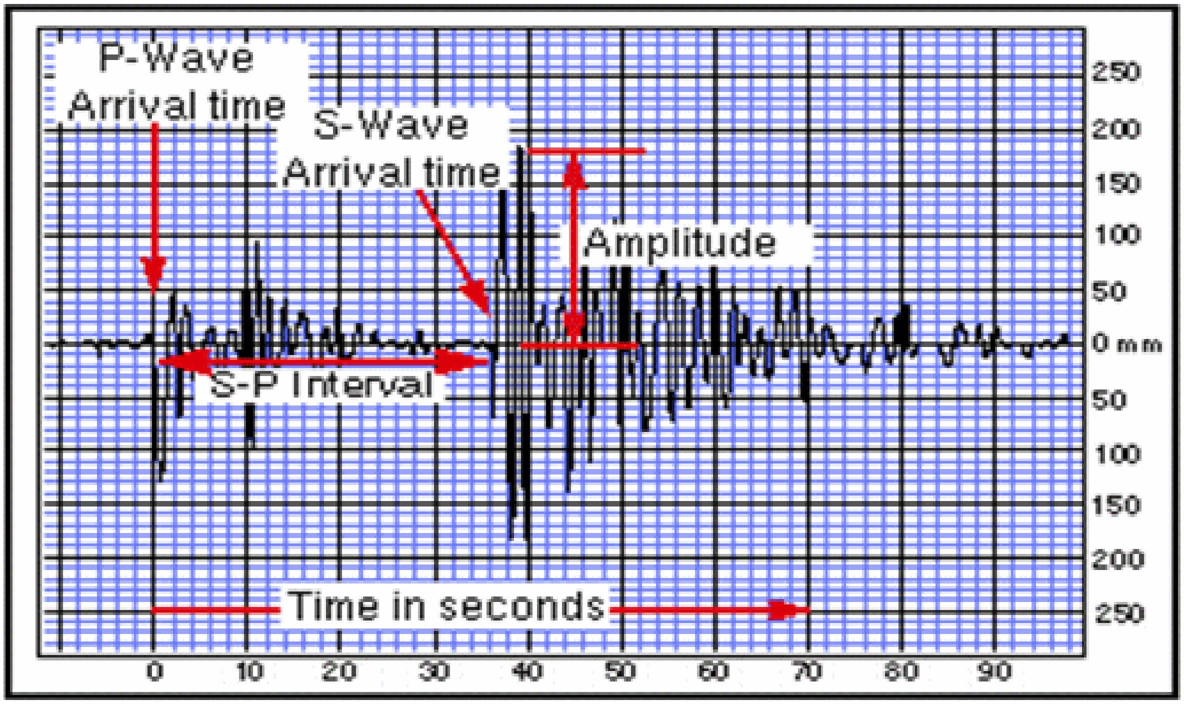

Figure 3.10: Guideline to picking arrival time for P-wave and S-wave.

The following calculations have been performed to evaluate the mechanical properties of the sample:

To arrive with compressional V_p and shear V_s wave velocities the captured respective arrival time is simply divided by the length of the sample l as shown in Equation 3.1.

$$V_p/V_s = \frac{l}{t_{arrVp\ /Vs}} \tag{3.1}$$

The dynamic Young's modulus E_{dyn} and dynamic Poisson's ratio v_{dyn} were calculated as described in Equations 3.2 and 3.3 respectively:

$$E_{dyn} = \rho V_s^2 \left(\frac{3V_p^2 - 4V_s^2}{V_p^2 - V_s^2} \right) \tag{3.2}$$

$$V_{dyn} = \frac{V_p^2 - 2V_s^2}{2(V_p^2 - V_s^2)} \tag{3.3}$$

3.5 Proppant in Fracture

Size 20 mesh ceramic proppant was selected as the proppant to be used in the conductivity tests due its large size for better visibility in the embedment tests when analyzing the experimental data. Using a single size of proppant in the experiments would help in determining proper relations between proppant size and conductivity damage. In addition, according to the pump data available, the same type and size of proppant has been reported to be used in stimulating the wells in the Vaca Muerta formation. The option of using sand instead of ceramic proppant was not viable due to the high closure pressures exhibited in the formation, determined through diagnostic fracture injection tests provided by the consortium sponsors. The desired size was sieved out of the 20/40 mesh proppant supplied from CoorsTek. A sieve was used to separate the 20 mesh size allowing smaller proppant to drop to the bottom and blocks the movement of the required size. For better sieving, the sieve was placed on a dental vibrator to further separate the 20 mesh proppant from the smaller sizes as illustrated in Figure 3.11.

Figure 3.11: Proppant sieve on a dental vibrator for better sieving of the proppant.

A monolayer of proppant was placed on the fracture face on one of the halves of the samples used in triaxial and uniaxial tests using tweezers to allow for for proper packing. A heavy syrup was used to stick the proppant to the surface (Figure 3.12). This syrup has the advantage of being soluble in water so as not to block the flow lines as fluids flow through the fracture during permeability tests.

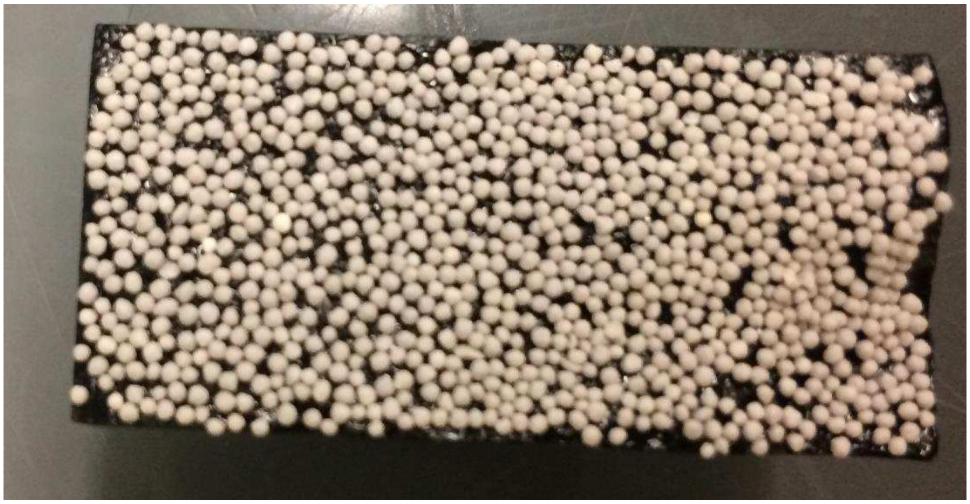

Figure 3.12: Proppant placement on the fracture face before fracture conductivity measurements.

3.6 Uniaxial Stress Test for Fracture Aperture Calculation

The uniaxial test was performed to estimate the fracture aperture to be used in for fracture permeability calculations as described in more detail in the following chapter. It was decided to perform the test since fracture displacement measurements are not attainable in the triaxial cell.

3.6.1 Apparatus

The servo-controlled hydraulic loading frame made by MTS was used to perform the uniaxial test. This frame can apply compression and tensile forces up to 250 kN to the test sample. The servo system is capable of generating monotonic and oscillatory functions of the axial force and the displacement. All the operation commands of servo-system can be handled from a software. The software provides real time data plots of displacement versus applied stress. The shortest data sampling interval is 0.1 second. The system could be used to test rock samples for indirect tensile strength, uniaxial compression strength, triaxial compression strength, and creep behavior.

3.6.2 Testing Procedure

Load was applied in steps to the cubic sample fractured sample filled with proppant as the displacement was recorded in real time Figure 3.13. The steps of the load applied are equal to the effective confining stress steps applied to the sample during the triaxial test *P*. This is achieved by multiplying the stress values by the area cross section of the cubic sample subjected to the load A to calculate F (lbf) (Equation 3.4).

$$F = P\,A \tag{3.4}$$

When the displacement stabilized (stopped changing) for each step, acoustic wave velocity measurements were taken; P-wave, S-wave perpendicular and parallel to the fracture plane.

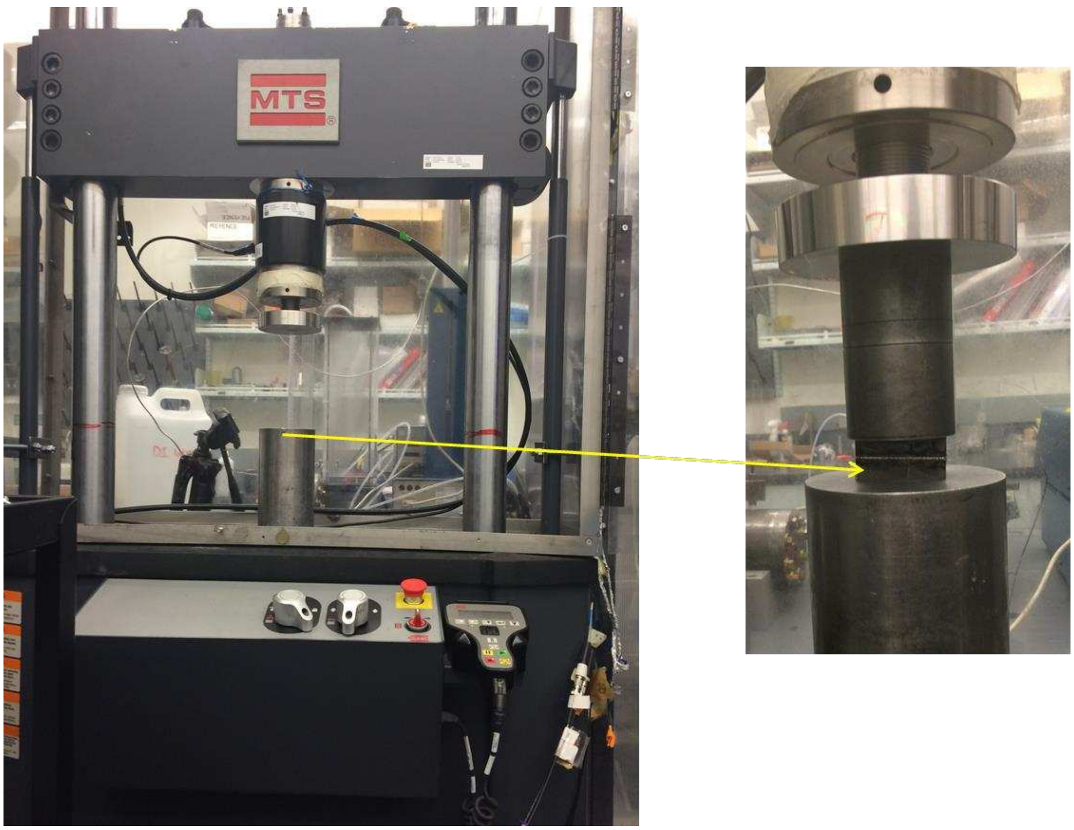

Figure 3.13: Fractured sample filled with proppant placed in MTS load apparatus for uniaxial testing to measure fracture aperture.

3.7 Fracture Conductivity Experiment using the Triaxial Cell

Two experiments were performed to test for propped short and long term fracture conductivity in the Vaca Muerta formation under triaxial stress state. Simultaneously, acoustic transit times were recorded for evaluation of the sample and the fracture mechanical properties at increasing stress conditions. The experimental apparatus used in the study was originally designed and built by Dr. Ali I. Mese and donated to UNGI Geomechanics laboratory by Dr. Mese in 2013. Padin (2015) has used the cell to study the osmosis in organic-rich shale samples. A few minor modifications have been made to the apparatus to accommodate for the high conductivity of the propped fracture. The advantage of the triaxial cell setting over the standard API procedures to measure fracture conductivity, is that more realistic bottomhole conditions are being simulated as the sample tested is exposed simultaneously to axial stress (simulating overburden pressure on the fracture) and confining stress (simulating isotropic horizontal or closure stress on the fracture). Alternatively, in standard API testing and most past reviewed studies, uniaxial stress is applied, neglecting the effect of the multiple principle stresses that exist in the reservoir formation.

3.7.1 Apparatus and Testing Conditions

The apparatus designed to attain the experimental objectives of the study is composed of a system that has the capability to measure several parameters such as the steady and unsteady permeability, rock strength and compressional and shear wave velocities. The system is capable of recording simultaneous measurements of the stress, strain, acoustic P and S wave velocities and flow data. The system consists of several components necessary for all these measurements to be taken. These components are: a triaxial load cell (1), a pore fluid injection system (2), a back pressure system (3), an axial and confining pressure system (4), a vacuum system (5) and a temperature control system (6). These components are shown in Figure 3.14. A schematic of how all the components are connected is shown in Figure 3.15. The components are described in more detail in the following paragraphs.

3.7.1.1 The Sample Core Holder

The main component of the system is the triaxial load cell, which is a high pressure vessel that holds core samples of 1.5 inch diameter. Holes are present in the cell to allow for hydraulic lines cables to pass through for pressure supply and acoustic wave measurements respectively. In the design by Padin (2015), the bottom section of the cell, where the confining fluid is contained, contains the lower end cap which contains two hydraulic lines that allow for pore fluid circulation through a porous filter. In the upper section where the axial fluid is contained, a porous filter is also placed on the top cap and is followed by a hydraulic line that is connected to a pressure transducer. Non-conductive mineral oil, which is sourced through non-conductive hoses, was chosen as the axial and confining fluids so they do not to interfere with resistivity measurements performed in measurements performed in the prior experimental studies when the cell was used.

Separation of axial and confining fluids is achieved by means of a triple O-ring matching the inner diameter of the cell.

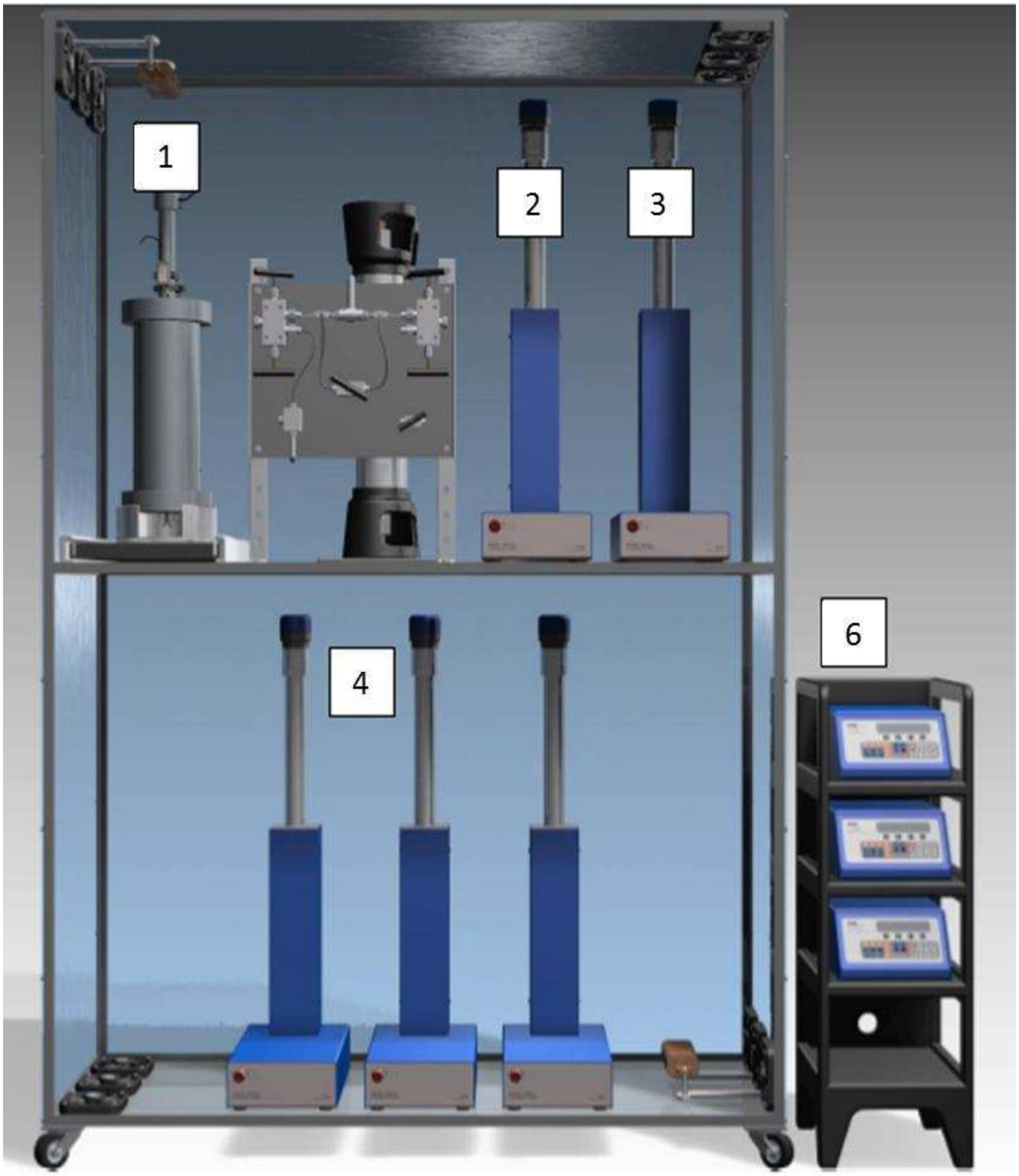

Figure 3.14: 3D view of components of the experimental setup. The numbering corresponds to the various components of the system, described in the text (Padin 2015).

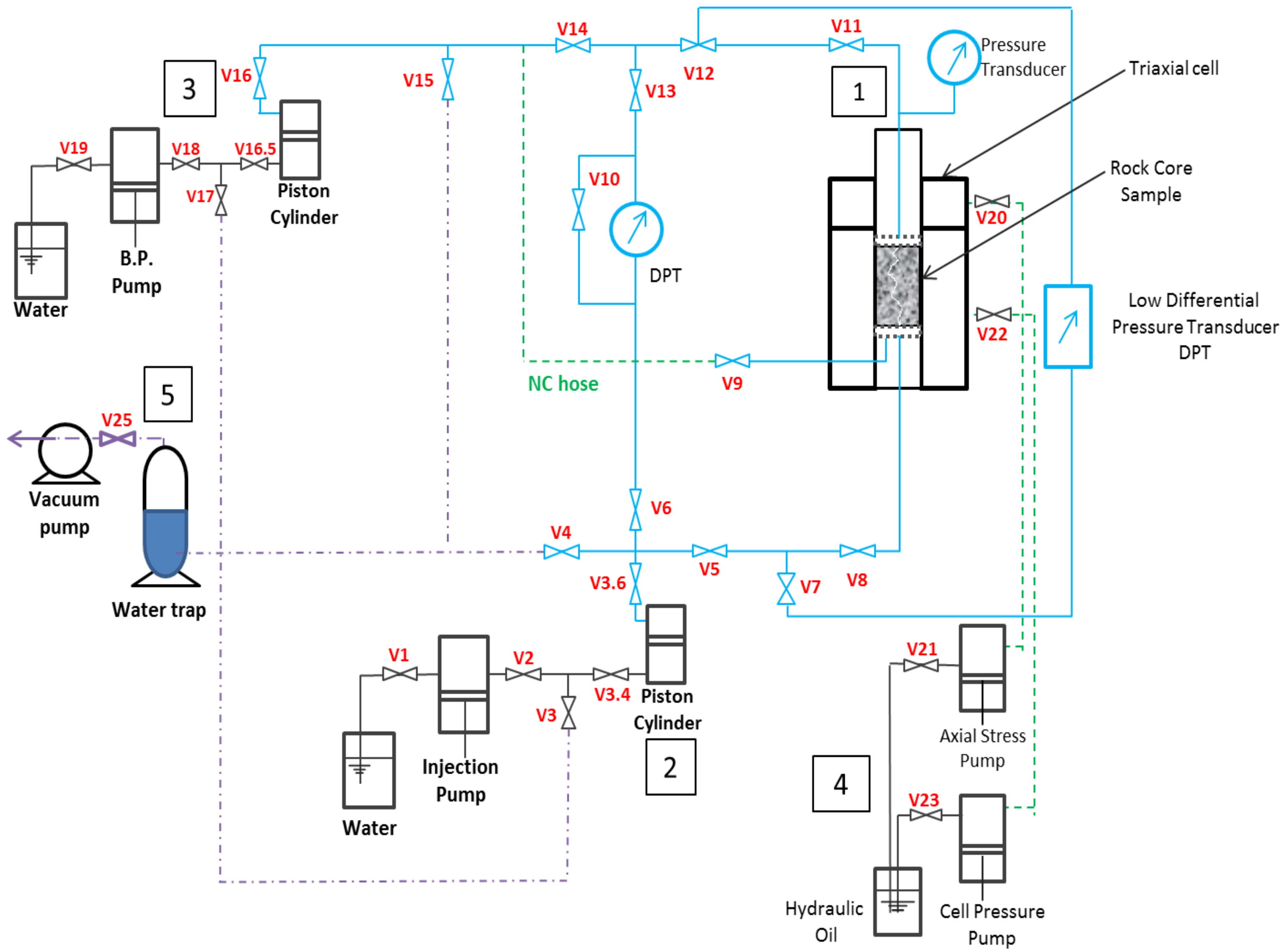

Figure 3.15: Schematic of the testing apparatus. The lines in blue are made of stainless steel; in green: lines made out of nonconductive material; in purple: lines leading to the vacuum pump.

The upper cap including the triple O-ring and the core holder that connects the upper cap and the lower cap are shown in Figure 3.16. Pore fluids like brine, that are circulated to maintain pore pressure and during permeability testing, along with the sample are separated from axial and confining fluids using a flexible rubber sleeve (Neoprene) that is capable of transmitting pressure to the sample. The pore fluid lines are enclosed within piston cylinders, for extra isolation from the mineral oil. A basic schematic of the triaxial cell is shown in Figure 3.17. A Solidworks® design that describes the cell configuration in more detail is presented in Figure 3.18.

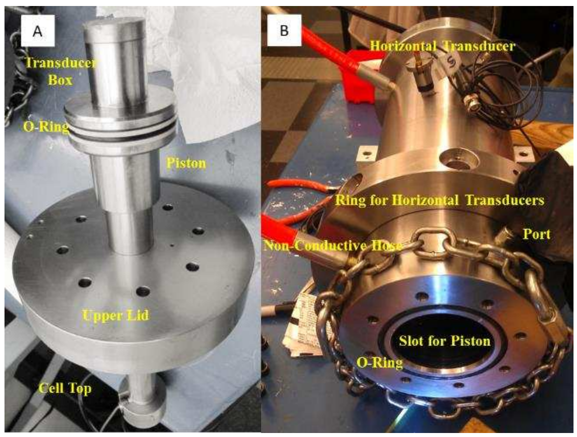

Figure 3.16: (A) Internal top piston; (B) cell sample holder (Padin 2015).

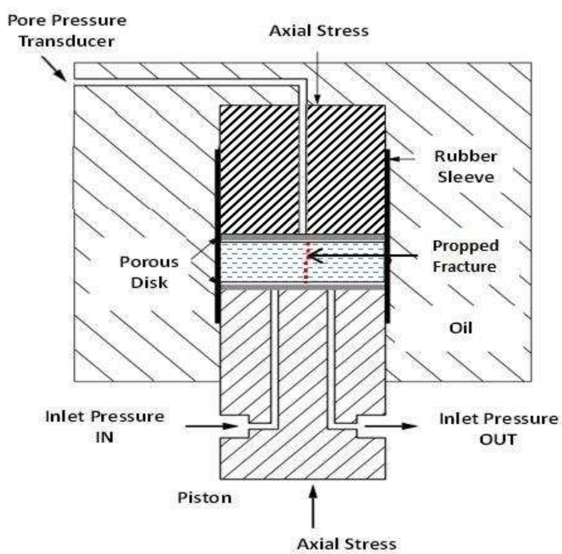

Figure 3.17: Schematic of the triaxial cell inner configuration (Padin 2015).

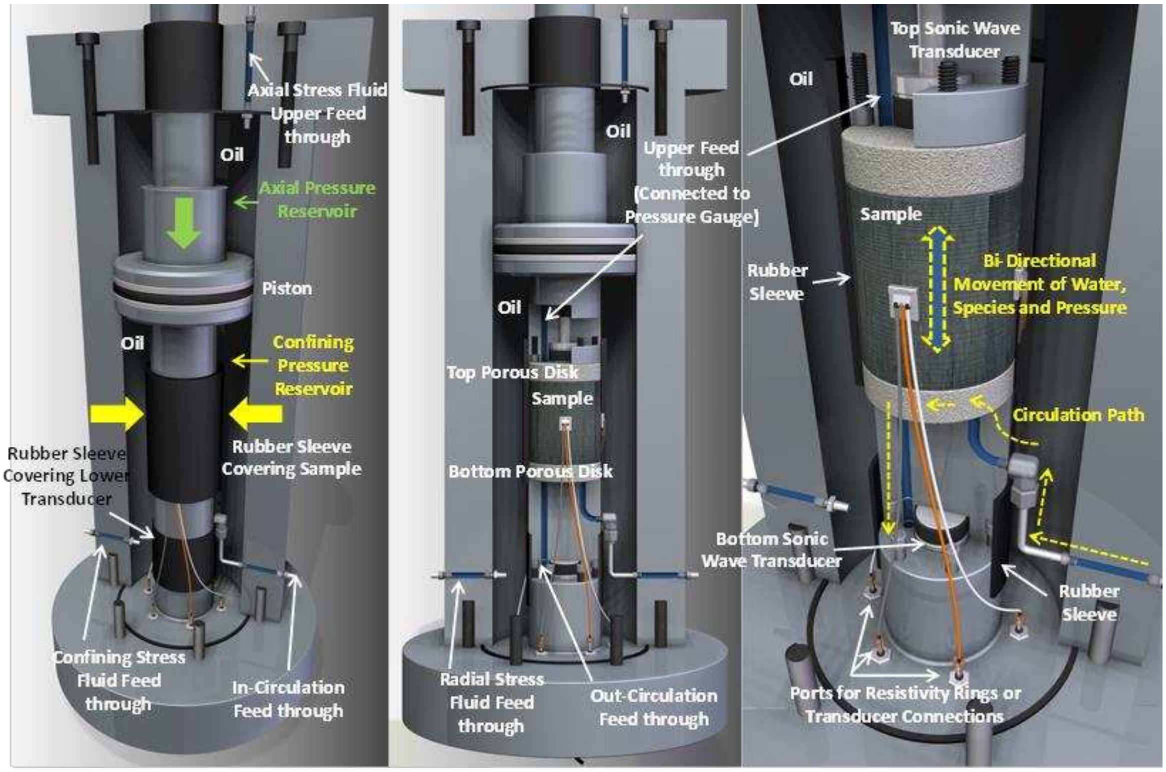

Figure 3.18: Cross Section of the cell where is the sample is contained, designed using Solidworks® (Padin 2015).

Porous filters similar to the ones referred to by Padin (2015), were used in the first experiment performed (Figure 3.19). Pores in those filters were of 10 microns diameter. To make sure that obtained permeability data is reliable, a calibration permeability test was performed to compare the permeability values with and without the fractured samples. It was discovered that the actual fractured sample permeability is masked by the presence of porous filters. This occurred due to the fact that the holes in the pistons are located at the edge of piston end surface while the fracture is located in the center of sample. Therefore, in both the inlet and outlet pore filters, the pore fluid has to flow through the filters in radial direction in the sections between the pore fluid inlet and fracture inlet and between the fracture outlet and pore fluid outlet, creating unnecessary pore pressure built up. The results of the first experiment were not completely discarded as trends of different relationships of different properties were used to arrive with conclusions for this research study. The porous filters were replaced by a new setup in the second test to accommodate for fracture conductivity experiments. Two disks were cut from a stainless steel rod (1.5 inch diameter) using a metal lathe and grooved in the center nearly across their whole diameter then drilled to create holes matching the pore pressure holes in the upper and lower pistons using a manual end mill. The grooves were made so that they are placed exactly under the fracture, solving the problem encountered using the filter used in the previous test. To prevent the proppant from escaping to the flow lines, manual made filters, that were made by punching holes into an aluminum thin material using a sewing needle were glued to the grooves. The metal disks were then glued to the end of the upper and lower pistons, replacing the porous disks, while aligning the flow line holes. The setup of the new porous filter is described in Figure 3.20. Pressure differential across the new filters was tested to make sure that it was negligible, and therefore not having an effect on the measured permeability of the fractures.

Figure 3.19: Porous disks used in the first test.

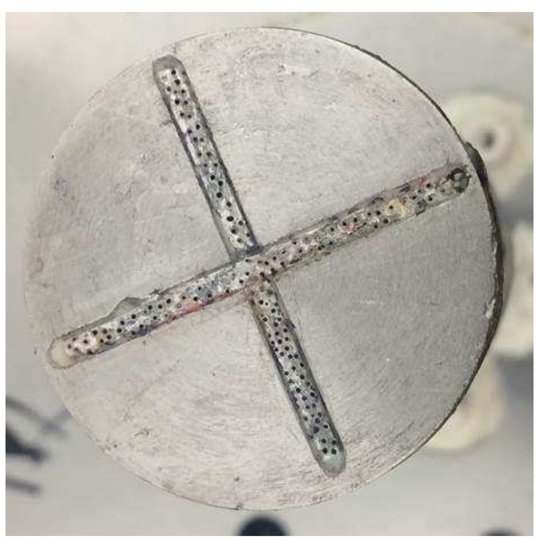

Figure 3.20: New porous filter to accommodate for low pressure drop though fractured core samples.

3.7.1.2 The Pore Pressure System

The pore pressure is controlled through the injection and back pressure systems, which are number 1 and 2 as indicated in Figure 3.15. The injection pressure system (1), injects pore fluid in the bottom part of the sample through valve V8. The fluid circulates through the manually made porous filters and is received through V11 followed by V16 into the back pressure (B.P.) system (3). Both injection and back pressure systems are 10,000 psi, ISCO pumps that generate fluid (pore) pressure. Pump pressure changes are manually controlled during permeability testing to avoid over pressuring the cell and displacing the proppant, which might affect experimental results. Each pump is connected to a piston cylinder which contains 2% KCl solution at the side connected to the cell. Pressure is applied from the pumps using deionized water and the pistons transfer that pressure to the sample. The pistons help separate the KCl water from the pump hydraulic fluid, which is deionized water in this case. Pore pressure is maintained at 100 psi during most of the experiment period. This is accomplished by making sure that the average pressure between the injection and back pressure pumps is always maintained at that value.

3.7.1.3 Axial and Confining Stress System

The hydraulic system (4) controls the axial and confining pressures through the application of mineral oil. In this case, separation is not required as the oil is already separated from the sample and pore pressure lines by means of a rubber sleeve and metallic piston cylinders as explained earlier. The axial pressure pushes the piston downwards and the confining pressure is in form of radial pressure around the sample as illustrated in Figure 3.18. Initially, it was intended to apply anisotropic stress to the sample to better simulate field conditions. Several trials were performed with metal core plugs to look at the stability of triaxial cell under different stress conditions with different confining stress to axial stress ratios. During the first 6 trials it was found that the resulting pressures were unstable, which caused the piston to move up uncontrollably with the rubber jacket, creating a pathway for the oil in the bottom section of the cell to move into the pore pressure lines and to contaminate the sample. Stability in the cell was finally reached by applying a ratio of 2:1 of confining stress to axial stress. When this stress condition was tested in uniaxial stress conditions using the MTS loading frame the sample reached its uniaxial compressive strength (UCS) and failed (Figure 3.21). If the sample fails during the triaxial test, the number of pathways through the sample will increase, increasing its measuring permeability.

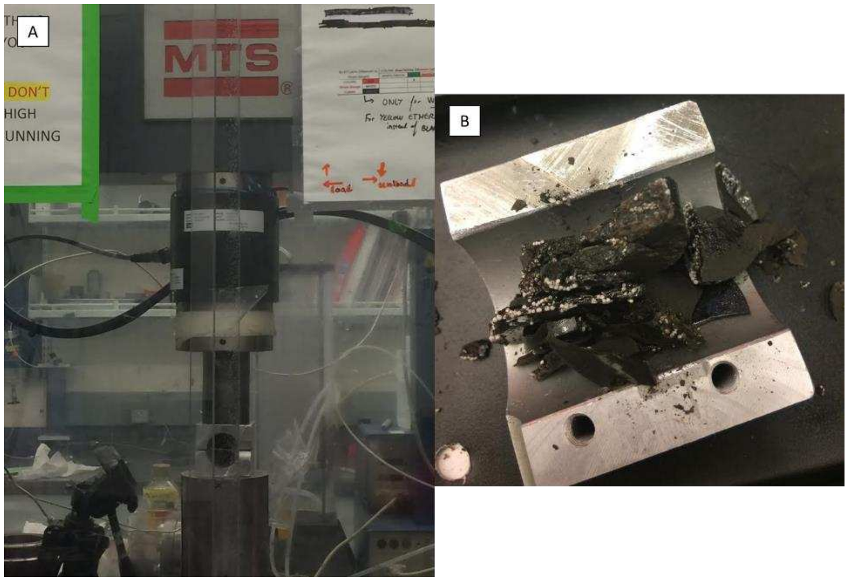

Figure 3.21: (A) Picture of the sample placed in a core holder in the MTS load system, for uniaxial stress testing; (B) Sample failed as it reached its UCS; notice the embedment of proppant in the sample.

To prevent that risk from happening during the test, it was decided to apply isotropic stress (axial stress=confining stress) during testing. To achieve isotropic test conditions, the axial pressure exceeds the confining pressure in the cell as shown in Equation (3.5). The axial force required to apply the axial stress is presented by F_a; p_a is the pump axial pressure; p_c is the pump confining pressure, which is equal to the confining stress applied to the sample σ_c; A_c is the surface area of the larger section of the piston; and σ_a is the axial stress applied to the sample with a cross sectional area of with A_s, explained in Figure 3.22.

$$F_a = p_a (A_c - A_s) - p_c (A_c - A_s) \tag{3.5}$$

where:

$$\sigma_a = \frac{F_a}{A_s} \tag{3.6}$$

By rearranging the equations, by substituting above to arrive with Equation 3.5 into Equation 3.6, we can see that the axial stress is dependent on the relation between the areas of the sample and the piston in Equation 3.7:

$$\sigma_a = p_a \left(\frac{A_c}{A_s} - 1 \right) - p_c \left(\frac{A_c}{A_s} - 1 \right) \tag{3.7}$$

With further rearranging:

$$p_a = \frac{\sigma_a}{\left(\frac{A_c}{A_s} - 1\right)} - p_c \tag{3.8}$$

Therefore, in case of isotropic stress, for each value of σ_c, to obtain an equal value of σ_a, Equation 3.8 is used to get the required axial pump pressure.

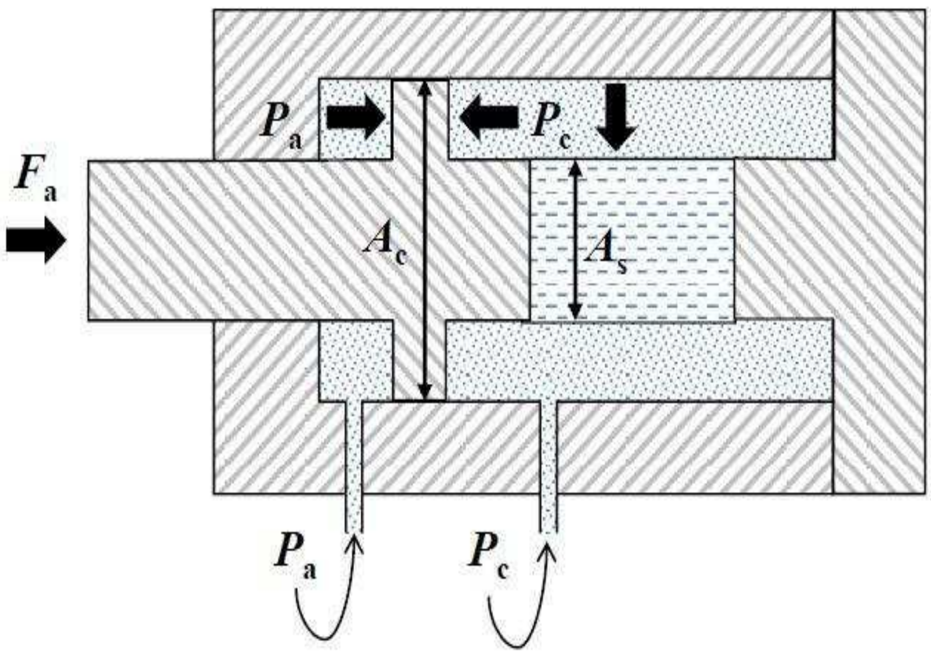

Figure 3.22: Representation of the forces applied to the core holder to create axial and confining stresses. F_A is the axial force necessary to apply the in situ axial stress; p_a is the pump axial pressure; p_c is the pump confining pressure; A_C is the surface area of the widest section of the piston; and A_S is the cross section area of the sample (Padin 2015).

The effective stress is calculated as shown in Equation 3.9 by subtracting the Biot's coefficient α multiplied by the pore pressure p_p from the axial stress σ_a, as explained previously the literature review section. The axial and confining stresses used in the experiments and the required pump pressures are shown in a table in Appendix B, along with the corresponding pore pressures and effective stresses.

$$\sigma_a' = \sigma_a - \alpha p_p \tag{3.9}$$

3.7.1.4 Temperature Control

An insulation chamber is important to maintain constant temperature while testing, even though the laboratory is under thermostat controlled temperature. When the system was being set up in its initial stages by Padin (2005), it was found that even small temperature changes resulted in great variations in line pressures. The pore pressure changes were significant to an extent that they masked aimed measurements. Therefore, the constant temperature chamber was created, by surrounding the test setup including the cell and the pumps with insulating walls that are made of twin wall polycarbonate sheets (Figure 3.14 (6)), while hot air is being circulated continuously. Temperature is maintained at 40 C° with error that amounts only to ±0.3 C°, measured by two temperature gauges that are connected to heater and fan controllers.

3.7.1.5 Vacuum System

The pore pressure lines that are in contact with the sample and the piston cylinders are connected to a vacuum that feeds into a reservoir as shown in Figure 3.15. The presence of a vacuum pump connected to the system is important to eliminate air from the system, as air is compressible and might lead to pressure changes in the lines by dissolving in water, which might interfere with permeability measurements. The vacuum pump is used to degas the 2% KCl water that flows through the sample. The degassed fluid is then vacuumed for 30 minutes when it is placed in the injection piston cylinder, prior to entering the high pressure hydraulic line system.

3.7.2 Data Acquisition and Storage

Data collection and storage is important, especially for long term experiments such as the long term permeability experiments performed. Data acquisition is also important for surveillance, in case an undesired incident occurs, such as leakage. Measurements vary by the second and manual data collection would be highly inaccurate. The Data Acquisition System (DAQ) is used to collect data from the different components of the experimental set up and store it into a computer. The system consists of three ISCO syringe pump controllers, the LVDT that measures axial deformation changes, a pressure transducer, and two differential pressure transducers. All data acquisition systems are connected to the desktop computer via RS232 cables. The LVDT which measures the axial deformation and the pressure transducers transmit voltage signals through an A/D DAQ board that is connected to the computer. The software required for data acquisition displays and stores the data into excel sheets and is based on Labview®. The pore pressure system is explained in detail as an important modification has been made to accommodate for fracture permeability measurements. In addition, wave velocity data acquisition is also explained as it is an important step throughout early to late stages of the study.

3.7.2.1 Pore Pressure Measurement System

The injection and back pressure pump pressure are recorded through the DAQ system in real time. Three other pore pressure measurements are also recorded; pore pressure at the top (downstream) of the sample and two differential pressures between circulation pressure and downstream pressure. Measurement at the top of the sample is obtained by means of a high precision bidirectional Omegadyne® pressure transducer (Figure 3.23) with accuracy: ±0.25%.

Figure 3.23: Omegadyne® pressure transducer for downstream pressure measurement.

For measurement of the differential pressure, a Stellar Technology® transducer has been used in prior measurements. The pressure difference between the inlet and outlet of sample is very low (~30 psi) even at the highest flow rate of syringe pumps, due to the fact that it is fractured. The Stellar Technology® transducer pressure transducer was found to be not adequate to measure such low pore pressure difference. This is due to its high pressure capacities and associated inherent errors which could potentially be comparable or greater than the actual pressure difference to be measured. Therefore, a new low wet pressure transducer has been added to the apparatus to remedy the problem. The Veris PWLX05S Wet Pressure Differential Transducer has very low differential pressure ranges (0-250 psig) (Figure 3.24).

Figure 3.24: Veris PWLX05S Wet Pressure Differential Transducer

Pressure change measured by the transducer is transmitted to the DAQ system and recorded as voltage. Therefore, it was necessary to perform calibration procedures to convert the voltage signal to pressure. This was performed by connecting the transducer to a degassed water reservoir at known different heights. A relationship was made between the output voltage signal and the corresponding pressure calculated from the head of the reservoir source (ρgh) and is shown in Figure 3.25.

3.7.2.2 Ultrasonic Wave Velocity Measurement System

Piezoelectric transducers of 1 MHz- central frequency was used in the wave velocity measurements. Compressional and shear pulses are generated by applying a high voltage, short duration (ultrasonic frequency) electrical pulse to the transmitting piezoelectric transducer using the same pulse generator. The electrical pulse is transmitted through the fractured core sample in form of an elastic wave to the receiving transducer in the other end of the sample. P-wave and S-wave velocities are calculated based on the time for the wave to travel through the sample. The overall communication system between the sample and computer is shown in Figure 3.26.

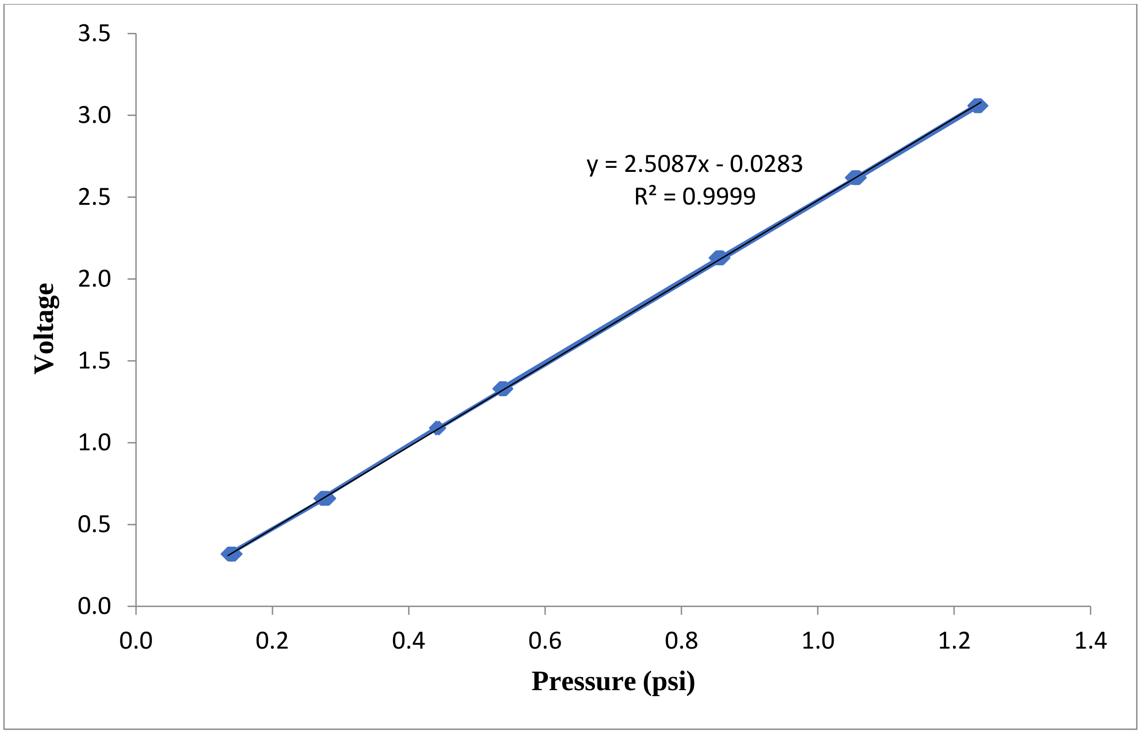

Figure 3.25: Relationship between acquired voltage through DAQ and corresponding pressures.

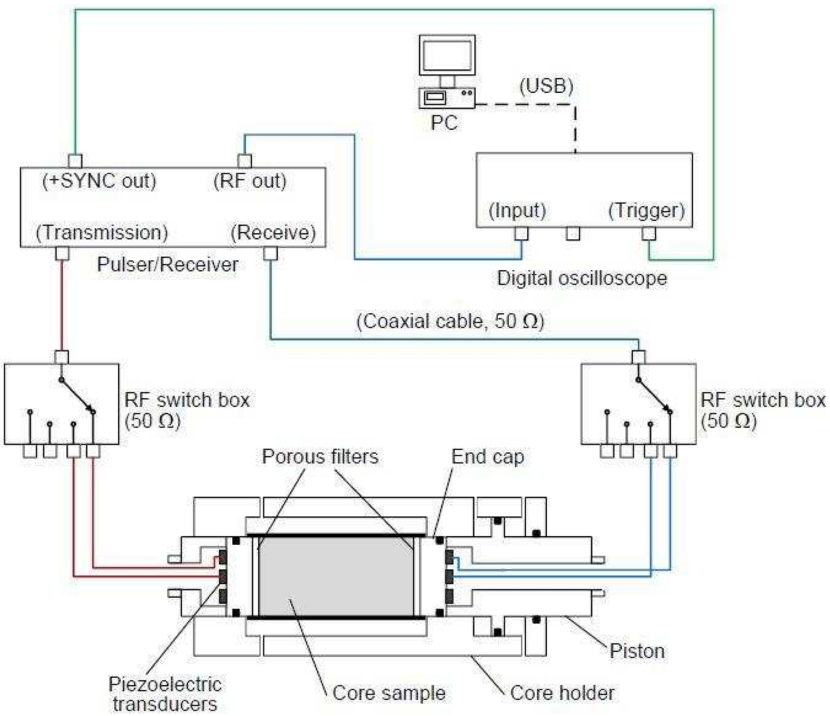

Figure 3.26: Ultrasonic wave velocity system (Padin 2015).

The wave form data viewed on the oscilloscope is viewed and stored using a software package was developed using LabVIEW® (Figure 3.27), which also used to set parameters such as the x and y axis intervals (voltage), trigger point and logging settings for the waves.

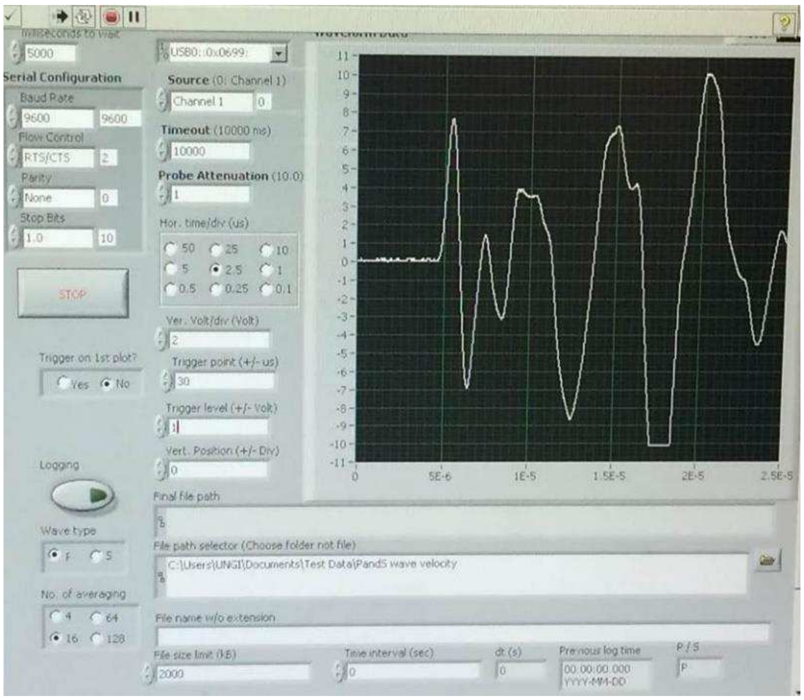

Figure 3.27: Interface of software package from LabVIEW.

For this experiment, P and S wave forms were recorded at each stress condition, to compare the acoustic wave velocities with increasing stress. Wave velocities were also measured at the time of each permeability test, at confining stresses where long term permeability terms were performed to be able to correlate them to permeability values.

Calibration was performed to measure the compressional and shear wave arrival times without the sample. Calibration was performed at the same stress states used in the experiments. We conducted calibration both using the old porous filters and using the manually made filters.

3.7.3 Experimental Procedure

The experimental procedures involves many steps required to assemble the cell to collecting the data. The procedure is discussed in detail in Appendix A.

CHAPTER 4

EXPERIMENTAL RESULTS AND DISCUSSION

This section presents results for each step of the experimental analysis starting from sample analysis to stress dependent propped fracture conductivity. Analysis is performed by examining relationship between various parameters including the stress dependence of compressional and shear wave velocities and fracture permeability as well as the correlation between the shear velocity and fracture permeability. The discussion in this section focuses on the degradation of sample mechanical properties with exposure to fluid, difference in the results between the 2 propped fracture conductivity experiments, relationship between fracture stiffness and S-wave velocity and long term fracture permeability.

4.1 Sample Properties

Core sample properties aided in explaining results obtained from the experiments conducted in this research study and were also used as a baseline for comparing the fracture face image before and after the experiments were performed.

4.1.1 Sample Mineralogy

Mineralogical composition analysis for samples used in this study has been conducted at the Mineral Labs and is presented in Table 4.1. The sample is quartz rich, with 33 wt% quartz, 20% calcite and 29% clay content. The analysis performed at Terratek for the LJE. 1010 entire cored interval also presents high clay composition. Alramahi and Sundberg (2012) reported that samples tested for conductivity with high clay composition experienced higher embedment compared to samples with low clay content. Moreover, Moreover, the clay could react with the saturating fluid and swell, resulting in swelling and more embedment through the softening of the fracture face.

4.1.2 Sample Fracture Intensity

The following CT scan images show a cross section from the top, at the mid depth of the core plugs used in the study (Figure 4.1). Samples VM-01 and VM-02 that were used for the first and

Table 4.1: Mineralogical composition of the core plug from the LJE. 1010 well studied (depth 3094.1 m).

Mineral Name	Approx. Wt %
Quartz	33
Mica/Illite	24
Plagioclase feldspar	8
K-feldspar	<3
Kaolinite	5
Calcite	20
Pyrite	3
Hematite	<3
"Unidentified"	<5

second propped fracture conductivity experiments, respectively contain a fracture that occupies the whole diameter of the core. The fracture is most probably induced from the coring process and is continuous in VM-02 through the outer edge of the core sample, unlike in VM-01 where the fracture discontinues in the center. Calcite filled micro-fractures are observed in the samples. The induced fractures made it easier to induce the fracture in the cores for the conductivity experiments.

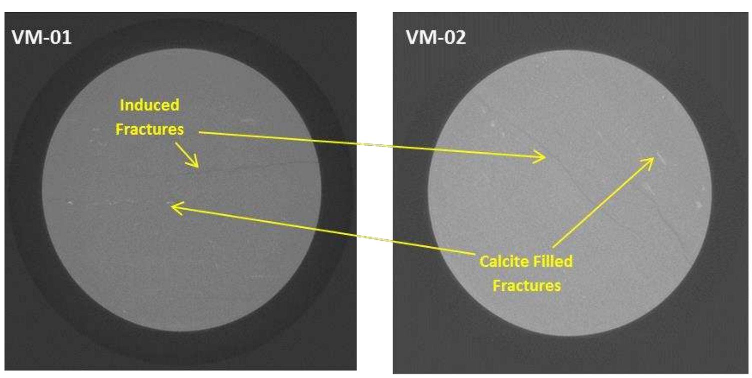

Figure 4.1: CT scan images showing the fracture intensity in the studied cores (VM-01 and VM-02).

4.1.3 Fracture Face Topography

The fracture face topography was investigated in micro scale to utilize as a basis of comparison when comparing the undamaged fracture face prior to the proppant conductivity experiment with the damaged fracture face after the experiment. The fracture face is relatively flat with few roughness indications (peaks and troughs) as shown in Figure 4.2.

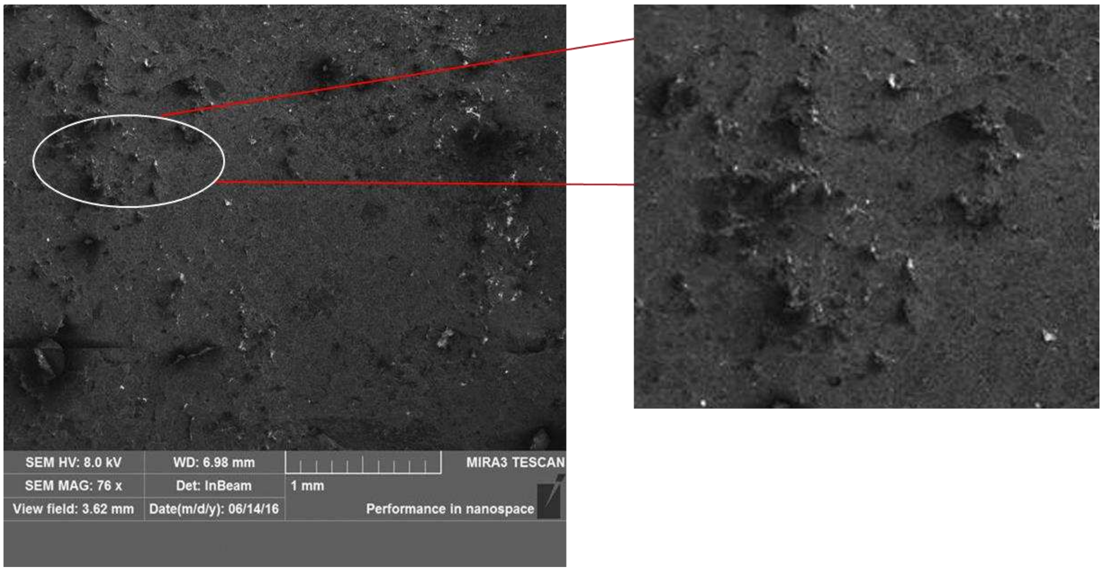

Figure 4.2: Figure 4.2: Scanning Electron Microscope (FSEM) image of the fracture face before the conductivity tests was conducted on the sample under triaxial stress state.

4.2 Effect of Fluid Interactions on Formation Mechanical Properties

The change in mechanical properties that occurs due to interaction with the fracturing fluid (2% KCl brine in this study) is a factor of various formation properties. The mineralogical composition determines the chemical reactions that take place between the rock, native fluid and fracturing fluid. Compressional and shear wave velocities play an important role in the evaluation of Young's modulus and Poisson's ratio. The wave speeds passing through a fractured medium filled with different fluid compositions and proppants vary. There is slight uncertainty in the first arrival times for particularly shear wave velocities. Yet, the uncertainty is reduced when comparing the arrival times with those picked for the fractured sample.

4.2.1 Wave Velocity Response to Fluid Saturation

The changes in the calculated P-wave velocities before and after the sample is exposed to 2% KCl are presented in Figure 4.3. The P-wave velocity increases as a result of saturation of the core sample with the fracturing fluid. The velocity increased from an average calculated value of 4.083 km/s to 4.97 km/s in sample VM-01 and from 4.2 km/s to 4.9 km/s in sample VM-02. The presence of fluid in the sample pore space resulted in an increase in the bulk density of the core sample promoting faster P-wave propagation. In addition, the fluid itself acts as a medium for wave transmission (Nur and Simmons 1969).

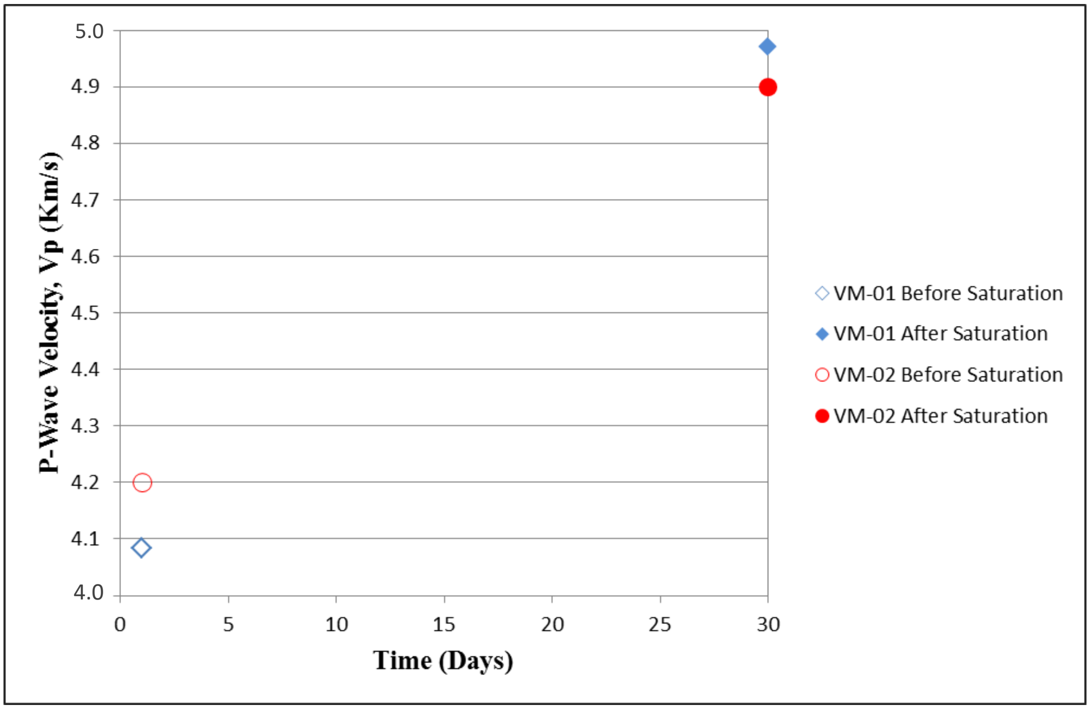

Figure 4.3: P-wave velocity variation before and after saturation in 2% KCl for 30 days.

Conversely, calculated S-wave velocities decreased after saturation as shown in Figure 4.4. Shear waves do not travel in the fluid phase which results in a slowdown in their velocity (Nur and Simmons 1969). Wave velocities decreased from 2.4 km/s to 2.2 km/s in sample VM-01 and 2.8 km/s to 2.5 km/s in sample VM-02.

Compressional and shear wave velocities calculated before and after saturation differ between the 2 samples, although they are from the same depth in well LJE. 1010. This may be explained by the high degree of the fracture anisotropy present in the sample which contribute to the difference in wave velocities. The fractures also serve as a pathway for fluid to move into the sample. Therefore, different fracture intensities could result in different wt% saturations between samples resulting in densities.

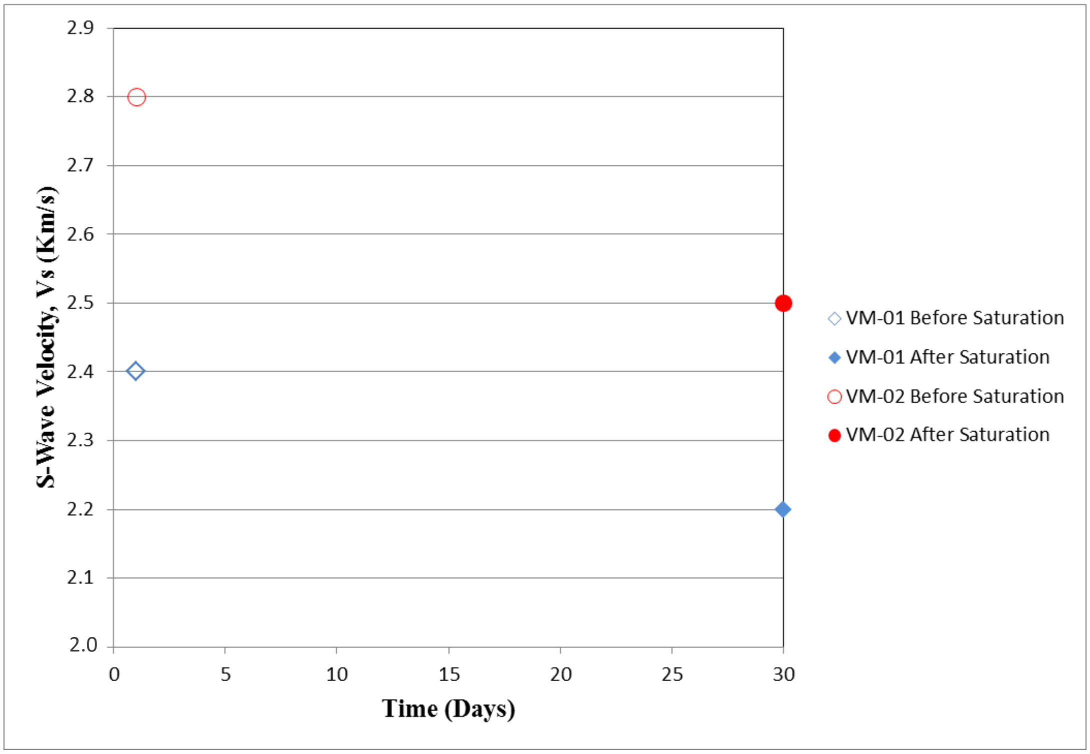

Figure 4.4: P-wave velocity variation before and after saturation in 2% KCl for 30 days.

4.2.2 The Effect of Saturation on Sample Mechanical Properties

The saturation of the sample in 2% KCl water resulted in the reduction of its Young's modulus. The variation of the Young's moduli before and after saturation is presented in Figure 4.5.

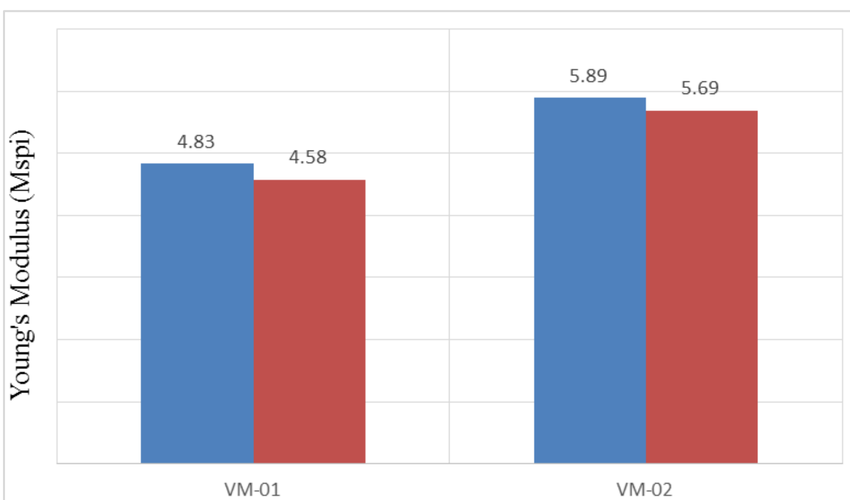

Figure 4.5: Decrease in Young's modulus as a result of saturation of the sample with fracturing fluid (2% KCl) for 30 days. The blue bars represent the Young's Modulus before sample saturation and the red bars show the Young's Modulus after sample saturation.

It must be noted that the decrease in the Young's moduli wasn't significant, amounting to 5.2% and 3.4% for samples VM-01 and VM-02, respectively. The samples, however contain water sensitive clays mica/illite, which can lead to the expectancy that Young's modulus decreases significantly with fluid interaction. However, the KCl present in the solution is believed to have contributed to the sample maintaining its stiffness through preventing the swelling expected to occur as a result of interacting with the fracturing fluid. Similar results were reported by Akrad et al. (2011) for samples with similar mineralogy to the Vaca Muerta samples used in this study that were saturated in 2% KCl for 30 days. Reduction in Young's modulus was insignificant (10%) in samples from the Barnett shale formation which are quartz rich with high clay content (20 wt%) like the samples used in our study. The Middle Bakken shale samples used by Akrad at al. (2011) that were calcite rich with low clay content exhibited higher percentage of Young's modulus reduction of 40% . These results lead Akrad et al. (2011) to the conclusion that the use of KCl as additive in fracturing fluids does not help in preventing Young's Modulus loss in formations with low clay content or calcite rich formation, unlike in quartz and clay rich formation in which it has proven to be beneficial in maintaining rock stiffness. A comparison of the percentage reduction in the Young's Moduli in the Vaca Muerta (our study), Barnett and Middle Bakken (Akrad et al. 2011) shale samples after saturation in 2% KCl water is presented in Figure 4.6.

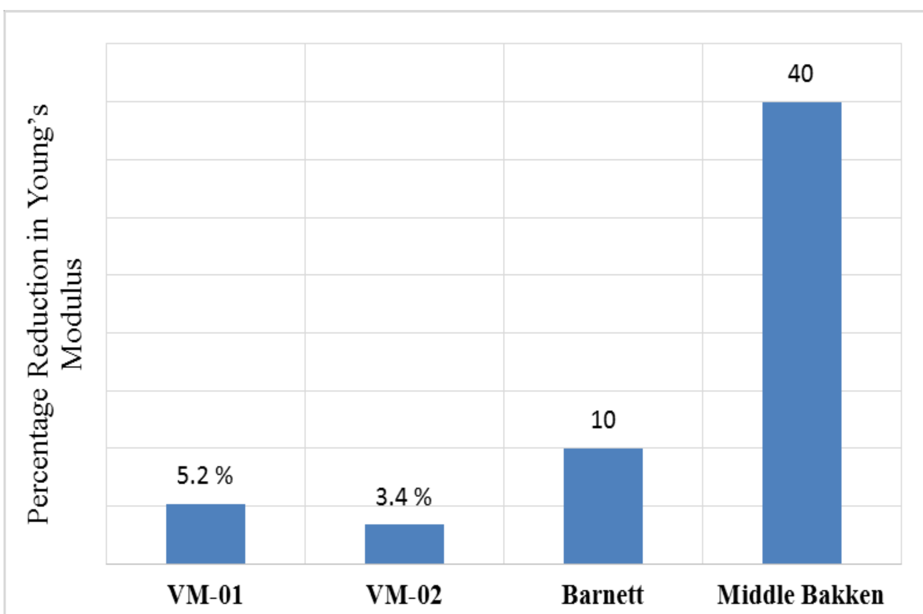

Figure 4.6: Percentage reduction in Young's modulus in the Vaca Muerta, Barnett and Middle Bakken shale samples as a result of saturation in 2% KCl water for 30 days.

4.3 Propped Fracture Conductivity Tests

Two tests were performed to test for propped fracture conductivity in fractured samples coated with a mono-layer of 20 mesh ceramic proppant. As mentioned in Chapter 3, fracture conductivity values obtained from the first experiment performed are a great underestimate of actual lab proppant conductivity values obtained in the lab, due to the presence of a less permeable porous filters overlying and underlying the sample during the experiment. However, trends of the results obtained from this experiment are used to arrive with parts of the conclusion from this research study. The adjustments made to the apparatus for Experiment 2 were based on lessons learned in Experiment 1. Both samples exhibit similar relations between compressional and shear wave velocities and change in fracture conductivity.

4.3.1 Damage Mechanisms Observed

Damage is inevitable when the samples are placed at high in-situ stress conditions. Damage was observed in the samples when they were investigated after the completion of the experiments. In sample VM- 01, proppant embedment was not prevalent over the fracture face area. However, proppant fines migration and spalling were visibly significant as the porous filters were inspected (Figure 4.7). When the samples were taken out of the sample cell assembly, it was found out that the fractures were not fully filled with proppants. In sample VM-02, proppant embedment and spalling were clearly visible as shown in Figure 4.8.The high clay content present in the sample correlates to the high embedment observed in the sample as reported by Alramahi and Sundberg (2012).

4.3.2 Propped Fracture Conductivity-Experiment 1

This section details the propped fracture conductivity and acoustic wave velocities results from the first an experiment conducted in the triaxial cell. The conductivity results were found to be somehow inaccurate. However, trends between change in propped fracture conductivity and acoustic wave velocities were used as lessons learned for the experimental design and fracture permeability calculations for the second experiment.

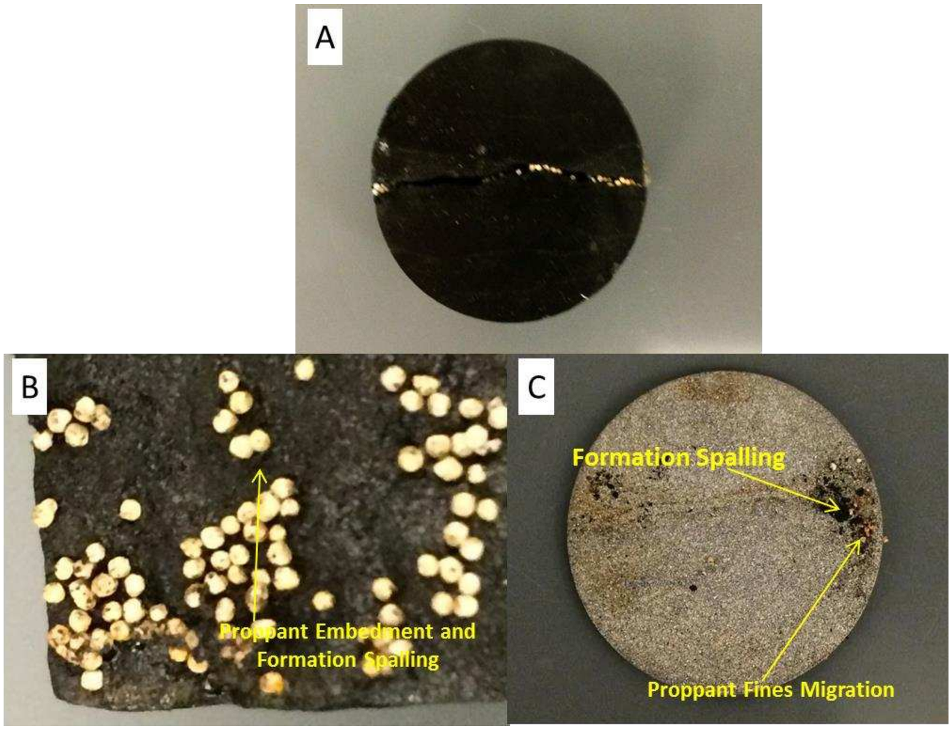

Figure 4.7: Evidence of damage in Vaca Muerta core sample VM-01 after experiment 1. (A) shows that proppant escaped from the fracture to the porous filters; (B) Evidence of proppant embedment and formation spalling; (C) Proppant and formation fines that broke off the fracture face.

Figure 4.8: Proppant embedment in Vaca Muerta core sample VM-02 after the triaxial stress conductivity experiment (Experiment 2).

4.3.2.1 Stress Dependent Propped Fracture Conductivity

Short term fracture conductivity was recorded for experiment 1. Since the value of the fracture width w_f with stress change is not recorded during the experiment, conductivity was calculated and presented as a function of effective stress in Figure 4.9. Using Darcy's law, the area term A is replaced by the fracture width multiplied by the fracture height $w_f h$ as shown in Equation 4.1. The fracture conductivity is defined as the fracture permeability (k_f) multiplied by the fracture aperture. Hence, it could be calculated by multiplying both sides of Equation 4.1 by w_f to arrive with Equation 4.2.

$$k_f = \frac{q\mu l}{w_f h \Delta p} \tag{4.1}$$

$$k_f w_f = \frac{q\mu l}{h \Delta p} \tag{4.2}$$

The conductivity variation with increasing closure stress is shown in Figure 4.9. Steep decline in conductivity is observed at lower stresses (400-3000 psi), followed by small decline at higher stresses. This trend was observed most likely due to the fact that the fracture closed significantly at the lower applied stresses and then the two fracture faces approached closer together at higher stress causing higher resistance to closure which in turn leads to a lower rate of decrease of permeability. The values obtained for fracture conductivity are unreliable since it was determined after the test that the permeability of the porous filters overlying and underlying the sample is less than that of the fracture permeability. The true values recorded by the differential transducer are masked by the pressure gradient created as the fluid transports through the porous filters as explained in more detail in Chapter 3. A new setup was created for the second experiment, which is explained in further detail in following sections.

4.3.2.2 Effect of Stress on Wave Velocity Propagation

Although the fracture permeability values from experiment are not highly accurate, it is worth noting that the trends observed for changes in wave velocity with respect to change in propped fracture conductivity provide valuable information on the stress dependent changes in both parameters. The compressional wave velocities as a function of effective stress for VM-01 is shown in Figure 4.10.

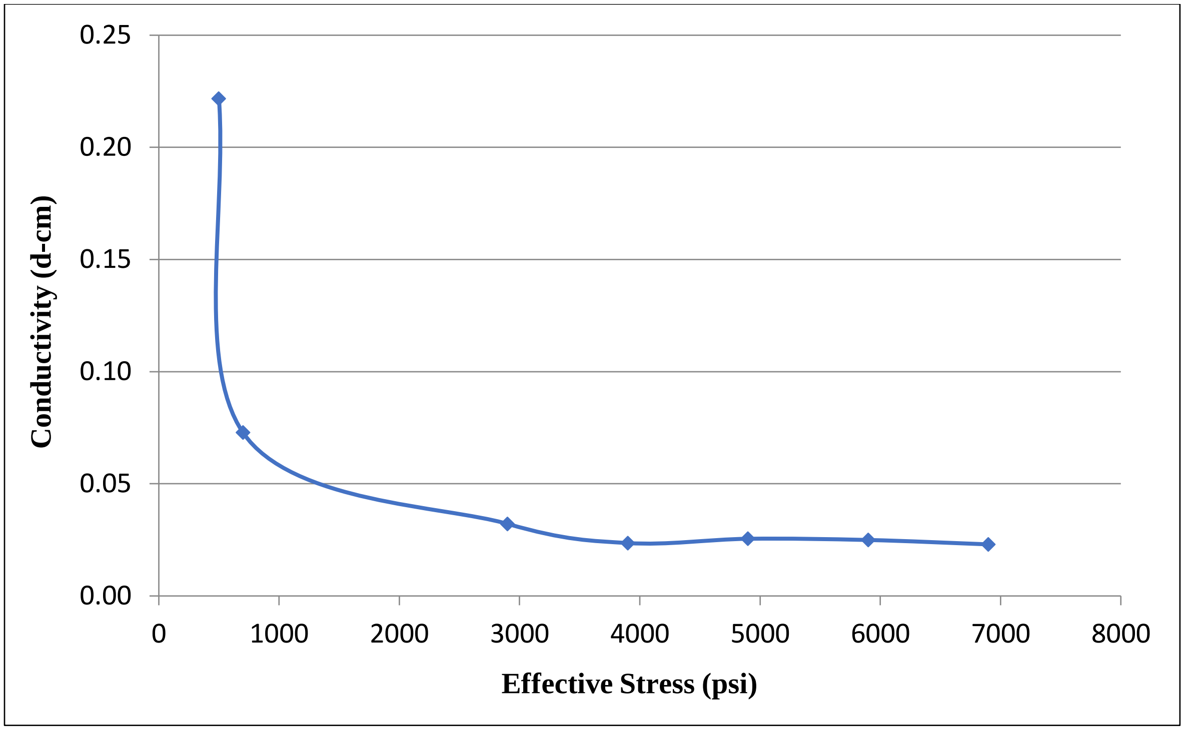

Figure 4.9: Propped fracture conductivity vs. Effective confining stress.

P-wave velocity increased slowly with increasing stress. It would be argued that P-wave velocity should remain constant as it should preferentially propagate through the dense intact section of the sample. The velocity is expected to remain the same as the sample did not deform axially based on caliper measurements after disassembling. A change in P-wave behavior due to the presence of fractures was reported by Tutuncu et al. (1993) and Pyrak-Nolte et al. (1990). They focused on the change in wave attenuation resulting from the presence of a single or multiple fractures, by comparing the spectral amplitudes for intact and fractured samples at the same stress conditions. They both reported that the P-wave spectral amplitudes for fractured samples are much lower than those for intact samples at the same stress levels, indicating that higher energy loss occurred in fractured samples. There was no fluid circulation through the fracture in their samples. When the stress magnitude was increased, the energy loss was reduced and velocities increased matching our results presenting reduction in fracture width and correspondingly fracture permeability.

In our study, the decrease in initial P-wave velocity to 3.8 km/s compared to the value of 4.97 km/s calculated right after the sample saturation using 2% KCl brine indicates that the propped fracture in the sample has an effect on P-Wave propagation, resulting in slower propagation as expected . The presence of wet proppant eases the transmission of the compressional waves. As the fracture closes with increasing applied stress and proppant embeds in the fracture wall and the fracture becomes stiffer as the two halves of the fracture come closer together creating a denser medium for improved P-wave transmission.

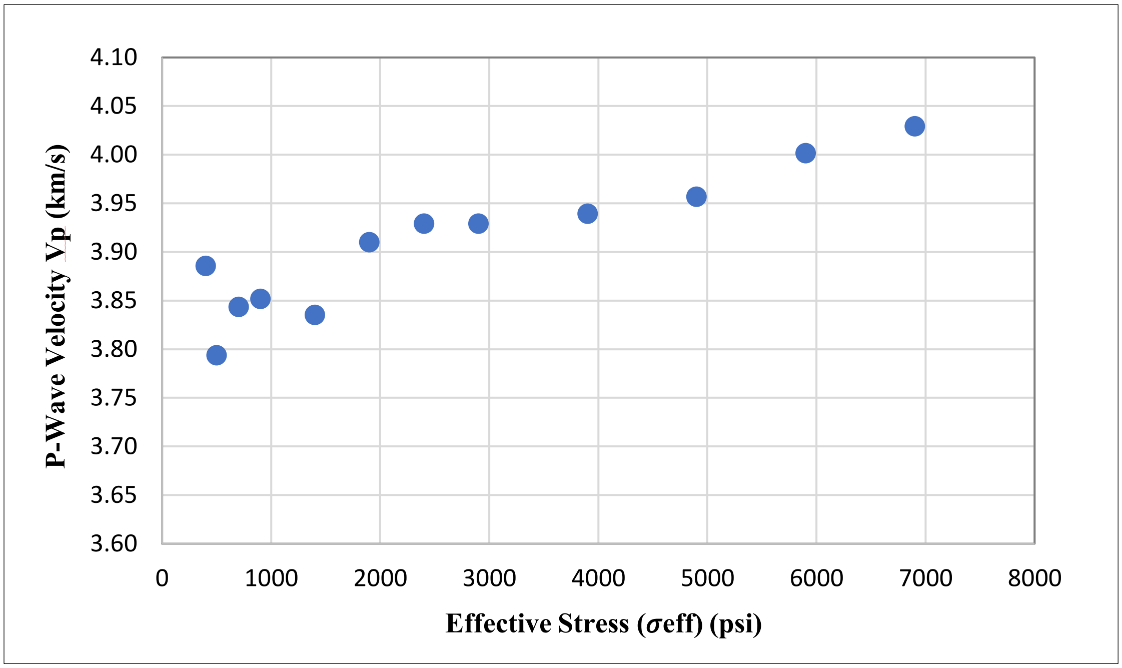

Figure 4.10: Compressional wave velocity V_p in sample VM-01, with change in effective confining stress.

The S-wave velocity increased with increasing stress and was more sensitive to change in stress compared to P-wave velocity (Figure 4.11). Values ranged from 2.11 to 2.23 km/s. There was a rapid increase in S-wave velocity between 0 and 2000 and following the fast increase, velocity increases at lower rates with increasing stress. The trend of shear wave velocity increase is similar to that of conductivity decrease due to stress where rapid decrease was observed until 2000 psi of applied stress, followed by a lower rate of decline at higher stresses.

Based on similar measurements performed using intact Eagle Ford Shale (analog for the Vaca Muerta shale) samples, using the same apparatus as this study Katsuki et al. (2016) stated that the permeability change with stress could be explained by changes in S-wave velocity to increasing stress. The S-wave used had polarization normal to the bedding planes of the samples. Similar trends to this study for changes in shear and compressional wave velocities with stress were observed by Katsuki et al. (2016) for unfractured organic-rich Eagle Ford and Pierre seal shale core plugs.

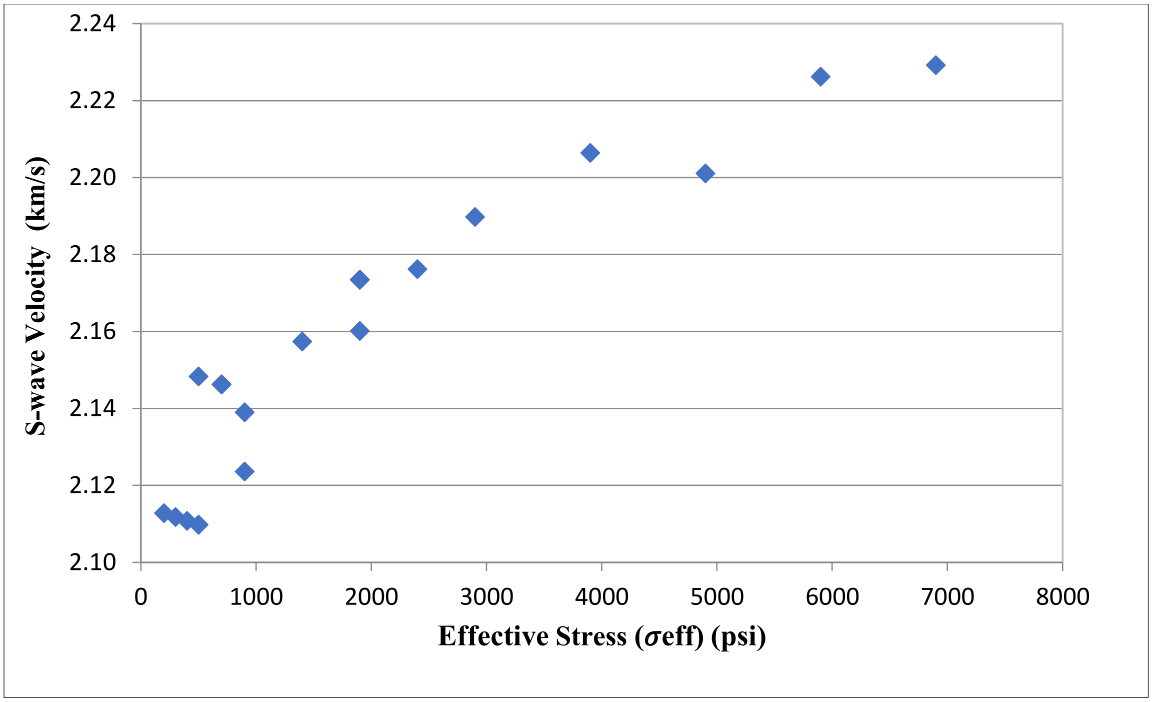

Figure 4.11: Shear Wave Velocity Vs in sample VM-01, with change in effective confining stress.

As mentioned in Chaper 3, the fracture was placed perpendicular to the direction of S-wave polarization, S-wave velocity (S_v) becomes sensitive to fracture closure. Therefore, S-wave velocity (V_{sv}) becomes sensitive to the fracture closure with stress. Shear wave velocity increased with the increasing stress which caused the proppant to embed into the fracture wall promoting further fracture closure. The increase in shear wave velocity due to increasing stress could be explained by the assumption that seismic stress is continuous across the fracture, but seismic particle displacement and seismic particle velocity are not (Pyrak-Nolte et al. 1990). The shear wave propagation behavior through the propped fracture and change in displacement due to proppant embedment into the fracture face are explained in Figure 4.12. The two fracture faces in this study are separated by and are both contacting a monolayer of proppant with a particular geometry of asperities and voids. An increase in stress causes the proppant to embed into the surface of the fracture face as described in the previous section, which results in an increment of displacement across the fracture causing the fracture faces to come closer together. The ratio between the change in stress and the displacement is defined as the specific stiffness of the fracture. The shear wave velocity increases with specific stiffness, because as the stiffness increases it means that the space through which the S-wave is propagating is becoming denser, allowing for faster propagation. Moreover, as proppant embeds into the fracture face, it partially becomes part of the rock matrix and therefore acts as a “bridge” or passage for S-wave propagation. The same phenomenon describing S-wave velocity increase with increasing stress applies to the results of the second experiment which are presented in following sections.

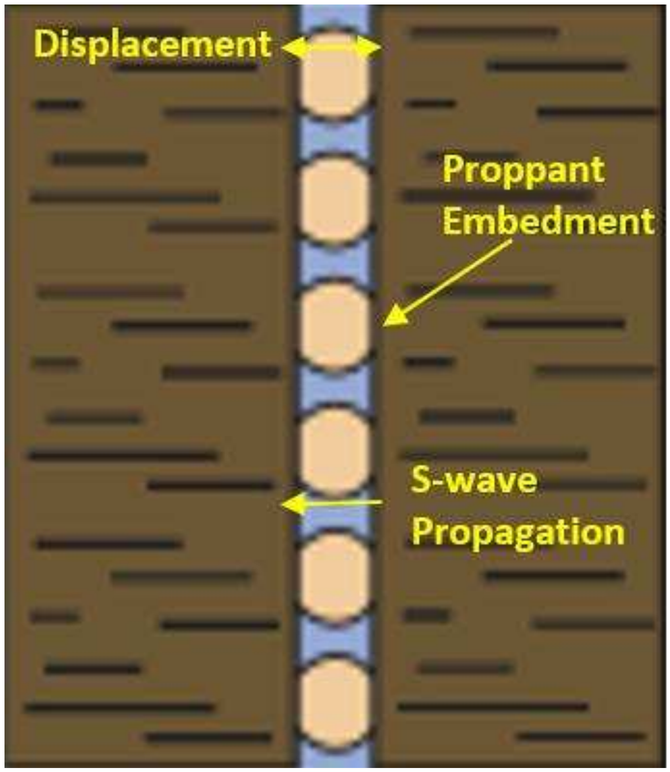

Figure 4.12: The direction of shear wave propagation with respect to the direction of the propped fracture in the tested core sample. Proppant embedment results in a change in displacement.

4.3.3 Propped Fracture Conductivity-Experiment 2

Based on the similarity in trends observed between changes in fracture conductivity and shear wave velocity with stress, it was concluded that a relationship exists between shear wave velocity and fracture stiffness. The fracture displacement with respect to change in uniaxial stress was measured using the MTS load frame. Compressional and shear wave velocities in the sample were measured simultaneously. From these coupled measurements, a relationship was obtained between the fracture stiffness and shear wave velocity. Utilizing this relation, the change in the fracture aperture was calculated using the recorded shear wave velocities as stress was increased during the triaxial test. From the change in the aperture, the fracture width was calculated and used to determine fracture permeability. In this section, the results of the recorded P and S wave velocities and the fracture permeability calculation are presented. The permeability values as a function of stress and time were calculated based on the relationship between shear wave velocity and fracture stiffness.

4.3.3.1 Effect of Stress on Wave Velocity Propagation

The variation of P-wave velocity with increase in stress is presented in Figure 4.13. Trends are similar to trends observed for P-wave velocity vs stress for the first experiment. A slow increase in velocity is observed with increasing stress and P-wave velocity values ranged between 4 and 4.32 km/s.

As observed in Experiment 1, axial deformation was negligible according to Linear Variable Displacement Transducer (LVDT) measurements recorded as a function of stress during the test (Figure 4.14) and caliper measurements taken after the sample was taken out of the triaxial cell assembly. The increase in P-wave velocity observed could be explained by the same explanation as the first experiment.

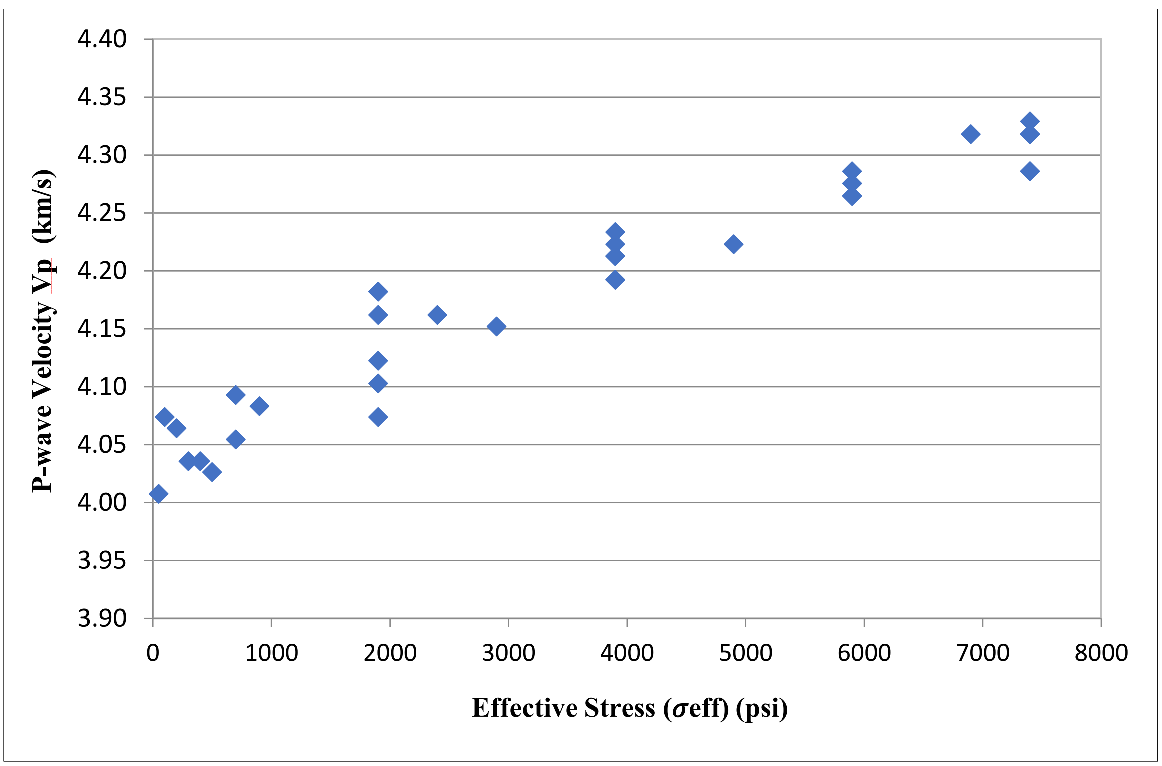

Figure 4.13: Compressional Wave Velocity Vp in sample VM-02, with change in effective confining stress.

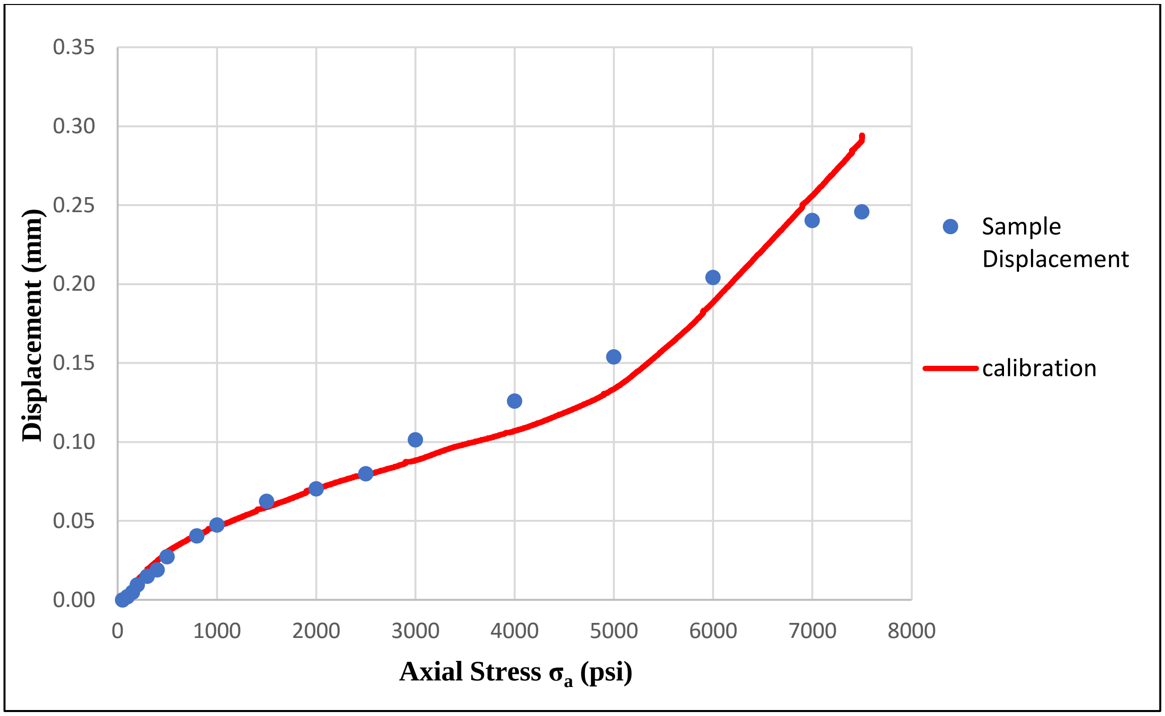

Figure 4.14: LVDT measurements as a function of stress: for calibration (without the sample) and during experiment 2 (fractured sample). The difference between the two measurements is negligible, indicating that no axial deformation occurred in the sample during the test.

Shear wave velocity through the propped fracture in sample VM-02 exhibited the same trend with increasing stress as the observed trend in the Experiment 1 as shown in Figure 4.15. The S-wave velocity is more sensitive to stress changes than the P-wave velocity. Values started from 2.1 km/s at effective stress of 30 psi and went up to 2.87 km/s at effective stress of 7400 psi. A steep increase in velocity occurs until the effective stress reaches a value of 1900 psi, followed by a slow increase at higher stress, with increasing stress. An explanation of the phenomenon behind the sensitivity of shear wave velocity to stress is also provided in the previous section.

4.3.3.2 Determination of Fracture Aperture

The uniaxial test was conducted on a square shaped sample, from the same depth as sample VM-02, filled with 20 mesh ceramic proppant. P and S wave velocity measurements were recorded as the axial was increased on the sample. Unfortunately, the sample failed as 730 lbf load was applied (equivalent to 500 psi), yet the data was sufficient to arrive with a relationship between S-wave velocity and fracture stiffness. From this relationship, the change in fracture aperture was

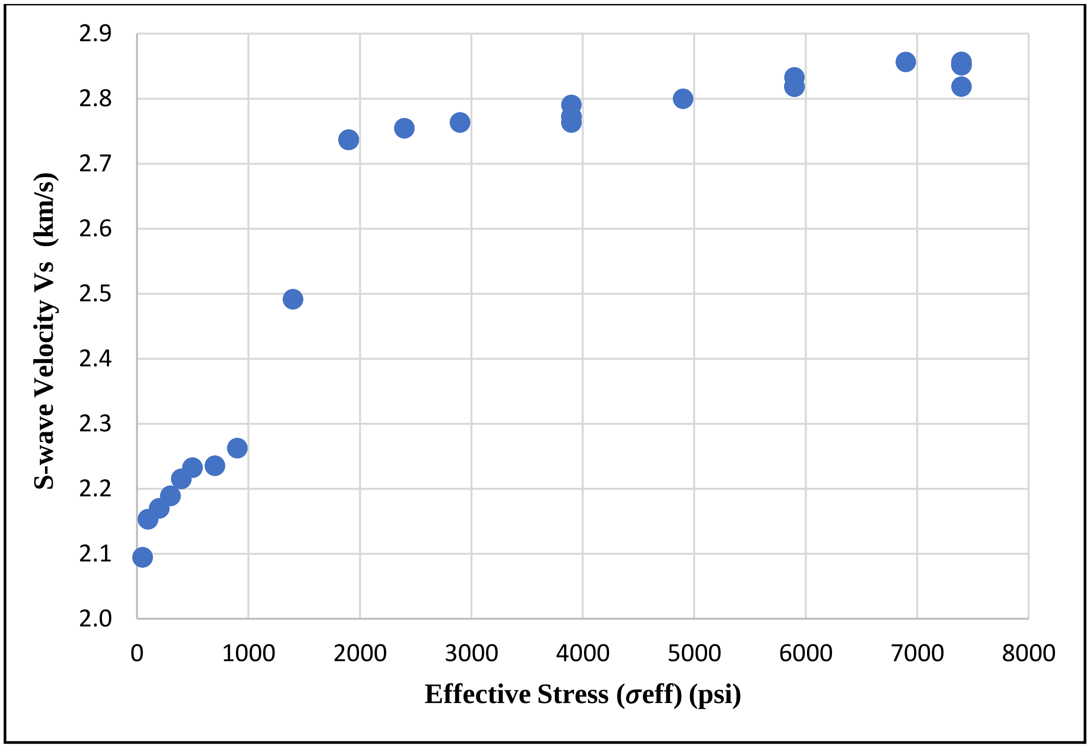

Figure 4.15: Shear Wave Velocity vs in sample VM-02, with change in effective confining stress.

calculated from recorded shear wave velocities recorded as stress was increased during the triaxial test. From the change in the aperture, the fracture width was calculated and was used to calculate fracture permeability.

The S-wave velocities from the uniaxial test and the triaxial test (experiment 2) and the displacement representing the change in fracture aperture (de_m) recorded during the uniaxial test are plotted as a function of stress in Figure 4.16. The S-wave velocity values as a function of stress are almost equal to the S-wave velocities calculated from triaxial cell measurements. Therefore, the calculation of the fracture width for VM-02 was made using the relationship between the S-wave velocity and fracture stiffness from the uniaxial tests.

The applied axial stress vs change in fracture aperture during the uniaxial stress test is presented in Figure 4.17. The slope of the curve is the fracture stiffness.

The points on the graph above fit almost perfectly into a second order polynomial curve $(y = ax^2 + bx + c)$. In this case the derivative of the curve is $2ax + b$.

The second degree polynomial equation obtained from the test is $y = 13954x^2 + 114.87 + 7.8934$. In this case the derivative which is the fracture stiffness k_n in psi/mm is represented by Equation 4.3.

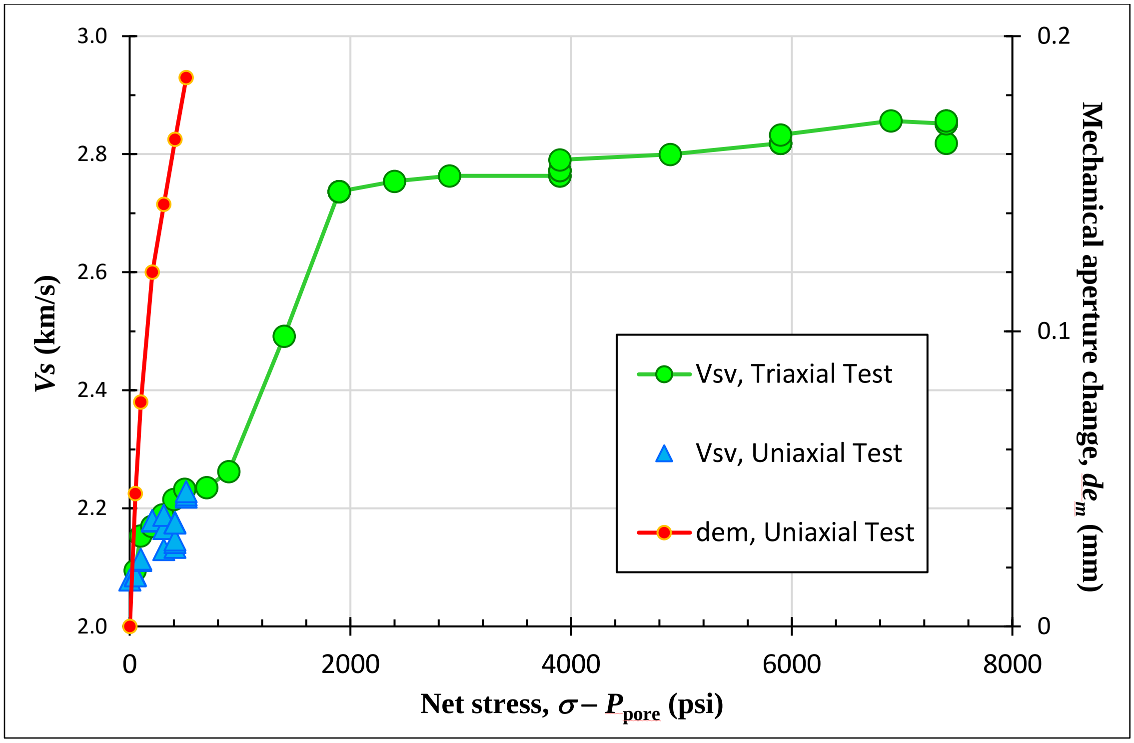

Figure 4.16: Shear wave velocities for the triaxial and uniaxial tests and fracture displacement vs net stress.

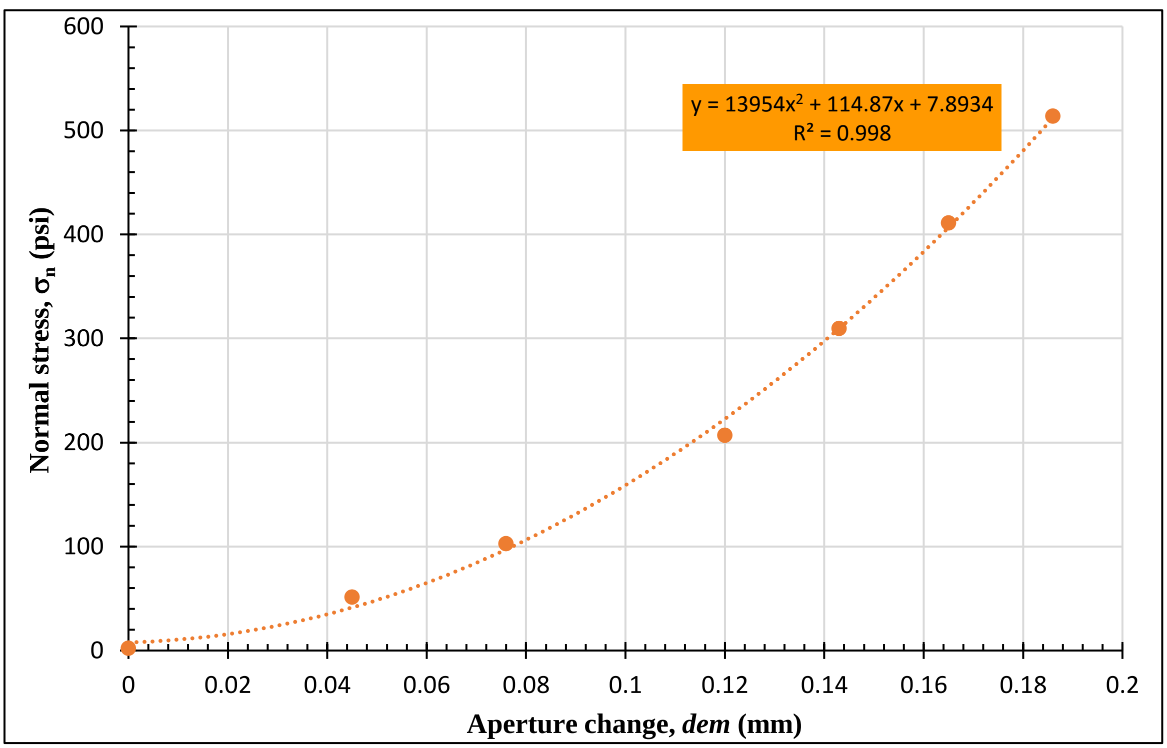

Figure 4.17: Applied axial stress using MTS loading setup vs fracture width change.

$$k_n = 2 \times 13954 de_m + 114.87 \text{ (4.3)} \tag{4.3}$$

The calculated k_n values were plotted against the S-wave velocities recorded at each applied uniaxial stress using the MTS load frame is shown in Figure 4.18.

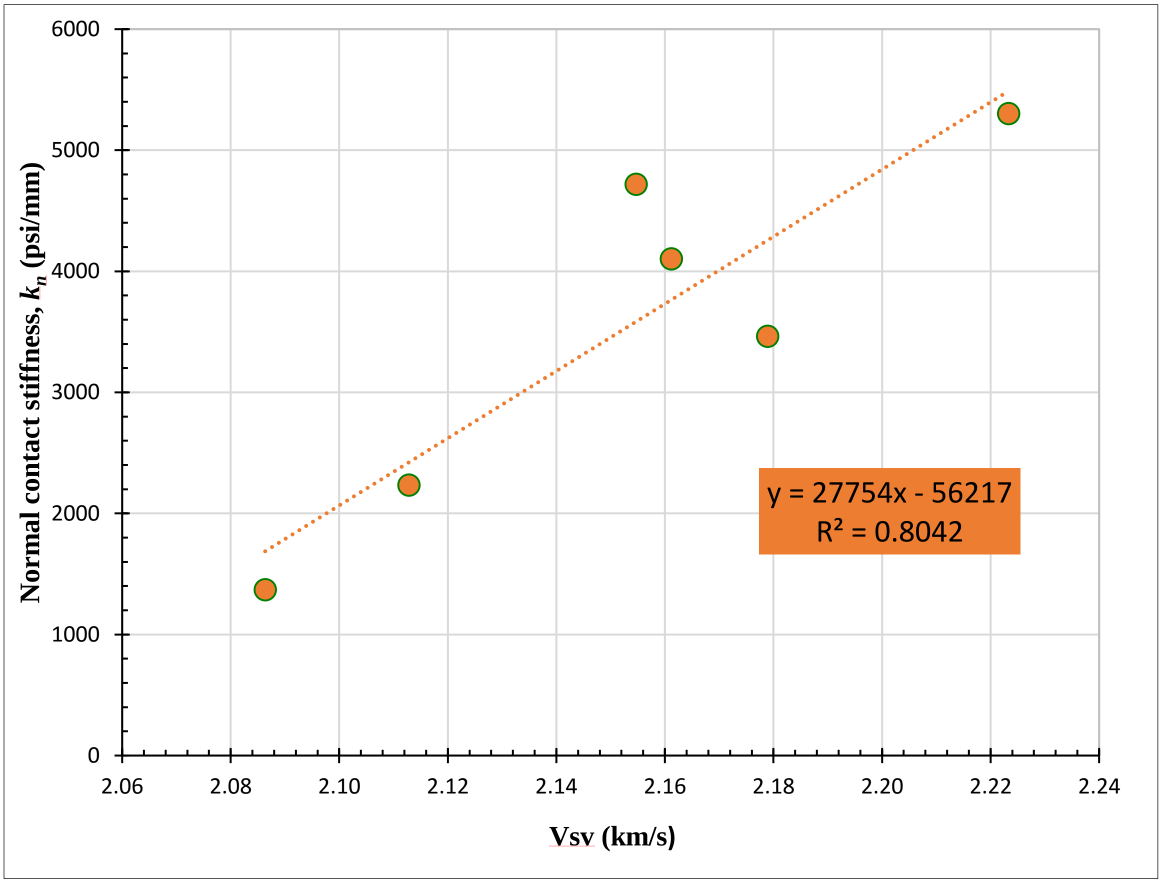

Figure 4.18: Normal fracture contact stiffness vs Vertical shear wave velocity during the uniaxial test.

A best fit line provided the linear relationship $y = 27754x - 56217$. Using this linear relationship, the fracture width was calculated as follows:

Since the equation of the line is $y = 27754x - 56217$, the relationship between fracture stiffness and the S-wave velocity could be described by Equation 4.4.

$$k_n = 27754(V_{SV}) - 56217 \tag{4.4}$$

As k_n is substituted by $\dfrac{\sigma}{de_m}$, the previous equation could be described as follows:

$$\frac{\sigma}{de_m} = 27754(V_{SV}) - 56217 \tag{4.5}$$

Effective closure stress values applied in the propped fracture conductivity triaxial test and the corresponding shear wave velocities are substituted in Equation 4.5 to calculate the change in fracture width de_m which is the only unknown in the equation. To obtain the fracture width at each stress state de_m subtracted from the original width of the fracture measured before subjecting the sample to triaxial state stress conditions d_o (Equation 4.6). The relationship between calculated fracture width and stress, during triaxial testing is presented in Figure 4.19. The fracture width decreased from 1.04 mm to 0.52 mm, amounting to 50% reduction.

$$w_f = do - de_m \tag{4.6}$$

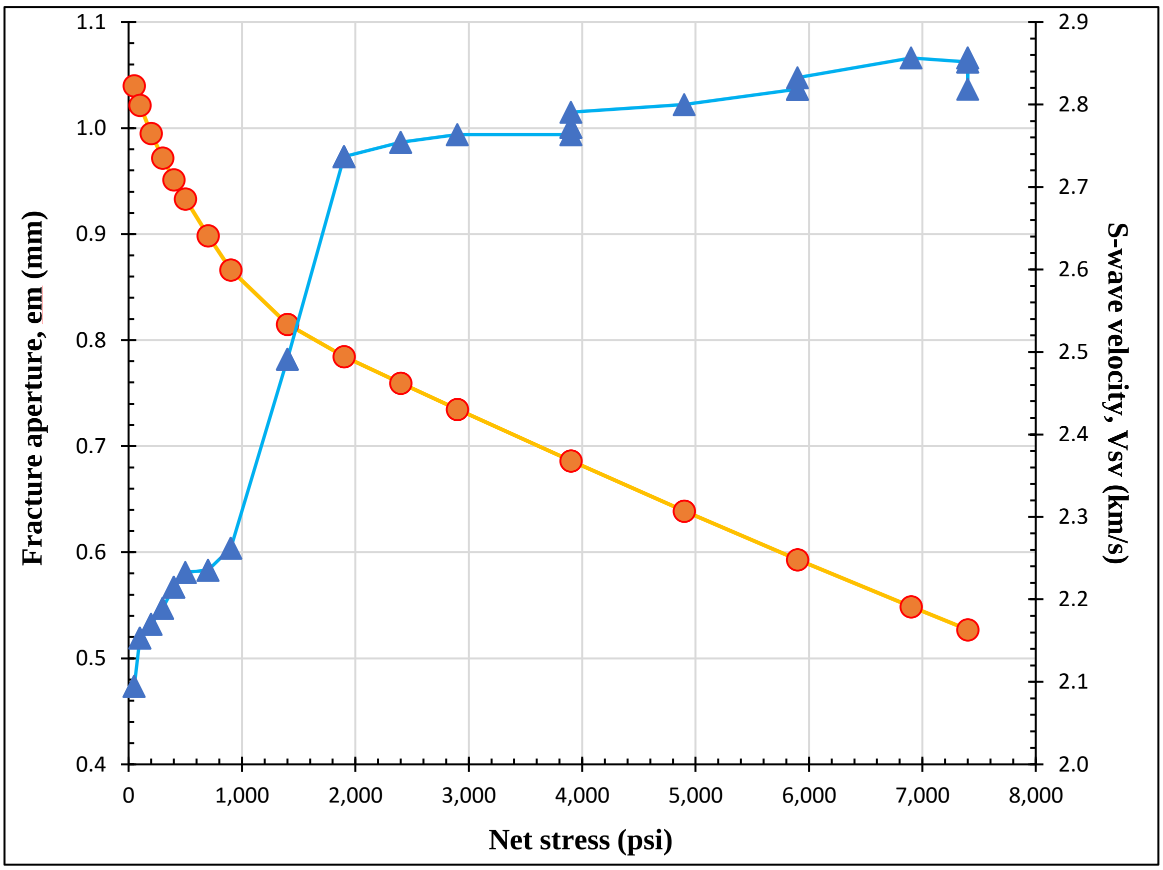

Figure 4.19: Fracture aperture w_f (orange line) and Shear wave Velocity (blue line) V_s as a function of stress.

It must be noted that since a limited number of samples have been tested in this study, to create a more general relation, additional samples should be tested to confirm the relationship between the fracture contact stiffness and shear wave velocity.

A comparison was made between fracture conductivity values obtained from the traditional method used by Stim-lab (Equation 4.2) and values obtained by multiplying the fracture permeability (k_f) and fracture width (*em*) obtained from our fracture stiffness-shear wave velocity correlation. An explanation on how the fracture permeability is obtained is provided in following sections.

Values obtained for each method as function of stress are presented in Table 4.2. A negligible difference exists between the two methods, with an average percentage difference of 3.5%. Therefore, it could be concluded that using our method to estimate fracture width yields fracture conductivity values within a reliable acceptable range, since it is comparable with the method used by industry.

Table 4.2: Conductivity values as a function of net stress calculated from this study's S-wave method and the method used by Stim-Lab.

Net Stress (psi)	1900	2900	3900	4900	5900	6900	7400
Conductivity S-wave-Method (D.cm)	2.1	1.92	1.53	1.03	0.81	0.51	0.44
Conductivity Stim-Lab (D.cm)	2.2	1.98	1.58	1.06	0.84	0.52	0.45

4.3.3.3 Propped Fracture Permeability

To obtain more accurate differential pressure transducer reading of the pressure gradient through the propped fracture in the sample a new setup was created. As noted in Chapter 3, the permeability of the porous filters used in this stage is negligible. To obtain propped fracture permeability, Darcy's equation (Equation 4.7) was applied incorporating the fracture aperture w_f obtained from the fracture stiffness-shear wave velocity relations, explained in the previous section.

$$k = \frac{q\mu l}{w_f h \Delta p} \tag{4.7}$$

The calculated permeability indicated non-Darcy flow conditions existed during the tests. The permeability values obtained for each rate at given stress state were noticeably different as shown in Figure 4.20. In addition, the relationship between the pressure drop and flow rate was nonlinear.

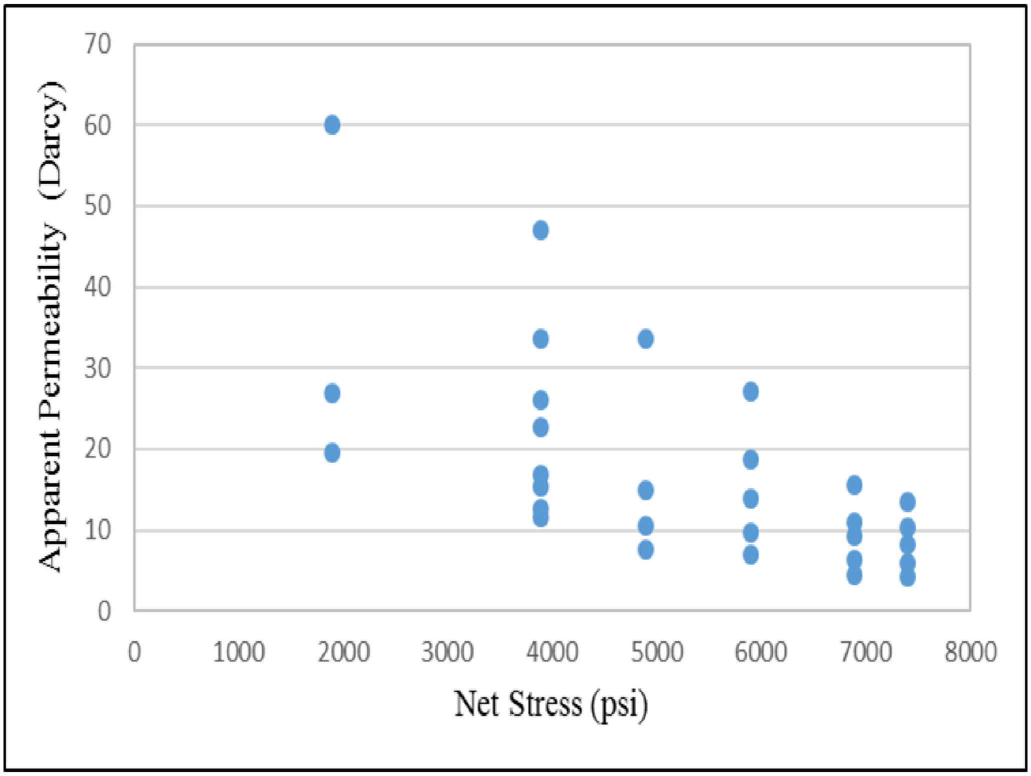

Figure 4.20: Variation in fracture permeability values obtained at same stress state conditions.

In order to obtain absolute values of permeability for each stress state, Forchheimer's method was used. The reciprocal of the calculated permeability using Equation 4.8 was plotted versus the flow rate to obtain a linear relationship as shown in Figure 4.21. The values plotted are at an applied effective closure stress of 4900 psi. All the Forchheimer plots for all applied the stress states are presented in Appendix B. The intercept of the line $1/k_d$ is the reciprocal of the permeability value k_d.

The calculated short-term permeability values (measurements taken after 15 minutes of applied stress) based on the intercepts from Forchheimer plots at each stress state are presented in Table 4.3. Fracture permeability reduction is 92% when net stress is increased from 1900 to 7400 psi.

The high percentage of reduction in permeability occurred due to the fact that only a monolayer of proppant was applied to the sample. At higher concentrations of multiple layers of proppants the closure of the fracture will depend on the proppant and therefore the proppants might contribute better to maintaining fracture conductivity. However, with a monolayer the amount of embedment and fracture closure depends strongly on the sample properties. Therefore, the high percentage of

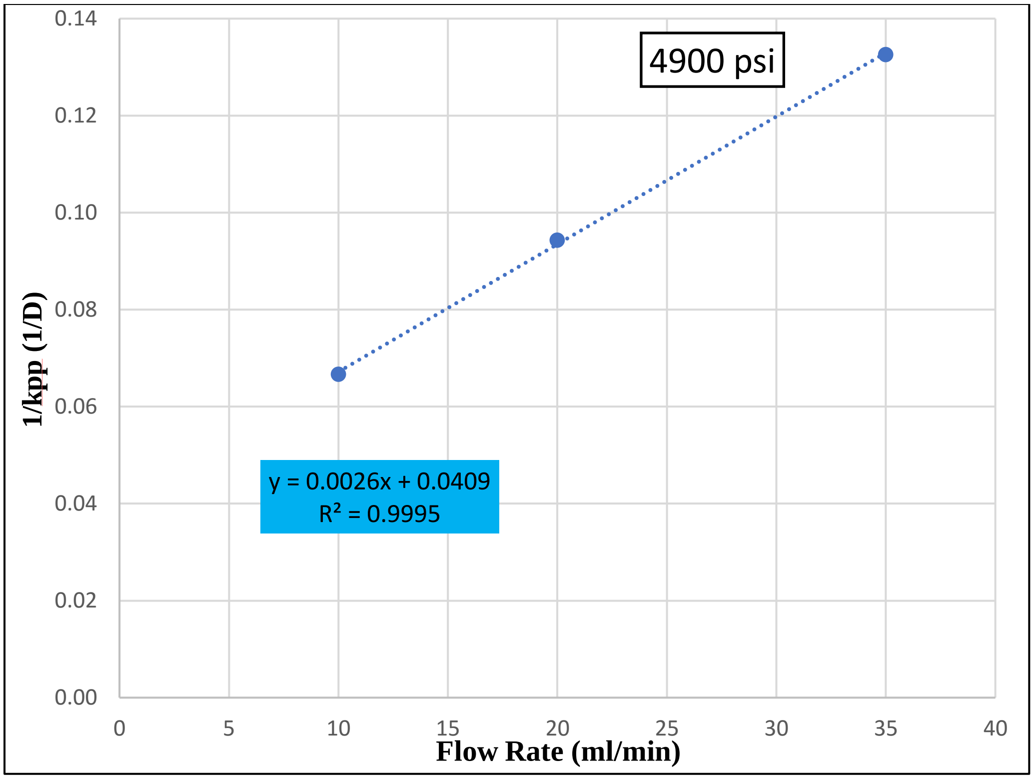

Figure 4.21: Forchheimer's plot: The reciprocal of the apparent permeability $1/k_{app}$ versus flow rate q at 4900 effective closure stress.

permeability reduction might have been attributed to the high clay content of sample which made it easier to deform from embedment. The main reason behind the permeability reduction at proppant monolayer concentration is proppant embedment, where due to high localized stress, the proppant-rock interaction goes directly to the deformation of the rock. This phenomenon is evident in Figure 4.8.

Table 4.3: Short term permeability test results

Effective Closure Stress (psi)	1900	2900	3900	4900	5900	6900	7900
Permeability (Darcy)	167	41.8	34.7	24.4	22.2	15.3	13.2

A plot of short term conductivity as a function of effective stress is shown in Figure 4.22. Permeability decreases steeply at small applied stress up to 2900 psi and continues to decrease at a lower rate at higher stresses. The difference in trends observed between the samples VM-01 and

VM-02 could be attributed to the fact that the proppant layer in VM-01 flowed from the fracture face to the porous filter during the first experiment. This flow might have led to an earlier fracture closure due to the fact that the fracture is not filled with proppant reducing the resistance to closure stress. On the other hand, proppants were in place within the fracture space in VM-02 until the sample was taken out of the triaxial cell assembly.

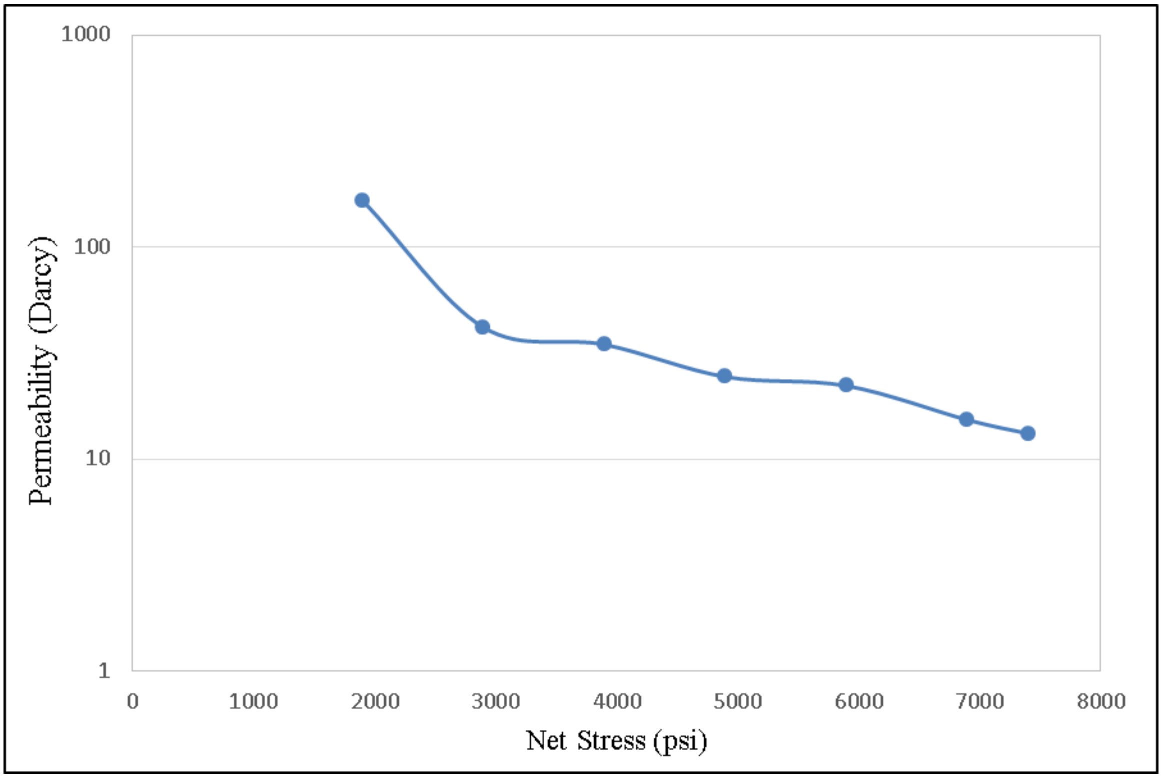

Figure 4.22: Short term fracture permeability versus stress.

It is important to realize the effect of long term exposure of the propped fracture to the stress. Forchheimer plots for permeability tests taken at different timing at the same stress state condition (7400 psi net stress) are shown in Figure 4.23. Different permeability values are obtained from the plot at each permeability test.

Long term fracture permeability results for our experiments are presented in Figure 4.24. Long term fracture permeability measurements were taken at effective closure stresses of 1900, 3900, 5900 and 7400 psi. The fracture permeability at a given stress decreases and stabilizes at about 2 days based on our measurements. Permeability decreased rapidly over the 2 days at 1900 psi net

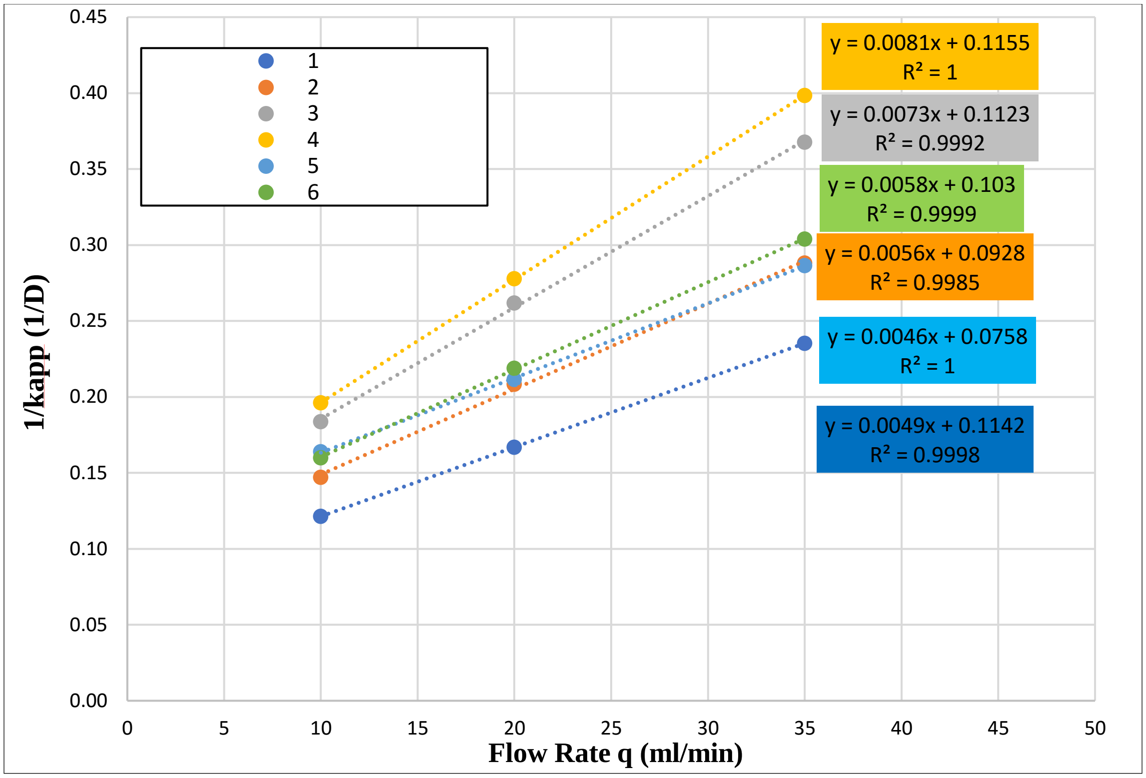

Figure 4.23: Forchheimer plot for long term permeability measurement at 7400 psi effective closure stress.

confining stress, indicating that a significant amount of embedment occurred over this period. Little change occurred when confining stress was increased from 2900 to 3900, indicating that little proppant embedment occurred at that stage. When net confining stress reached 4900 psi, the permeability began to decrease.

Cobb and Farrell (1986) discussed the occurrence of the proppant reorientation during long term conductivity tests leading to variability in permeability values even at the same stress state. Samples from the Canadian shale with similar mineralogy (31% quartz and 28.8% clay) were tested for propped fracture conductivity by Pedlow and Sharma (2014) using 40/70 mesh white sand proppant. As expected lower permeability values were obtained as they were using weaker proppant. A similar trend was observed however for the decrease in fracture permeability at higher stresses where faster increase was observed when stress reached 6000 psi, compared to the constant permeability at 4000 psi as shown in Figure 4.25. Pedlow and Sharma (2014) also related changes of permeability to proppant embedment.

It could be argued that higher permeability values are obtained in our experiment due to the roughness of the natural fracture filled with proppant, which could lead to fracture displacement

(Ghanizadeh et al. 2016). However, according to the LVDT reading during the triaxial test, both halves of the sample remained intact as there no signs of axial displacement, possibly due to the presence of the adhesive tape connecting the 2 halves.

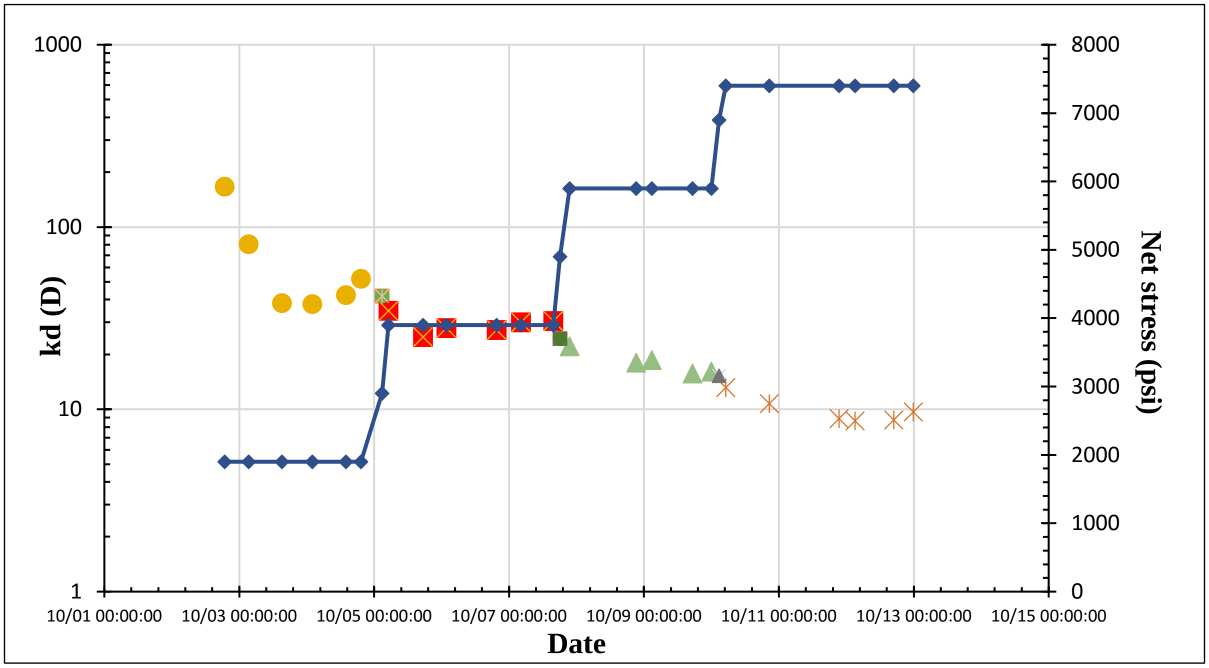

Figure 4.24: Long term fracture permeability versus stress.

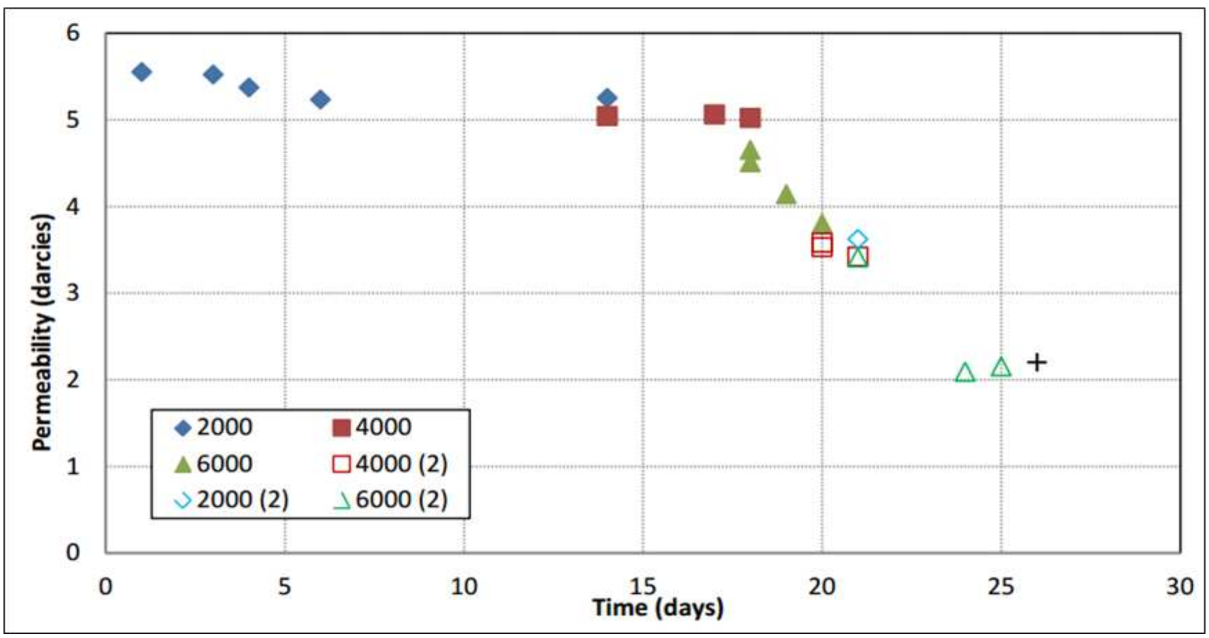

Figure 4.25: Long term fracture permeability versus stress for Canadian shale fractured samples propped with 40/70 mesh white sand (Pedlow and Sharma 2014).

A similar trend of change of short term permeability and shear wave velocity with respect to change in stress is observed. The decrease in permeability appears to correlate proportionally with increase in S-wave velocity. This is partially due to the reason that permeability values were calculated using fracture width obtained for relationship between stiffness and shear wave velocity. This relationship is displayed clearly when the two parameters are plotted against effective stress as shown in Figure 4.26.

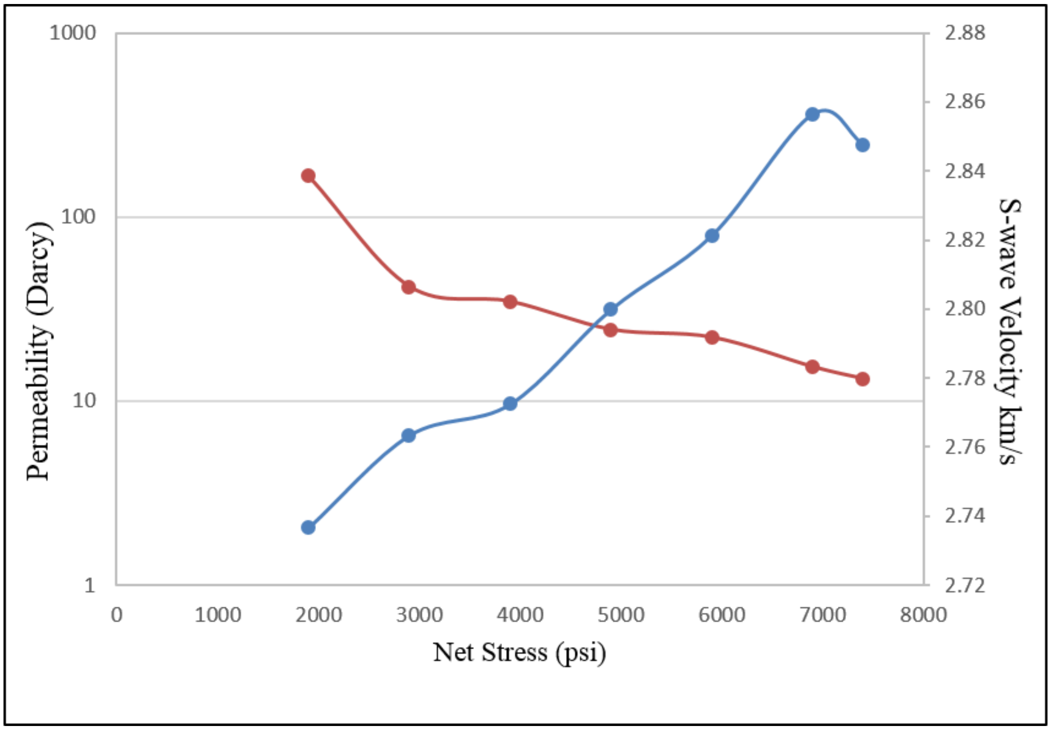

Figure 4.26: Shear wave velocity and permeability as a function of stress presents good relationship between the two parameters.

For long terms conductivity measurements, decrease in measured permeability with time did not correspond to changes in S-wave velocity, which stayed constant throughout the period of each applied effective stress step. This may be due to the fact that during the duration of each long term conductivity test, the proppants reorient on the fracture face, not contributing significantly to change in fracture width. It is less likely that the change in the geometry of the flow path, which contributed to the variability of permeability over time, was due to proppant rearrangement. This is because only a monolayer of proppant was placed on the fracture face. Therefore, it could be concluded that the change in permeability over time at the same stress occurred due to sloughing of the fracture face and formation fines migration.

CHAPTER 5

CONCLUSION AND RECOMMENDATIONS FOR FUTURE WORK

The quantification of degradation of mechanical properties due to 2% KCl interaction and the propped fracture conductivity degradation due to increasing stress at triaxial stress conditions was performed successfully in Vaca Muerta shale samples. Along with fracture permeability measurements, compressional and shear wave velocity measurements were collected to understand the relationship between those parameters and fracture conductivity. Based on results and observations of the tests performed we were able to come up with the conclusions and recommendations described in the following sections.

5.1 Conclusions

1. The use of KCl as base fluid for fracturing fluids used in stimulation of the lower Vaca Muerta formation is recommended to reduce clay swelling that is induced through clay water reactions. By measuring acoustic wave velocities before and after saturation in 2% KCl water, Young's modulus as a result of fluid interaction with Vaca Muerta samples was quantified and the reduction was found to be not significant.
2. Operators in the Vaca Muerta formation might plan to consider other proppant types when stimulating the formation after thorough economic analysis. The largest size of proppants used in this study indicated significant embedment into the fracture wall. It must be noted that the triaxial cell was exposed to temperature of 100°F which amounts to half of the realistic borehole conditions. Therefore, higher embedment is anticipated in borehole conditions. Moreover, the conductivity reduction was 92%, over an approximately one month testing duration. Longer exposure to fracturing fluid may also result in higher conductivity reduction in the field.
3. Non-Darcy flow in fractures is very likely with high flow rates during permeability tests which much cause uncertainty in permeability measurements but present more realistic flow conditions present bottomhole.
4. Long term propped fracture conductivity is more representative of the fracture conductivity

measured in the experiments than the short term conductivity. Short term conductivity results are an overestimation of the conductivity. This conclusion was made based on the results obtained from long term measurements, where fracture permeability decreased and then finally stabilized within 2 days of being exposed to the same closure stress.

5. A linear relationship exists between shear wave velocity and fracture contact stiffness. From this relationship, fracture aperture could be calculated. The relationship yields conductivity values that are close to values from calculation of fracture conductivity as a fraction of overall sample conductivity. Further tests should be performed on several samples from the Vaca Muerta formation at different proppant concentrations to be able to confirm our method of aperture calculation as a generalized method for propped fractured shale samples' fracture width calculation.
6. The UNGI triaxial cell has been used to perform short and long term fracture conductivity tests. Apart from simulating more realistic borehole conditions, transducers built in the cell made the measurements of acoustic wave velocities possible for establishing correlations between the shear wave velocity and the fracture contact stiffness, which made the quantification of fracture closure possible. In field operations, the majority of the measurements conducted are wave propagation based (seismic, dipole sonic log, microseismic). Utilizing velocity based permeability and fracture conductivity will allow for efficient use of the log and microseismic data for evaluation of the fracture conductivity in the stimulated reservoir volume of the reservoir. Moreover, by identifying propped fractures that were closed due to embedment through S-wave velocity measurements, candidate wells for refracturing could be selected.

5.2 Recommendations for Future Work

The Vaca Muerta is an emerging play and therefore more tests need to be performed to provide an adequate assessment of fracture fluids and proppants to be used in the formation. More proppant types should be compared for proper selection of the optimum type in the formation. Moreover, reactions with fracture fluids other than 2% KCl should be examined to get a better quantification of geomechanical properties that results due to interactions with fracturing fluids and the Vaca Muerta formation. To examine the effect of sample mineralogy on conductivity damage, samples at different depth of the formation could be used in the experiments. For accurate measurement of fracture width w_f, an LVDT with resistance to high pressure and temperatures could be installed inside the cell to capture the displacement of the fracture. This could help assess the reliability of the relationship between fracture contact stiffness and S-wave velocity in fracture width estimation. Finally, anisotropic stress conditions should be applied to capture the anisotropic nature of shale reservoirs and a comparison can be made with the isotropic fracture conductivity measurements.

REFERENCES CITED

Aguirre-Uretta, M., Price, G., and Ruffel, A. 2008. Southern Hemisphere Early Cretaceous (Valanginian-Early Barremian) Carbon and Oxygen Isotope Curves from the Neuquén Basin, Argentina. *Cretaceous Research*, 29(1): 87–99. http://dx.doi.org/10.1016/j.cretres.2007.04.002.

Akrad, O., Miskimins, J., and Prasad, M. 2011. The Effects of Fracturing Fluids on Shale Rock Mechanical Properties and Proppant Embedment. Presented at the SPE Annual Technical Conference and Exhibition, Denver, Colorado, USA, 30 October-2 November. SPE 146658-MS. http://dx.doi.org/10.2118/146658-MS.

Alramahi, B. and Sundberg, M. 2012. Proppant Embedment and Conductivity of Hydraulic Fractures in Shales. Presented at the 46th U.S. Rock Mechanics/Geomechanics Symposium, Chicago, Illinois, USA, 24-27 June. ARMA-2012-291.

Anderson, H., Bratrud, T., and Delorey, J. 1982. A Logical Approach to Fracture Fluid Selection. *Journal of Canadian Petroleum Technology*, 21(06): 105–111. PETSOC–82–06–06. http://dx.doi.org/doi:10.2118/82-06-06.

API RP 61, *Recommended Practice for Evaluating Short-Term Proppant-Pack Conductivity*. 1989. Washington, DC: API.

API RP19D, *Recommended Practice for Measuring the Long-term Conductivity of Proppants*, First Edition (ISO 13503-5:2006, Identical) (Includes July 2008 Errata). 2008 Washington, DC:API.

Baree, R., Cox, S., Baree, V., and Conway, M. 2003. Realistic Assessment of Proppant Pack Conductivity for Material Selection. Presented at the SPE Annual Technical Conference and Exhibition, Denver, Colorado. USA, 5-8 October. SPE 84306-MS. http://dx.doi.org/10.2118/84306-MS.

Brannon, H., Malone, A., Rickards, A., Wood, W., Edgeman, J., and Bryant, J. 2004. Maximizing Fracture Conductivity with Proppant Partial Monolayers: Theoretical Curiosity or Highly Productive Reality? Presented at the SPE Annual Technical Conference and Exhibition, Houston, Texas, USA, 26-29 September. SPE-90698-MS. http://dx.doi.org/10.2118/90698-MS.

Briggs, K. 2014. *The Influence of Vertical Location on Hydraulic Fracture Conductivity in the Fayetteville Shale*. MS thesis, Texas A&M University, College Station, Texas (May 2014).

Cipolla, C. L., Warpinski, N. R., Mayerhofer, M., Lolon, E. P., and Vincent, M. 2010. The Relationship Between Fracture Complexity, Reservoir Properties, and Fracture Treatment Design. *SPE Production & Operations*, 25(04): 438 – 452. SPE–115769–PA. http://dx.doi.org/10.2118/115769-PA.

Cobb, C. and Farrell, J. 1986. Evaluation of long term proppant stability. Presented at the International Meeting on Petroleum Engineering, Beijing, China 17-20 March. SPE-14133-MS. http://dx.doi.org/10.2118/14133-MS.

Coker, C. E. and Mack, M. M. 2013. Proppant selection For Shale Reservoirs: Optimizing Conductivity, Proppant Transport and Cost. Presented at the SPE Unconventional Resources Conference Canada, Calgary, Alberta, Canada, 5-7 November. SPE-167221-MS. http://dx.doi.org/10.2118/167221-MS.

Colmenares, L. and Zoback, M. 2001. Statistical Evaluation of Six Rock Failure Criteria Constrained by Polyaxial Test Data. Presented at the 38th U.S. Symposium on Rock Mechanics, Washington, District of Columbia, 7-10 July. ARMA-01-1251.

Corapcioglu, H. 2014. *Fracturing Fluid Effects on Young's Modulus and Embedment in the Niobrara Formation*. Master's thesis, Colorado School of Mines, Golden, Colorado (May 2014).

Coulter, G. and Wells, R. D. 1972. The Advantages of High Proppant Concentration in Fracture Stimulation. Journal of Petroleum Technology, 24(06): 643–650. SPE–3298–PA. http://dx.doi.org/10.2118/3298-PA.

Daneshy, A. 2007. Pressure Variations Inside the Hydraulic Fracture and its Impact on Fracture Propagation, Conductivity, and Screen-Out. 22: 107–111. SPE–95355–PA. http://dx.doi.org/10.2118/95355-MS.

Drucker, D. and Prager, W. 1952. Soil Mechanics and Plastic Analysis or Limit Design. *Engineering Fracture* Mechanics, 10(6): 157-165. http://dx.doi.org/10.1016/j.engfracmech.2007.07.008.

Duenckel, R., Moore, N., O'Connell, L., Abney, K., Drylie, S., and Chen, F. 2016. The Science of Proppant Conductivity Testing-Lessons Learned and Best Practices. Presented at the SPE Hydraulic Fracturing Technology Conference, The Woodlands, Texas, USA, 9-11 February. SPE-179125-MS. http://dx.doi.org/10.2118/179125-MS.

EIA. 2013. Technically Recoverable Shale Oil and Shale Gas Resourses: An Assessment of 137 Shale Formation in 41 Countries Outside the United States. Washington, DC (June 2013).

EIA. 2014. Updates to the EIA Eagle Ford Play Maps. Washington, DC (December 2014).

Ewy, R. T. 1999. Wellbore-Stability Predictions by Use of a Modified Lade Criterion. *SPE Drilling & Completion*, 14(02): 85-91. SPE–56862–PA. http://dx.doi.org/10.2118/56862-PA.

Forchheimer, P. 1914. *Hydraulik*. Berlin, Germany: Teubner.

Freeman, E. R., Anschutz, D. A., Rickards, A. R., and Callanan, M. J. 2009. Modified API/ISO Crush Tests with a Liquid-Saturated Proppant Under Pressure Incorporating Temperature, Time, And Cyclic Loading: What Does It Tell Us? Presented at the SPE Hydraulic Fracturing Technology Conference, The Woodlands, Texas, USA, 19-21 January. SPE-118929-MS. http://dx.doi.org/10.2118/118929-MS.

Ghanizadeh, A., Clarkson, C. R., Deglint, H., Vahedian, A., Aquino, S., and Wood, J. M. 2016. Unpropped/Propped Fracture Permeability and Proppant Embedment Evaluation: A Rigorous Core-Analysis/Imaging Methodology. Presented at the Unconventional Resources Technology Conference, San Antonio, Texas, USA, 1-3 August. URTEC-2461613-MS. http://dx.doi.org/10.2118/175954-MS.

Guzek, J. 2014. *Fracture Conductivity of the Eagle Ford Shale*. Master's thesis, Texas A&M University, College Station, Texas (August 2014).

Hernández Bilbao, E. 2016. *High Resolution Chemostratigraphy , Sequence Stratigraphic Correlation, Porosity and Fracture Characterization of the Vaca Muerta Formation, Nuequen Basin, Argentina*. Ph.D. thesis, Colorado School of Mines, Golden, Colorado (May 2016).

Hoek, E. and Brown, E. 1980. Empirical Strength Criterion for Rock Masses. *Rock Mechanics and Rock Engineering*, 106(4): 1013–1035. http://dx.doi.org/10.1007/s00603-009-0044-2.

Holditch, S., Perry, K., and Lee, J. 2007. Unconventional Gas. Working Document of the NPC Oil and Gas Study, Topic #29, National Petroleum Council (July 2007).

Howell, J., Schwar, E., and Spalletti, L. 2005. The Neuquén Basin: An Overview. In the Neuquén Basin, Argentina: A Case Study in Sequence Stratigraphy and Basin Dynamics. *Geological Society, London, Special Publications,* **252**(1): 1-14. http://dx.doi.org/10.1144/gsl.sp.2005.252.01.01.

Hudson, J. and Harrison, J. 1997. *Engineering Rock Mechanics an Introduction to the Principles*. Oxford, UK: Pergamon. http://dx.doi.org/10.1016/b978-008043864-1/ 500 16-1.

Jaeger, J. and Cook, N. 1979. *Fundamentals of Rock Mechanics*, third edition. London, UK: Chapman and Hall.

Jansen, T. and Zhu, D. 2015. The Effect of Rock Mechanical Properties on Fracture Conductivity for Shale Formations. Presented at the SPE Hydraulic Fracturing Technology Conference, 3-5 February, The Woodlands, Texas. SPE-173347-MS. http://dx.doi.org/10.2118/173347-MS.

Kamenov, A., Zhu, D., Hill, A. D., and Zhang, J. 2013. Laboratory Measurement of Hydraulic Fracture Conductivities in the Barnett Shale. Presented at the SPE Hydraulic Fracturing Technology Conference, 4-6 February, The Woodlands, Texas. SPE-163839-MS. http://dx.doi .org/doi:10.2118/163839-MS.

Katsuki, D., Deben, A. P., Adekunle, O., Rixon, A. J., and Tutuncu, A. N. 2016. Stress-Dependent Permeability and Dynamic Elastic Moduli of Reservoir and Seal Shale. Presented at the Unconventional Resources Technology Conference, San Antonio, Texas, USA, 1-3 August. URTEC-2461613-MS. http://dx.doi.org/10.15530-urtec-2016-2461613.

Kazemi, H. 2015. Naturally Fractured Reservoirs Class Notes.

Kernan, H. 2014. *Electrofacies, Elemental Composition, and Source Rock Characteristics Along Seismic Reflectors of the Vaca Muerta Formation in the Loma La Lata Area, Neuquén Basin*, Argentina. MS thesis, Colorado School of Mines, Golden, Colorado (May 2014).

Kim, C. and Willingham, J. 1987. Flow Response of Propped Fracture to Repeated Production Cycles. Presented at the SPE Annual Technical Conference and Exhibition, Dallas, Texas, USA, 27-30 September. SPE-16912-MS. http://dx.doi.org/10.2118/16912-MS.

Kietzmann, D.A., Martin-Chivelet, J., Palma, R.M., Lopez-Gomez, J., Lescano, M., and Concheyro, A. 2011. Evidence of Precessional and Eccentricity Orbital Cycles in a Tithonian Source Rock: The Mid-Outer Carbonate Ramp of the Vaca Muerta Formation, North Neuquén Basin, Argentina. The American Association of Petroleum Geologists Bulletin 95 (9): 1459-1474.

Kranz, R., Frankel, A., Englder, T., and Scholz, C. 1979. The Permeability of Whole and Jointed Barre Granite. *International Journal of Rock Mechanics and Mining Sciences & Geomechanics Abstracts*, 16(4): 225–234. http://dx.doi.org/10.1016/0148-9062(79)91197-5.

Kugler, R. L. 1985. Source Rock Characteristics, Los Molles and Vaca Muerta Shales, Neuquén Basin, West-Central. *AAPG Bulletin*, 69. http://dx.doi.org/10.1306/ad4620ce-16f7-11d7-865000102c1865d.

Kullam, J., Carbo Ceramics. (2011). *The Complicated World of Proppant Selection (Retrieved on 1/16/2016)*. http://images.sdsmt.edu/learn/speakerpresentations/Kullman.pdf

Kundert, D. and Mullen, M. 2009. Proper Evaluation of Shale Gas Reservoirs Leads to a More Effective Hydraulic-Fracture Stimulation. Presented at the SPE Rocky Mountain Petroleum Technology Conference, Denver, Colorado, USA. SPE-123586-MS. http://dx.doi.org/10.2118/123586-MS.

Kuuskraa, V. A., Stevens, S. H. and Moodhe K. 2013. EIA/ARI World Shale Gas and Shale Oil Resource Assessment. Advanced Resources International, Inc (June 2013).

Lade, P. 1977. Elastolastic Stress-Strain Theory for Cohesionless Soil with Curved Yield Surfaces. *International Journal of Solids and Structures*, 13(11): 1019–1035. http://dx.doi.org/10.1016/0020-7683(77)90073-7.

Licitra, D., Lovrincevich, E., Vittore, F., and Quiroga, J. 2015. Sweet Spots in Vaca Muerta: Integration of Subsurface and Production Data in Loma Campana Shale Development, Argentina. Presented at the Unconventional Resources Technology Conference, San Antonio, TX, 20- 22 July. SPE-178563-MS. http://dx.doi.org/10.2118/178563-MS.

Liebowitz, H. 1968. *Fracture: an advanced treatise.* Vol. 2, Mathematical fundamentals. New York: Academic press.

Manceda, R. and Figueroa, D. 1995. Inversion of the Mesozoic Nuequen Rift in The Malargue Fold and Thrust Belt, Mendosa, Argentina. *Journal of Structural Geology*, Memoir 62(7): 369–382. http://dx.doi.org/10.1016/j.jsg.2008.03.007.

Mayerhofer, M. J., Lolon, E. P., and Youngblood, J. E. 2006. Integration of Microseismic Fracture Mapping Results with Numerical Fracture Network Production Modeling in the Barnett Shale. Presented at the SPE Annual Technical Conference and Exhibition, San Antonio, Texas, USA, 24-27 September. SPE-102103-MS. http://dx.doi.org/10.2118/102103-MS.

Meissner, F. 1984. *Petroleum Geochemistry and Basin Evaluation*, volume 35. Tulsa, Oklahoma: American Association of Petroleum Geologists.

Miskimins, J. 2015. Advanced Well Stimulation Class Notes.

Nur, A. and Simmons, G. 1969. The Effect of Saturation on Velocity in Low Porosity Rocks. *Earth and Planetary Science Letters*, 7: 183–193. http://dx.doi.org/10.1016/0012 821x(69)90035-1.

Padin, A. 2015. *Experimental and Theoretical Study of Water and Solute Transport Mecha- nisms in Organic-Rich Carbonate Mudrocks*. Ph.D. thesis. Colorado School of Mines, Golden, Colorado (December 2015).

Palisch, T., Vincent, M., and Handren, P. 2008. Slick Water Fracturing: Food for Thought. Presented at the SPE Annual Technical Conference and Exhibition, Denver, Colorado, USA, 21-24 September. Paper SPE-115766-MS. http://dx.doi.org/10.2118/115766-MS.

Parnell, J. and Carey, P. 1995. Emplacement of Bitumen (Asphaltite) Veins in the Neuquén Basin, Argentina. *AAPG Bulletin*, 79: 1798–1816. http://dx.doi.org/10.1306/7834df08-1721-11d7-8645000102c1865d.

Pedlow, J. and Sharma, M. 2014. Changes in Shale Fracture Conductivity Due to Interactions with Water-Based Fluids. Presented at the SPE Hydraulic Fracturing Technology Conference, The Woodlands, Texas, USA, 4-6 February. SPE- 168586-MS. http://dx.doi.org/10.2118/168586-MA.

Penny, G. 1987. An Evaluation of the Effects of Environmental Conditions and Fracturing Fluids Upon the Long-Term Conductivity of Proppants. Presented at the SPE Annual Technical Conference and Exhibition, Dallas, Texas, USA, 27-30 September. SPE-16900-MS. http://dx.doi.org/10.2118/16900-MS.

Pyrak-Nolte, L. J., Myer, L. R., and Cook, N. G. W. 1990. Transmission of Seismic Waves Across Single Natural Fractures. *J. Geophys. Res*., 95(B6): 8617–8638. http://dx.doi.org/10.1029/jb095ib06p08617.

Sagasti, G., Ortiz, A., Hryb, D., Foster, M., and Lazzari, V. 2014. Understanding Geological Heterogeneity to Customize Field Development: An Example from the Vaca Muerta Unconventional Play, Argentina. Presented at the Unconventional Resources Technology Conference, Denver, Colorado, USA 25-27 August. SPE-1923357-MS. http://dx.doi.org/10.15530/urtec-2014-1923357.

Sahai, R. 2012. *Laboratory Evaluation of Proppant Transport in Complex Fracture Systems*. Ph.D. thesis, Colorado School of Mines, Golden, Colorado (October 2012).

Saldungaray, P. M., Palisch, T., and Shelley, R. 2013. Hydraulic Fracturing Critical Design Parameters in Unconventional Reservoirs. Presented in the SPE Middle East Technical Conference, Muscat, Oman, 28-30 January. SPE-164043-MS. http://dx.doi.org/10.2118/164043-MS.

Stein, S. and Wysession, M. 2003. *An Introduction to Seismology, Earthquakes, and Earth Structure*. Malden, MA: Blackwell Scientific.

Stinco, L. and Barredo, S. 2014. "Vaca Muerta Formation: An Example of Shale Heterogeneities Controlling Hydrocarbon's Accumulations." Presented at Unconventional Resources Technology Conference, Denver, Colorado, USA 25-27 August. URTEC 1922563, http://dx.doi.org/10/15530/urtec-2014-1922563.

Tepper, B., Baechle, G., J.Keller, Walsh, R., and Quint, E. 2013. Petrophysical Evaluation of Shale Oil and Gas Opportunities in Emerging Plays; Some Examples and Learnings from the Americas. Presented at the International Petroleum Technology Conference, Beijing, China, 26-28 March. IPTC-16926-Abstract. http://dx.doi.org/10.2523/ IPTC-16926-Abstract.

Terracina, J., Turner, J., Collins, D., and Spillars, S. 2010. Proppant Selection and its Effect on the Results of Fracturing Treatments Performed in Shale Formations. Presented at the SPE Annual Technical Conference and Exhibition, Florence, Italy, 19-22 September. SPE-135502-MS. http://dx.doi.org/10.2118/135502-MS.

Terzaghi, K. 1943. *Theoretical Soil Mechanics*. New York, New York: John Wiley and Sons.

Tutuncu, A. 2016. Lecture Notes on Shale Reservoir Engineering.

Tutuncu, A. N., Podio, A. L., and Sharma, M. M. 1993. Effect of Macrofractures on Acoustic Properties of Rocks. Presented at the SEG Annual Meeting, Washington, DC, USA, 26-30 September. SEG-1993-0765.

Urien, C. and Zambrado J.J. 1994. Petroleum Systems in the Neuquén Basin, Argentina. In AAPG Memoir 60: *The Petroleum System–from Source to Trap*. ed. L.B. Magoon and W.G. Dow, Chapter. 32: 513–534. http://dx.doi.org/10.1306/00aa804e-1730-11d7-8645000102c1865d.

Veeken, C., Walter, J., and Kenter, C. 1989. Use of Plasticity Models for Predicting Borehole Stability. Presented at the ISRM International Symposium, Pau, France, 30 August-2 September. ISRM-IS-1989-106.

Vincent, M. and Besler, M. 2013. Declining Frac Effectiveness - Evidence that Propped Fractures Lose Conductivity, Surface Area, and Hydraulic Continuity. Presented at the Unconventional Resources Technology Conference, Denver, Colorado, USA 12-14 August. SPE 1579008-MS. http://dx.doi.org/10.1190/URTEC2013-073.

Vincent, M. C. 2002. Proving it - A Review of 80 Published Field Studies Demonstrating the Importance of Increased Fracture Conductivity. Presented at the SPE Annual Technical Conference and Exhibition help in San Antonio, Texas, USA, 29 September-2 October. SPE - 77675-MS. http://dx.doi.org/10.2118/77675-MS.

Vincent., M. C., Miller, H. B., Milton-Tayler, D., and Kaufman, P. B. 2004. Erosion by Proppant: A Comparison of the Erosivity of Sand and Ceramic Proppants During Slurry Injection and Flowback of Proppant. Presented at the SPE Annual Technical Conference and Exhibition, Houston, Texas, USA, 26-29 September.SPE-90604-MS. http:// dx.doi.org/10.2118/90604-MS.

Willis, M. 2013. *Upscaling Anisotropic Geomechanical Properties using Backus Averaging and Petrophysical Clusters in the Vaca Muerta Formation*. MS thesis, Colorado School of Mines, Golden, Colorado (December 2013).

Willis, M. and Tutuncu, A. 2014. Integration of Core Data with Well Logs for Geomechanical Property Determination and Monitoring in the Argentinian Vaca Muerta Shale Formation. Presented at the Unconventional Resources Technology Conference, Denver, Colorado, USA 25-27 August. SPE-1922481-MS. http://dx.doi.org/10.15530/ urtec-2014-1922481.

Wren, E. 2011. The Prospectively of Unconventional Oil And Gas Resources in the Vaca Muerta Shale of the Neuquén Basin Of Argentina. Presented at the World Shale Gas Conference and Exhibition, 7-11 November. SPE-179145-MS. http://dx.doi.org/10.2118/179145-MS.

Zhou, S. 1994. A program to model the initial shape and extent of borehole breakout. *Computers & Geosciences*, 20(7-8): 1143–1160. URL http://dx.doi.org/10.1016/ 0098-3004(94)90068-x.

APPENDIX A - ASSEMBLY OF THE TRIAXIAL CELL

A.1 Steps to Assemble the Triaxial Cell

1. Make sure hydraulic lines passing through piston cylinders are clean by injecting soap, water then deionized water. This procedure is repeated until the output water conductivity matches or is close to that of deionized water.

2. Apply vacuum grease to the seals of the cells where O-rings are located to ensure proper sealing of pressure.

3. Apply vacuum grease to the upper and lower pistons where they are in contact with the rubber sleeve.

4. Mark the direction of the S-wave polarization in the outer part of the cell and then case the sample with rubber sleeve.

5. Place the propped fracture sample on the lower piston, with the fracture perpendicular to the direction of S-wave polarization.

6. Close the nuts in the lower section of the cell. At this stage the sample is in the cell.

7. Measure the remaining length in the cell and accordingly adjust the length of the axial piston to be slightly longer (5-10 mm) than the measured length. Set up the triaxial cell and align the upper part of the piston to the marked direction of the S-wave propagation. Tighten the nuts for the upper section.

8. Pump mineral oil into the upper section of the cell. While pumping oil in the lower section, the pore pressure ports are connected to a vacuum pump and vacuum pressure is being maintained.

9. Move the cell to the temperature controlled chamber. The chamber is kept closed. Initial axial pressure of 67 psi and confining pressure of 50 psi are applied and not changed until the temperature stabilizes. This is indicated when we see that the axial and confining pumps are no longer taking in fluid volume due to the oil expansion from temperature

increase.

10. Before connecting the cell to the pore pressure lines, push air through these lines to push any unwanted fluids.

11. Connect the pore pressure lines then apply vacuum through the sample for 30 minutes. The vacuum is connected to V15, and vacuum is applied from V7 to V15. Vacuum is also applied to the fluid in the piston connected to the injection pump through V4 for further degassing. Please refer to (Figure 3.15) for further clarification on the valve location.

12. V4 is closed and V5 is opened. The sample is saturated by pumping fluid at very low rate 2cc/min fluid from the injection pump, while still applying vacuum through V15. The saturation process is stopped after the 100 cc of fluid is pumped.

13. Further test steps can now be started.

A.2 Conductivity Measurements

Axial, confining and pore pressures are increased in steps as shown in Appendix B. With each step, the corresponding wave arrival times are recorded. For the first test, short term permeability measurements were recorded starting at 500 psi. In the second test, long term permeability data was recorded for confining stress values of 2000, 4000, 6000, 7500 psi and short term permeability measurements were performed at the stress values between these values. At the time of each permeability measurement, wave velocities were also recorded (compressional and shear velocities). Steps for the permeability test that follow are provided below.

Axial, confining and pore pressures are increased in steps as shown in the Table B.1 in Appendix B and waveforms were recorded at each step. For the first stress state, short term permeability measurements were recorded starting at 500 psi. In the second test short and long term permeability data was recorded for of 2000, 4000, 6000, 7500 confining stress values. Simultaneously, wave velocities have been recorded. Steps for the permeability test were as follows:

1. Stop the injection pump and set it at constant flow and keep the BP pump at constant

pressure of 100 psi.

2. Perform the test at different flow rates for more reliable results and make sure that the pressure differential is readable by observing the wet low pressure transducer screen.

3. Calculate permeability from recorded differential pressures and flow rates.

APPENDIX B - STRESS STATE CONDITIONS DURING TRIAXIAL TEST

The stress state conditions applied in the propped fracture conductivity experiments are presented in Table B.1. The cell, axial and pore pressure values applied during the test are detailed below.

Table B.1: Stress state conditions applied during propped fracture conductivity experiments using the triaxial cell.

σ_a (psi)	σ_r (psi)	P_a (psi)	P_c (psi)	P_p-In (psi)	P_p-out (psi)	P_p eff(psi)	σ_a' (psi)	σ_c' (psi)
50	50	67	50	20	20	20	30	30
100	100	133	100	50	50	50	50	50
100	200	233	200	50	50	50	50	150
200	200	267	200	100	100	100	100	100
300	300	400	300	100	100	100	200	200
400	400	533	400	100	100	100	300	300
500	500	667	500	100	100	100	400	400
600	600	800	600	100	100	100	500	500
800	800	1067	800	100	100	100	700	700
1000	1000	1333	1000	100	100	100	900	900
1500	1500	2000	1500	100	100	100	1400	1400
2000	2000	2667	2000	100	100	100	1900	1900
2500	2500	3333	2500	100	100	100	2400	2400
3000	3000	4000	3000	100	100	100	2900	2900
4000	4000	5333	4000	100	100	100	3900	3900
5000	5000	6667	5000	100	100	100	4900	4900
6000	6000	8000	6000	100	100	100	5900	5900
7000	7000	9333	7000	100	100	100	6900	6900
7500	7500	10000	7500	100	100	100	7400	7400